

**The Role of the Heterointerfaces
in the Cu(In,Ga)Se₂ Thin Film Solar Cell
with Chemical Bath Deposited Buffer Layers**

Von der Fakultät Chemie der Universität Stuttgart
zur Erlangung der Würde eines Doktors der Naturwissenschaften
genehmigte Abhandlung

Vorgelegt von
Nguyen Hong Quang
aus Hanoi, Vietnam

Hauptberichter: Prof. Dr. phil. E. Roduner
Mitberichter: Prof. Dr. rer. nat. habil. J. H. Werner
Tag der mündlichen Prüfung: 23.07.2004

Institut für Physikalische Chemie der Universität Stuttgart
Stuttgart 2004

Contents

Summary	3
Zusammenfassung	6
1 Introduction	9
2 Cu(In,Ga)Se₂ thin film solar cells	11
2.1 Structure and operating principle.....	11
2.2 Cu(In,Ga)Se ₂ absorber layer	13
2.3 Buffer/window layers	14
2.4 Heterointerfaces	17
2.4.1 Models for the CIGS surface layer.....	17
2.4.2 Intermixing at the CdS/CIGS heterointerface.....	20
3 Experimental techniques	22
3.1 Preparation techniques.....	22
3.1.1 Preparation of the Cu(In,Ga)Se ₂ thin film	22
3.1.2 Deposition of buffer layers	22
3.1.3 Preparation of the ZnO window layers.....	24
3.2 Analysis methods	25
3.2.1 X-ray Photoelectron Spectroscopy (XPS).....	25
3.2.2 Secondary Ion Mass Spectroscopy (SIMS)	27
3.2.3 Current/Voltage measurements.....	27
3.2.4 Thermally stimulated capacitance measurements.....	29
3.2.5 Other analysis methods.....	30
4 The CdS buffer solar cell	32
4.1 Background of chemical bath deposited CdS.....	32
4.2 Growth characteristics of CdS	33
4.2.1 Coverage	33
4.2.2 Deviation from stoichiometry	36

4.2.3 Crystallography.....	41
4.3 Modification of the Cu(In,Ga)Se ₂ surface	42
4.3.1 Experiments.....	42
4.3.2 Thermodynamical considerations	42
4.3.3 Chemical analysis.....	45
4.3.4 Solar cell performance.....	48
4.3.5 Discussion	49
5 The In(OH,S) buffer device	52
5.1 Characteristics of the In(OH,S) buffer.....	52
5.1.1 Solution chemistry	52
5.1.2 Buffer properties	54
5.2 Characteristics of the solar cell with the In(OH,S) buffer	57
5.3 Role of the heterointerfaces	58
5.3.1 Experiments with double buffers.....	58
5.3.2 Solar cell performance.....	59
5.3.3 Metastability behavior	65
5.4 Modifications of the ZnO/In(OH,S) interface.....	75
5.5 Discussion	79
5.5.1 Electronic model	79
5.5.2 Metastabilities.....	86
5.5.3 Chemical origin of the defects at the ZnO/In(OH,S) interface.....	88
5.5.4 Role of the chemical bath	89
Outlook for the future work.....	90
Appendix A: parameters used for the simulation.....	91
Symbols and Abbreviations.....	96
References.....	98
Acknowledgement.....	108
Curriculum Vitae.....	109

Summary

The replacement of the toxic chemical bath deposited CdS buffer layer in the heterostructure device ZnO/CdS/Cu(In,Ga)Se₂ is a challenge for research and development of the thin film solar cell based on the Cu(In,Ga)Se₂ (CIGS) material. Though a variety of alternative Cd-free buffers has been tested with considerable success, their solar cells in general are unstable and less efficient compared to the CdS buffer device. The aim of this work is to elucidate the superiority of the CdS buffer as well as the inferiority of an alternative In(OH,S) buffer by comparing the chemical and electronic properties at the heterointerfaces in the solar cells with those buffers. The first part of this thesis studies the formation of the CdS/CIGS interface, focusing on the interaction between the CIGS absorber layer and a standard chemical bath solution for the CdS deposition. The second part investigates the role of the heterointerfaces in the device with chemical bath deposited In(OH,S) buffer in comparison to that in the CdS buffer device.

The study of the interface formation in the CdS buffer device first presents the growth characteristics of the CdS buffer from a standard chemical bath onto the CIGS substrate. X-ray photoelectron spectroscopy (XPS) reveals a complete coverage of the CIGS absorber layer after 4 min of CdS deposition. Taking into account that damage by ZnO sputtering can reach 5 nm depth in the substrate layer, a CdS layer deposited in 5 min is required to separate successfully the ZnO and CIGS layers. This result explains why the performance of the CdS buffer solar cells is best when the CdS layer is deposited in 5 min. A reduction of the CdS deposition duration, aiming at a decrease of the buffer thickness, results in a drastic decrease of the cell performance due to an incomplete coverage of the CIGS absorber surface by CdS, which in turn leads to shunting between the ZnO and Cu(In,Ga)Se₂ layers.

The incomplete coverage also results in a deviation of the S/Cd ratio from unity during the CdS deposition. X-ray photoelectron spectroscopy investigations reveal a large excess of Cd compared to S (S/Cd \approx 0.1) in the early stage of the CdS deposition. This strong deviation from stoichiometry is mainly due to an incorporation of Cd from the chemical bath into the Cu(In,Ga)Se₂ surface layer. The S/Cd ratio increases as long as the absorber surface stays in contact with the chemical bath solution. As the absorber surface is completely covered by CdS, the S/Cd ratio saturates at a value of 0.75. Another factor that influences the S/Cd ratio is a co-deposition of an impurity containing Cd in the form of Cd(OH)₂. During the chemical bath process, Cd(OH)₂ can be converted into CdS due to a metathesis of thiourea on the

surface of $\text{Cd}(\text{OH})_2$. However, this process plays a minor role in the trend of increasing the S/Cd ratio.

The chemical mechanism of the incorporation of Cd into the absorber layer and the formation of $\text{Cd}(\text{OH})_2$ are next targeted by investigations of the treatment of the CIGS absorber in the Cd- NH_3 solutions. The combination of secondary ion mass spectroscopy and XPS measurements shows an intimate tie of both these processes to the reduction-oxidation of the CIGS surface, which is controlled by the NH_3 concentration in the chemical bath solution. With high NH_3 concentration, a Cd diffusion into the absorber layer goes hand in hand with an adsorption of hydroxide ions onto the CIGS surface. When the NH_3 concentration is low, the CIGS surface is oxidized under formation of Se atoms and hydroxide. The latter induces the deposition of $\text{Cd}(\text{OH})_2$ onto the CIGS surface, which prevents a further Cd-diffusion. Both the formation of hydroxides on the CIGS surface and the Cd-diffusion are unfavorable for the solar cell performance.

In contrast to the polycrystalline CdS buffer layer deposited at a high pH value (11.6), the In(OH,S) buffer deposited at a much lower pH value (3.3) has quite different properties. In particular, it has an amorphous structure and contains a large fraction of hydroxide. To separate the role of bulk and interface properties in the electrical performance of the In(OH,S) buffer solar cell, I introduce a simple method by comparing the performance of this device to that of the devices with CdS and combinations of CdS/In(OH,S) buffers. The comparison leads to the following important conclusions:

- i) The interfaces of the In(OH,S) buffer to both the CIGS absorber and the ZnO window layers contain more defects than in the CdS buffer device.
- ii) However, the performance and the stability of the solar cell with the In(OH,S) buffer is predominantly controlled by the defects at the In(OH,S)/ZnO interface, but not by those at the In(OH,S)/CIGS interface. This result indicates that the advantage of the CdS buffer over the In(OH,S) buffer is due to the formation of a more favorable interface to the ZnO window layer. A high density of acceptor-like defects at the In(OH,S)/ZnO interface creates a barrier across this interface, which hinders photogenerated electrons to leave the CIGS absorber and results in a poor fill factor, a low current collection and low open circuit voltage. The reversible effect of air annealing, light soaking is mainly due to a temporal decrease of the defect density at this interface, whereas the reverse voltage bias increases it. Treatments of the In(OH,S) buffer grown on the CIGS absorber

layer in the solution containing Zn^{2+} passivate these defects, and thus improve the cell performance. In this way, I obtain the Cd-free In(OH,S) buffer device with efficiencies comparable to those of the standard CdS device without any need of annealing or light soaking steps.

- iii) The results suggest the presence of a thin inverted surface defect layer (SDL) on the top of the CIGS absorber with a bandgap larger than in the bulk CIGS. A lowering of the valence band energy in the SDL results in a large barrier for holes at the buffer/CIGS interface, and hence makes the interface recombination more tolerant to the defect density at this interface. Thus, the role of the chemical bath deposited buffers is rather to save this SDL than to modify it.

Zusammenfassung

Der Ersatz der aus einem chemischen Bad abgeschiedenen CdS-Pufferschicht in der ZnO/CdS/Cu(In,Ga)Se₂ (CIGS) Heterostruktur-Solarzelle ist eine Herausforderung für Forschung und Entwicklung dieser Dünnschicht Solarzelle. Eine Vielzahl von Solarzellen mit alternativen Cd-freien Puffern wurden mit beachtlichem Erfolg entwickelt. Allerdings sind diese Solarzellen im allgemeinen instabil und weniger effizient im Vergleich zu denen mit CdS-Pufferschicht. Das Ziel dieser Arbeit ist, die Überlegenheit der CdS-Pufferschicht sowie die Unterlegenheit alternativer In(OH,S)-Pufferschicht aufzuklären, durch Vergleichen der chemischen und elektronischen Eigenschaften der Heteroübergänge in den Solarzellen mit diesen Pufferschichten. Der erste Teil der Arbeit untersucht die Bildung der CdS/CIGS Grenzfläche und konzentriert sich auf die Wechselwirkung zwischen der CIGS Absorberschicht und der chemischen Lösung für die CdS Abscheidung. Der zweite Teil untersucht die Rolle der Heteroübergänge im Bauelement mit nasschemisch abgeschiedener In(OH,S)-Pufferschicht im Vergleich zu dem mit der CdS-Pufferschicht.

Die Untersuchung der Grenzflächenbildung in der CdS-Pufferschicht Solarzelle stellt zuerst die Wachstumeigenschaften der Cd-Pufferschicht aus einem chemischen Standardbad auf dem CIGS-Substrat dar. Röntgens Photoelektronen-Spektroskopie (XPS) zeigt eine komplette Bedeckung der CIGS-Absorberschicht nach 4 Minuten CdS-Abscheidung. Da eine Schädigung durch ZnO-Kathodenzerstäubung 5 nm Tiefe in der Substratschicht erreichen kann, sind zur Abscheidung der CdS-Schicht mehr als 4 Minuten erforderlich, um die ZnO und CIGS-Schichten erfolgreich zu trennen. Deswegen ist der Wirkungsgrad der Solarzellen optimal, wenn man eine in 5 Minuten abgeschiedene 50 nm dicke CdS-Schicht verwendet. Eine Verkürzung der CdS-Abscheidungsdauer, darauf abzielend, die Pufferdicke zu verringern, ergibt eine drastische Abnahme des Wirkungsgrades durch die unvollständige Bedeckung der CIGS-Absorberschicht durch CdS.

Die unvollständige Bedeckung ergibt auch eine Abweichung des S/Cd Verhältnisses von 1 während der CdS-Abscheidung. Die Untersuchungen mit XPS zeigen einen großen Überschuss von Cd verglichen mit S ($S/Cd \approx 0.1$) im frühen Stadium der CdS-Abscheidung. Diese starke Abweichung von der Stöchiometrie entsteht vor allem durch den Einbau von Cd aus dem chemischen Bad in die CIGS-Absorberschicht. Das S/Cd Verhältnis erhöht sich so lange die Absorberoberfläche in Verbindung mit der chemischen Badlösung bleibt. Wenn die Absorberoberfläche vollständig von CdS bedeckt ist, erreicht das S/Cd Verhältnis eine

Sättigung bei einem Wert von 0.75. Ein anderer Faktor, der das S/Cd Verhältnis beeinflusst, ist eine Co-Abscheidung von $\text{Cd}(\text{OH})_2$. Während des chemischen Badprozesses kann $\text{Cd}(\text{OH})_2$ durch der Metathese des Thioharnstoffs auf der Oberfläche von $\text{Cd}(\text{OH})_2$ in die CdS umgewandelt werden. Jedoch spielt dieser Prozess eine kleine Rolle bei der Erhöhung des S/Cd Verhältnisses.

Der chemische Mechanismus des Einbaus von Cd in die Absorberschicht und die Bildung von $\text{Cd}(\text{OH})_2$ werden zunächst durch Behandlung der CIGS-Absorberschichten in Cd- NH_3 -Lösungen untersucht. Die Kombination der Sekundärionenmassen-Spektroskopie (SIMS) und der XPS-Messungen zeigt einen deutlichen Zusammenhang dieser Behandlung mit der Red-Ox-Reaktion an der CIGS-Oberfläche, die durch die Konzentration von NH_3 in der chemischen Badlösung gesteuert wird. In der Lösung mit hoher NH_3 -Konzentration, geschieht eine Cd-Diffusion in die Absorberschicht zusammen mit einer Adsorption der Hydroxidionen auf die CIGS-Oberfläche. Ist die NH_3 -Konzentration niedrig, wird die CIGS-Oberfläche unter Bildung von elementarem Se und Hydroxid oxidiert. Das letztere induziert die Abscheidung von $\text{Cd}(\text{OH})_2$ auf der CIGS-Oberfläche, die eine weitere Cd-Diffusion verhindert. Die Anwesenheit der Hydroxide auf der CIGS-Oberfläche und die Cd-Diffusion beeinträchtigen die Leistung der Solarzelle.

Im Gegensatz zu der CdS-Pufferschicht, die bei einem hohen pH-Wert (11.6) abgeschieden wird, hat die In(OH,S)-Pufferschicht, die bei einem viel niedrigeren pH-Wert (3.3) abgeschieden ist, ganz andere Eigenschaften. Insbesondere hat sie eine amorphe Struktur und enthält einen großen Anteil von Hydroxid. Um die Beiträge der Volumen- und Grenzflächeneigenschaften zur elektrischen Leistung der In(OH,S)-Pufferschicht Solarzelle zu trennen, stelle ich eine einfache Methode vor, indem ich die Leistung der In(OH,S)-Pufferschicht Solarzelle mit der der Solarzelle mit CdS- und Kombinationen von CdS/In(OH,S)-Pufferschichten vergleiche. Der Vergleich führt zu den folgenden, wichtigen Erkenntnissen:

- i) Die Grenzflächen der In(OH,S)-Pufferschicht zu beiden der CIGS-Absorberschicht und der ZnO-Fensterschicht enthalten mehr Defekte als in der CdS-Pufferschicht-Solarzelle.
- ii) Die Leistung und die Stabilität der Solarzelle mit der In(OH,S)-Pufferschicht ist jedoch überwiegend durch die Defekte an der In(OH,S)/ZnO-Grenzfläche kontrolliert, nicht durch die In(OH,S)/CIGS-Grenzfläche. Dieses Resultat zeigt, dass der Vorteil des CdS-

Pufferschicht gegenüber der In(OH,S)-Pufferschicht an einer vorteilhafteren Ausbildung der Grenzfläche zur ZnO-Fensterschicht liegt. Die hohe Dichte von Akzeptor-Defekten bei der In(OH,S)/ZnO Grenzfläche bildet eine Barriere an dieser Grenzfläche, die den Fluss der photogenerierten Elektronen vom CIGS-Absorber behindert. Zudem verursacht sie einen schlechten Füllfaktor, eine niedrige Stromsammlung und eine niedrige Leerlaufspannung. Tempern an Luft oder längere Beleuchtung der Solarzelle verringern die Defektdichten. Eine Vorspannung der Solarzelle in Sperrrichtung der Diode erhöht die Defektdichte. Eine Behandlung der In(OH,S)-Pufferschicht, die auf der CIGS-Absorberschicht abgeschieden wird, in Zn^{2+} -Lösung passiviert diese Defekte und verbessert folglich die elektrischen Eigenschaften der Zelle. Auf diese Weise entsteht eine In(OH,S)-Pufferschicht-Solarzelle mit vergleichbarer Leistung wie die Standard-CdS-Pufferschicht-Solarzelle, ohne Notwendigkeit des Temperns oder längerer Beleuchtung.

- iii) Die Resultate deuten auf das Vorhandensein einer dünnen Oberflächendefektschicht (SDL) auf der CIGS-Absorberschicht mit einem höherem Bandabstand hin. Eine Absenkung der Valenzbandenergie durch die SDL ergibt eine große Barriere für Löcher an der Puffer/CIGS-Grenzfläche und erhöht die Toleranz der Rekombination gegenüber der Defektdichte an dieser Grenzfläche. Die Rolle der Pufferschicht ist es daher, diese SDL zu stabilisieren.

1 Introduction

Every year, the sun supplies to the earth a gigantic light energy: 3×10^{24} Joules - a number corresponding to approximately 10,000 times more than the total energy consumption of the global population. Ever since Becquerel discovered in 1839 the photoelectric effect in an electrolytic cell, researchers have been fascinated with the idea of turning the enormous energy from sunlight into electric power. So far, solar cells - the devices that convert directly the sunlight into electricity - are dominated by silicon devices. Today, the solar cells based on the monocrystalline silicon have achieved conversion efficiencies of 24.7% for the laboratory scale and of 10-15% for the module. Note that covering 0.1% of the Earth's surface with solar cells with 10% conversion efficiency would satisfy our present needs. However, the terrestrial use of solar cells is still limited because of high cost of these devices.

One approach to bring down the costs is to develop thin-film solar cells. The development of these new types of solar cell is promoted due to their low material usage [1] and low energy consumption for fabrication [2]. Among them, the $\text{Cu}(\text{In,Ga})\text{Se}_2$ (CIGS) based structure is a promising candidate. The heterostructure device $\text{ZnO}/\text{CdS}/\text{CIGS}$, where the CdS layer is chemical bath deposited (CBD), is the leading type of all thin-film solar cells on a laboratory scale with 19.2% of efficiency [3]. Pilot lines for large-scale CIGS module production have achieved 12.2% efficiency on $60 \times 120 \text{ cm}^2$ at Würth Solar [4] and 13.1% on $60 \times 90 \text{ cm}^2$ at Shell Solar [5], and thus proved an ability of successful manufacture of large area CIGS modules. However, the use of the toxic chemical bath deposited CdS buffer layer in the above mentioned structure is undesirable from the environment point of view. Therefore, replacement of the CdS buffer layer by a non-toxic alternative buffer is one of the major challenges for the research and development of the thin film solar cell based on the $\text{Cu}(\text{In,Ga})\text{Se}_2$ material.

A variety of Cd-free alternative buffers have been tested (see section 2.3), but there is still a lack in efficiency of the alternative buffer devices compared to that of the CdS buffer device. Furthermore, stabilities of the alternative buffer devices upon annealing, light soaking and voltage bias, which often appear more pronounced than in the CdS buffer device, remain open questions. Difficulties in the replacement of the CdS buffer lead to speculations that the advantage of using the CdS buffer is due to a favorable formation of the buffer/CIGS interface during the growth of this buffer from the chemical bath solution (see section 2.4.2).

This work investigates the chemical aspects that are relevant to the formation of the heterointerfaces in the CIGS solar cells with two different CBD-buffers, CdS and In(OH,S), and clarifies their influences on the electrical characteristics of the cells. By comparison of these two devices, I tried to elucidate the questions:

- i) Why is CBD-CdS still the best buffer layer for the CIGS solar cells?
- ii) Do interactions of the chemical solution for the CdS deposition with the CIGS absorber play a decisive role in the advantage of using CBD-CdS?
- iii) What does degrade the electrical performance of the alternative In(OH,S) buffer devices and how to overcome this problem?

After this introductory chapter, the thesis consists of four parts. Chapter 2 first presents the structure of the CIGS solar cell and its operating principle. Afterwards, the properties of each layer in the solar cell and the models for the buffer/CIGS heterointerface are reviewed.

Chapter 3 lists the methods used for preparations of the semiconductors layers in the CIGS solar cells. This chapter introduces also the analyzing methods mainly used during this work.

Chapter 4 first reviews the mechanisms of the CdS formation in the chemical bath solution. Thereafter, the characteristics of the CdS layer grown on the CIGS substrate like coverage, deviation from stoichiometry and crystallography are presented. Another topic of this chapter is interactions of the chemical bath solution with the CIGS substrate and their influence on the cell performance.

Chapter 5 investigates the role of heterointerfaces in the In(OH,S) buffer solar cell. The chemical properties of the In(OH,S) buffer layer are investigated and compared to those of CdS. The role of the heterointerfaces is elucidated by using the buffer combinations CdS/In(OH,S). This chapter presents also an electronic model to explain the influence of the defects at the interfaces on the cell performance.

2 Cu(In,Ga)Se₂ thin film solar cells

2.1 Structure and operating principle

Highly efficient Cu(In,Ga)Se₂ (CIGS) solar cells are fabricated with a multilayer structure as sketched in Fig. 2.1. On a soda lime glass substrate, a Mo film as a back contact with a thickness of 1-2 μm is deposited by sputtering or electron beam evaporation. A p-type Cu(In,Ga)Se₂ thin film semiconductor with a thickness of about 2 μm follows. This layer serves as a light absorber layer and can be prepared either by selenization of sequentially sputtered Cu, In and Ga films [6-8] or by co-evaporation of these elements in different ways [9-11]. A sophisticated buffer/window layer combination helps to optimize a heterojunction in the solar cell. The standard layer sequence of the buffer/window consists of 50 nm CdS formed in a chemical bath, 50 nm nominally undoped sputtered i-ZnO and 300 nm of Al doped sputtered ZnO transparent and conductive oxide. Onto the top of these layers, a Ni/Al front contact grid is deposited by vacuum evaporation. With this structure, cell efficiencies up to 17.8% have been achieved at our institute [12]. Note that the world record cell with an efficiency of 19.2% [3] as well as modules prepared at Würth Solar [13] have the same structure.

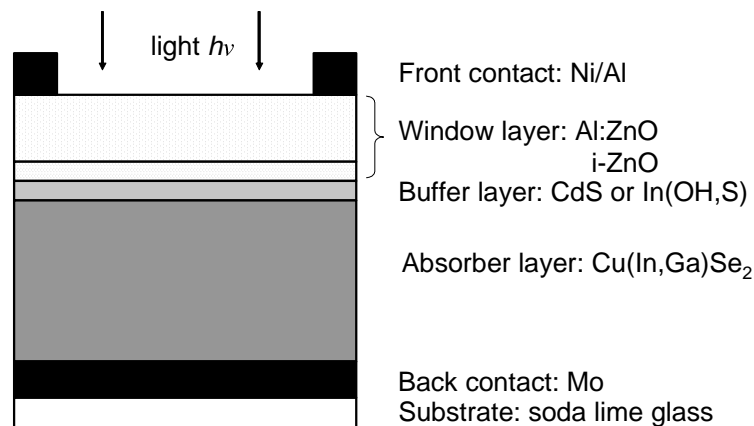


Figure 2.1: Schematic representation of the standard structure of the Cu(In,Ga)Se₂ thin film solar cells fabricated and used for study in this work.

The power generating part of the CIGS solar cell is a pn-heterojunction with the p-doped CIGS region and n-doped buffer/window semiconductor layers. The basic energy band

diagram of this pn-heterojunction is shown in Fig. 2.2. In the dark, electrons diffuse from the n-doped window/buffer layers to the p-doped CIGS absorber layer due to a difference in electron and hole concentrations of these layers. As the result, a part of the window/buffer layers becomes positively charged while a part of the CIGS absorber is negatively charged. These parts with different polarities establish a space charge region (SCR) and an electrical built-in potential V_{bi} in the heterojunction. When the device is illuminated with photons having energies $h\nu$ larger than the band gap energy E_g of the absorber, electrons are excited to the conduction band (E_C) of the CIGS, leaving holes (or positive charges) in the valence band (E_V) (process 1). The generated electrons diffuse to the SCR boundary (process 2) and there they drift further to the buffer/window part in the gradient of the built-in potential (process 3), contributing to the external electrical current. Another process, which plays an important role in photovoltaic cell, is electron-hole recombination. It can occur in the bulk of the CIGS layer (process 4) or at the interface of the pn-heterojunction (process 5) through the recombination centers, often caused by defects. Thus, a main objective of photovoltaic research and device optimization is to minimize such defects.

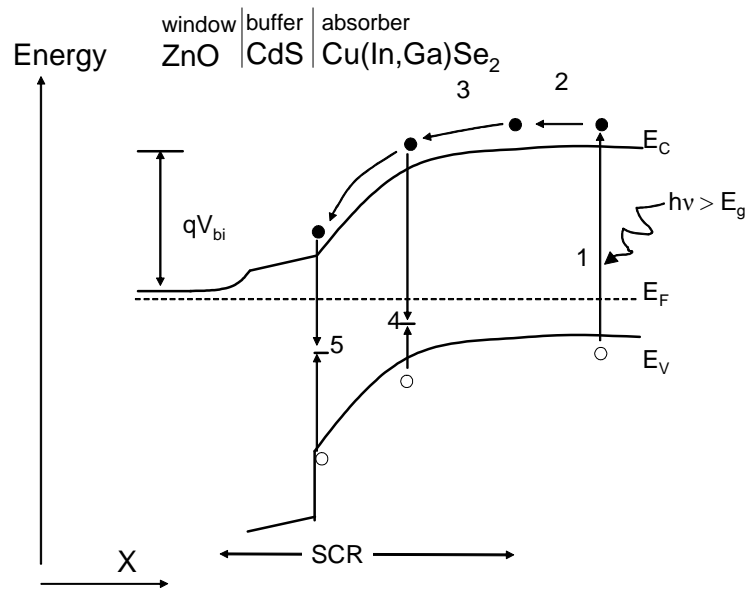


Figure 2.2: *The basic energy band diagram of the ZnO/CdS/CIGS heterostructure under illumination and at short circuit condition. E_C , E_V , and E_F denote for conduction band, valence band and the Fermi energy level, respectively. V_{bi} is the built-in potential in the space charge region SCR. The charge transport processes, marked by numbers, are explained in the text.*

For a more in-depth treatment, I would refer to standard text books in solar cell physics [14,15] and solid-state electronics [16].

2.2 Cu(In,Ga)Se₂ absorber layer

Cu(In,Ga)Se₂ crystallizes in the chalcopyrite structure with a face centered cubic lattice. Each metal atom is tetrahedrally surrounded by four Se-atoms, and every Se-atom is enclosed by two Cu- and two In/Ga-atoms. Figure 2.3 shows the phase diagram of quasi-binary systems In₂Se₃-Cu₂Se derived from differential thermo-analysis [17]. At room temperature, the CuInSe₂ α -phase, which is active for photovoltaic applications, exists in a relatively small region of the Cu-content from 24 % to 24.6 %. In the region of higher Cu-content, Cu₂Se is segregated. At lower Cu-content region, both the α -phase and the β -phase (CuIn₃Se₅) exist. The structure of the β -phase is still not clear. Hönle *et al.* [18] described this phase as a periodic arrangement of Cu- and Se-vacancies (V_{Cu} , V_{Se}) or a substitution of the Cu-atom by an In-atom. Zhang *et al.* [19] illustrated the β -phase as a periodical arrangement of defect-pairs ($2V_{Cu}+In_{Cu}$). The existence range of the α -phase can be extended by an addition of sodium and/or by a partial substitution of In by Ga [20]. It is proposed [20] that a presence of Na in the film prevents the formation of the defect pairs ($2V_{Cu}+In_{Cu}$).

The compounds CIGS are direct band gap semiconductors with band gaps E_g that are

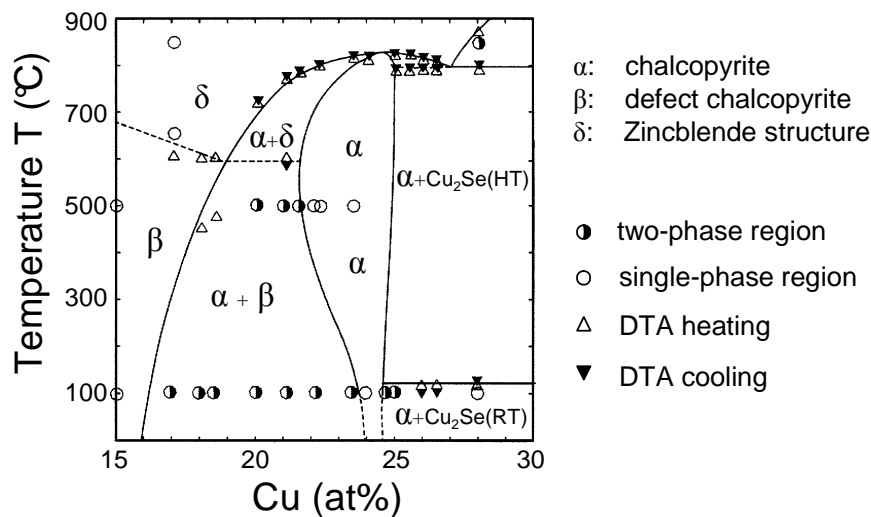


Figure 2.3: Phase diagram for the quasi-binary systems of Cu₂Se-In₂Se₃ obtained by differential thermo-analysis (DTA). After Ref. [17].

almost linearly dependent on the Ga-content ($E_g = 1.02$ eV for CuInSe₂ (CIS) and $E_g = 1.69$ eV for CuGaSe₂ (CGS), [21,22]). Due to a very high absorption coefficient, $\alpha \approx 5.5 \times 10^4$ cm⁻¹ [23,24], CIGS films with thicknesses $d \geq 0.8$ μm absorb most of the light with an energy above the band gap. The CIGS films are intrinsically p-type self-doped with Cu vacancy (V_{Cu}) shallow defects [25]. The energy level of the V_{Cu} defects is theoretically 30 meV [25] above the valence band edge in the band gap. Recombination in the bulk of the CIGS films occurs mainly through deep defects at an energy level around 300 meV above the valence band edge [26]. The origin of this defect is suggested [27] as Cu-atom on an In-site (Cu_{In}). Theoretical calculations of Zhang, Wei and Zunger [19] show a negative formation enthalpy for the electronically neutral defect-pair $2V_{\text{Cu}}+\text{In}_{\text{Cu}}$. A high concentration of this kind of defect explains a high tolerance for a large stoichiometry deviation of up to 1% in the CIGS films [19]. For a more extended description of structural and electronic properties of the CIGS thin-films, the reader is referred to compendia [28-30].

2.3 Buffer/window layers

In earlier years of the development of the thin film CIGS solar cell, an evaporated CdS film was used as a partner to create a heterojunction with the CIGS layer [31]. Due to a low conductivity and a relatively small bandgap (2.4 eV) of the CdS film, the cells had a low fill factor FF and a low quantum response in the blue light region of the solar spectrum. In order to improve these quantities, from the middle to the end of 1980s, the thickness of the evaporated CdS was reduced and a ZnO window layer with a better conductivity and a wider bandgap (3.3 eV) was deposited onto it [32]. A further optimization consisted in replacing the evaporated CdS by a CdS film deposited from chemical bath solutions [33,34,35]. Today, the best CIGS solar cell performances [12,3] are obtained by using a 50 nm thick chemical bath deposited (CBD) CdS buffer. The recipe and the deposition method of the CBD-CdS buffer have been developed already since 1993 by Kessler *et al.* [36]. However, this CBD-CdS buffer layer still causes an electrical loss in short circuit current J_{SC} of about 2 mA/cm² [37]. Hence, the replacement of CdS by wider band gap buffer material, preferably also less toxic, is a major challenge for research and development of the Cu(In,Ga)Se₂ solar cell.

The criteria listed below are essential for an empirical search for new buffer materials:

i) for the bulk properties:

The buffer layer should be as thin as possible and should have a high conductivity to eliminate serial resistances. A large band gap is preferred to avoid absorption of light with short wavelength. High optical transmission is required to let long wavelength light transmit better through to the absorber layer that results on more efficient quantum response.

ii) for the interface properties:

The deposition method as well as the buffer properties at the interface to the CIGS layer should be chosen such that a minimum quantity of interface defects is introduced. A small mismatch in lattice constants a and thermal expansion coefficients α between the buffer layer and the CIGS absorber layer should be advantageous ($a(\text{CIS}) = 5.784 \text{ \AA}$; $a(\text{CGS}) = 5.59 \text{ \AA}$; $\alpha(\text{CIS}) = 8.8 \times 10^{-6} \text{ K}^{-1}$, $\alpha(\text{CGS}) = 1.03 \times 10^{-5} \text{ K}^{-1}$, [38]). Note that the lattice match between CIS and CdS (wurtzite structure) is rather small (1.16%) [39]. A large spike in the conduction band discontinuity ΔE_C could obstruct the photogenerated current, which flows from the p-type absorber layer to the n-type buffer/window layers. On the other hand, a cliff in the ΔE_C would result in increased interface recombination and lower the open circuit voltage V_{OC} of the solar cell. Hence, for an optimized solar cell performance, ΔE_C should be close to zero for a p-type absorber/n-type window heterojunction configuration. However, in the case of a highly doped window, a small spike ($0 \leq \Delta E_C \leq 0.3 \text{ eV}$) would not degrade the cell performance [40,41].

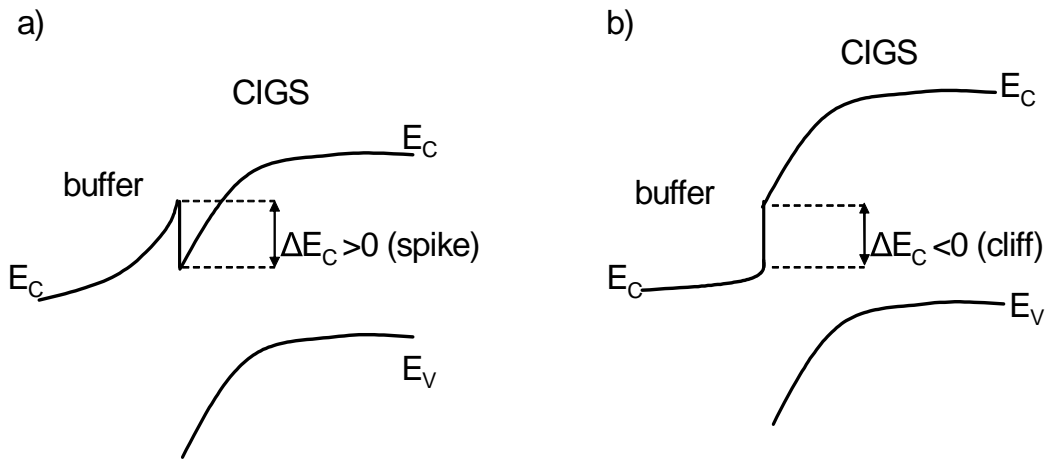


Figure 2.4: Different types of conduction band offset between the CIGS and buffer layers: a) spike with $\Delta E_C > 0$ and b) cliff with $\Delta E_C < 0$.

In reality, a variety of alternative buffer layers based mainly on Zn- and In-compounds, which have higher bandgaps than CdS, is developed with considerable success, but none of these buffer layers yet matches the performance of the standard CdS buffer structure. Table 2.1 gives an overview of the most efficient alternative Cd-free buffers deposited by different methods. Note that CBD-buffers yield higher efficiencies compared to buffers deposited by other methods.

Table 2.1: List of the most efficient alternative Cd-free buffers based on Zn- and In-compounds deposited by different methods: chemical bath deposition (CBD), atomic layer deposition (ALD), metal organic chemical vapor deposition (MOCVD), physical vapor deposition (PVD). Light soaking effect (indicated '+' in the column of the corresponding parameter that improves, '-' means no effect) and voltage bias effects are also displayed.

Buffer layer	Deposition method	Efficiency	Light soaking effect			Voltage effect	Ref.
			V_{OC}	J_{SC}	FF		
Zn(S,O,OH)	CBD	18.6%					[42]
ZnS	CBD	17.7%	+	-	+	yes	[43]
Zn(O,S,OH)	CBD	13%	+	-	+	yes	[44]
Zn(O,S,OH)	CBD	14.2%	+	-	+	?	[45]
Zn(Se,OH)	CBD	14.4%				?	[46, 47]
ZnSe	ALD	11.6%	+	-	+	yes	[48]
ZnSe	MOCVD	14.1%				?	[49]
ZnSe	PVD	9.1%	-	-	-	-	[50]
ZnIn _x Se _y	PVD	12.7%	-	-	-	-	[51]
ZnO	ALD	13.9%	+	+	+	yes	[52, 53]
In(OH,S)	CBD	15,7%	+	+	+	yes	[54, 55]
In ₂ S ₃	ALD	14.9%					[56]
In ₂ S ₃	PVD	11.8%	-	-	-	-	[57]
In ₂ S ₃	Sublimation	14.8%	-	-	-	-	[58]
In _x Se _y	PVD	13%	-	-	-	-	[59]

In general, air annealing at 200 °C up to a few tens of minutes is required to optimize the efficiency in all the alternative buffer devices. In the case of the CBD- and ALD-buffers, light soaking strongly improves the cell performance. Moreover, the devices with the CBD-buffers exhibit more pronounced metastabilities upon an applied voltage bias than the CdS buffer device [60]. The cell performance improves significantly by applying a forward voltage bias and degrades by applying a reverse bias. Metastabilities of the devices with a CBD-In(OH,S) buffer are investigated in chapter 5 of this thesis.

2.4 Heterointerfaces

In all Cu-poor chalcopyrites $\text{Cu}(\text{In}_{1-x}\text{Ga}_x)\text{Se}_2$ solar cells with a CBD-CdS buffer, electronic losses are dominated by the recombination in the bulk of the CIGS absorber [61-64]. In such devices, an asymmetric doping at the CIGS surface with a high barrier for holes, i.e. a type of inversion at the surface layer, is required to minimize surface recombination [65]. There are different models to explain the origin of the inversion at the surface. They can be divided into two main groups: i) the CIGS surface layer is inverted by itself and ii) a graded gap is caused by Cd-diffusion from the chemical bath.

2.4.1 Models for the CIGS surface layer

Ordered Defects Compound (ODC) model: It was experimentally observed that the surface composition of the $\text{Cu}(\text{In,Ga})\text{Se}_2$ thin film deviates from the bulk composition [66-69]. One of the reasons can be that the CIGS surface is self-reconstructed to be energetically more stable as shown by a theoretical calculation from a first-principle total energy approach [70].

Schmidt *et al.* [66] found a segregation of Cu_xSe on the surface in the Cu-rich CIS films ($\text{In}/(\text{In}+\text{Cu}) < 0.5$), see Fig. 2.4a. In contrast, a slightly In-rich bulk composition ($\text{In}/(\text{In}+\text{Cu}) > 0.52$) results in a very In-rich surface with a composition stoichiometry close to CuIn_3Se_5 (i.e. $\text{In}/(\text{In}+\text{Cu}) = 0.75$). Simultaneously, in this case, the distance of the Fermi level E_F from the valence band at the CIS surface is very large, suggesting an n-type surface layer.

As deduced from these results, the band diagram for the CIS film is sketched in Fig. 2.4b. While the bulk of pure CIS is p-type with a band gap $E_{g1} = 1.04$ eV, the surface phase, called ordered defects compound (β -phase CuIn_3Se_5), is an inverted n-type layer with a larger bandgap E_{g2} . A direct measurement for CuInSe_2 by combining x-ray photoelectron

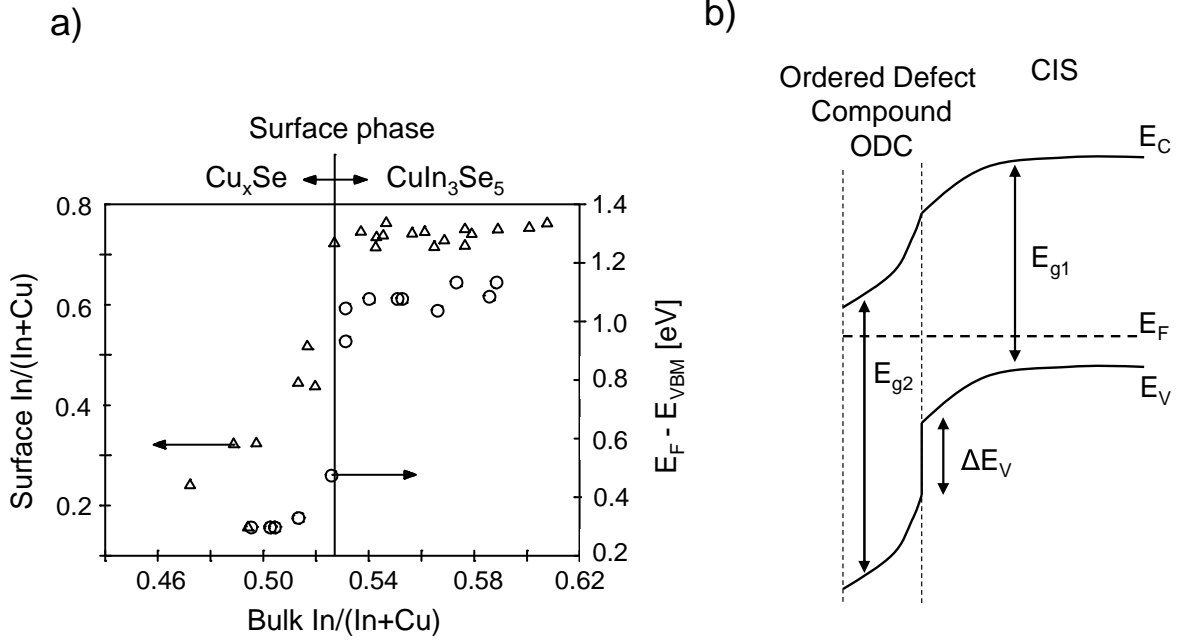


Figure 2.4: a) The surface versus bulk composition for a CuInSe_2 thin film suggests a segregation of an n-type CuIn_3Se_5 surface phase for a bulk $\text{In}/(\text{In}+\text{Ga})$ ratio greater than 0.52 [66] and b) the proposed band diagram for the CuInSe_2 thin film: a n-type ordered defect compound with a larger bandgap than that in the bulk is formed on the CIS surface layer.

spectroscopy with inverse photoemission spectroscopy proved that the band gap of the surface layer is wider ($E_{g2} = 1.4$ eV) [71]. Such an inversion creates a buried p-n-junction within the CIS film and shifts the pn-junction away from the CdS/CIS interface. In addition, the possibility of CIS to form ODC also allows for a larger barrier for holes $\Phi_b^p = E_F - E_{\text{VBM}}$ because of the different valence band edge energies ΔE_V [72].

Adding Ga to the CIS film affects the type inversion of the surface negatively. Using ultra-violet photoelectron spectroscopy (UPS) to measure the Fermi level E_F at the surface, Schmidt [73] has shown that the surface type inversion reduces with an increase in Ga-content, i.e. the distance of E_F to the conduction band increases. The type inversion disappears with Ga-content ($\text{Ga}/(\text{Ga}+\text{In})$) more than 0.8.

Cahen-Noufi model: In contrast to the ODC model, Cahen and Noufi [74] suggested that surface states like Se vacancies (V_{Se}) on the CIGS surface play an important role in the type inversion of the CIGS surface. Due to a deficiency of Se, In on the surface gives electrons from its outermost atomic level to the conduction band of the CIGS film. As a result the In

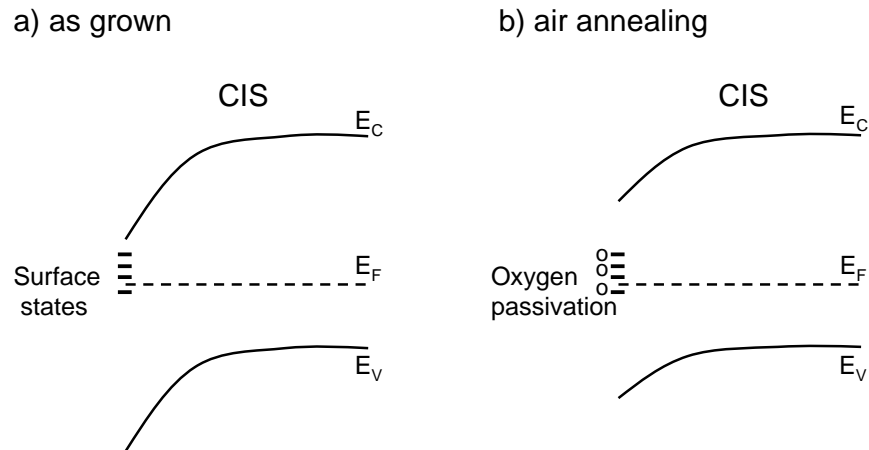


Figure 2.5: *a) A large concentration of surface states V_{Se} causes a large band bending in a $CuInSe_2$ thin film and b) air annealing or air exposing passivates the surface states by an oxidation, resulting in a decrease of the band bending.*

becomes a positively charged donor state and the conduction band bends strongly down to the Fermi level (Fig. 2.5a), i.e the surface is type inverted. When the CIGS film is exposed to the air, the oxygen can get electrons from the conduction band, is reduced to O^{2-} and binds to V_{Se} . As a result the surface states are passivated and the conduction band bending is decreased (Fig. 2.5b).

During the chemical bath deposition of CdS, oxides on the CIGS surface are dissolved and the V_{Se} as well as the large band bending are restored. By an analytical calculation [75] and a simulation [63] for the device based on a ZnO/CdS/CIGS heterojunction, the authors show that densities of interface states in the order of $10^{13} \text{ cm}^{-2} \text{ eV}^{-1}$ are sufficient to pin the Fermi level E_F at the CdS/CIGS interface at the neutrality level. Air annealing of the complete device passivates again the V_{Se} and reduces the surface type inversion.

Surface defect layer model: The surface defect layer (SDL) model proposed by Herberholz *et al.* [76] is a compromise between the two above models. In this model, a type inversion is not caused by a surface segregation of the β -phase. A field caused by positively charged donor states on the CIS surface can push Cu^+ ions to migrate deeper into the CIS layer. As a result, a surface defect layer (SDL) with a high concentration of negatively charged defects is formed (Fig. 2.6). From the theoretical calculation of Jaffe and Zunger [77], the band gap of this surface defect layer is larger than that of the bulk, and the valence band toward the surface is enlarged. This together with a band bending caused by the surface states V_{Se} results in the high barrier for holes at the CdS/CIS interface, which prevents recombination at the interface.

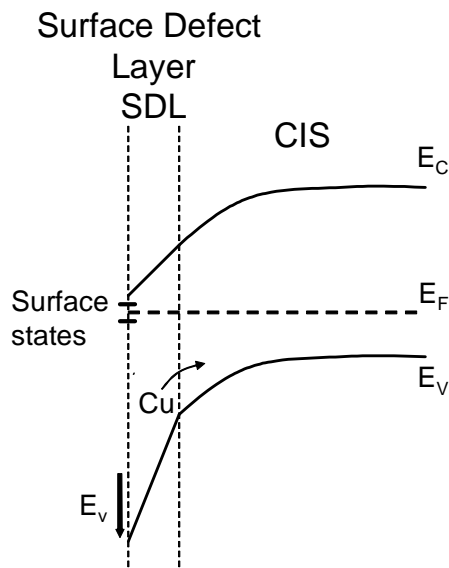


Figure 2.6: CIS band diagram after the model of Herberholz *et al.* [75]. A surface defect layer is created due to the migration of Cu from the surface into the bulk. The band gap of the surface defect layer is larger than that in the bulk.

2.4.2 Intermixing at the CdS/CIGS heterointerface

The CdS/CIGS interface is not abrupt but graded with an intermixing of the elements from the CdS buffer and the CIGS substrate. Heske *et al.* found Se while measuring XPS for the CdS/CIGS samples with different CdS thickness and interpreted the results by an out-diffusion of Se from the CIGS substrate into the CdS layer [78]. A Cd diffusion from the chemical bath into the CIGS absorber layer has been reported by several authors [79,80,81,82]. The depth of the Cd diffusion caused by chemical bath deposition of CdS is differently reported. By Secondary Ions Mass Spectroscopy (SIMS) profile measurements Wada [81] observed Cd diffusion up to ca 50-100 nm deep into the absorber layer. Nakada reported from his Energy Dispersive X-ray spectroscopy (EDX) measurement with a small spot [79,82] a presence of Cd at 10 nm CIGS surface layer. Liao *et al.* [83] by resolved angle XPS found a large concentration of Cd atoms at the very surface, within only 1-3 atomic layers of CIGS.

In parallel with the observations of the Cd diffusion, a decrease of Cu content at the surface layer compared to that in the bulk is observed [80,81]. Since the ionic radii of Cd^{2+} (0.97 Å) and Cu^+ (0.96 Å) ions are very close, it is likely that the diffused Cd atoms substitute Cu vacancies.

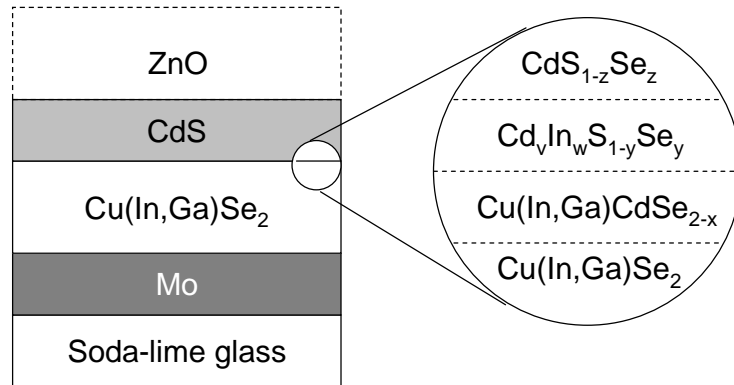


Figure 2.7: Intermixing of the elements at the CdS/CIGS interface due to diffusion processes.

Ramanathan [84] suggested that Cd diffusion results in an n type surface region and may play an important role in the formation of the homojunction in the CIGS absorber layer. This would imply an advantage of CBD-CdS over other Cd-free alternative buffers. CuInSe₂, n-doped by Cd, is reported by Yu *et al.* already since 1975 [85]. Their Hall measurements have shown a type conversion of CuInSe₂ from p-type to n-type by ion implantation of Cd [86]. This suggestion of Ramanathan leads to a number of experiments with a pre-treatment of the CIGS absorber layer in the ammonia solution containing Cd prior to the deposition of the alternative buffers or a direct deposition of the ZnO-window. Instead of the Cd-solution, Zn-solution is also applied to treat the CIGS absorber.

3 Experimental techniques

3.1 Preparation techniques

3.1.1 Preparation of the $\text{Cu}(\text{In,Ga})\text{Se}_2$ thin film

In this thesis, all the $\text{Cu}(\text{In,Ga})\text{Se}_2$ thin films are Cu-poor in stoichiometry. They are prepared by vacuum evaporation onto the Mo-coated soda-lime glass in the three-stage process as described elsewhere [87,88]. Figure 3.1 shows a scheme of the evaporation rate of the metals and their ratio in the three-stage process. The process begins with the deposition of a $(\text{In,Ga})_2\text{Se}_3$ precursor layer. During the second stage, only Cu and Se are evaporated to obtain a film, which is Cu-rich in stoichiometry. In order to obtain a Cu-poor absorber film, where the ratio $\text{Cu}/(\text{In}+\text{Ga}) < 1$, In, Ga and Se are evaporated again in the third stage.

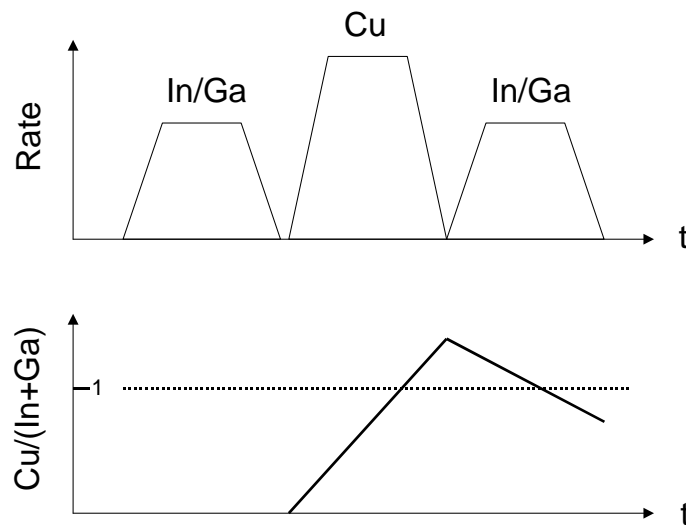


Figure 3.1: Schematic representation of the evaporation rates and the ratio $\text{Cu}/(\text{In}+\text{Ga})$ in the CIGS absorber film for a three-stage process.

3.1.2 Deposition of buffer layers

As buffer layers for CIGS solar cells, two kinds of thin films, CdS and $\text{In}(\text{OH,S})$, are deposited from chemical bath solutions. In both cases, the deposition of the buffer is mainly

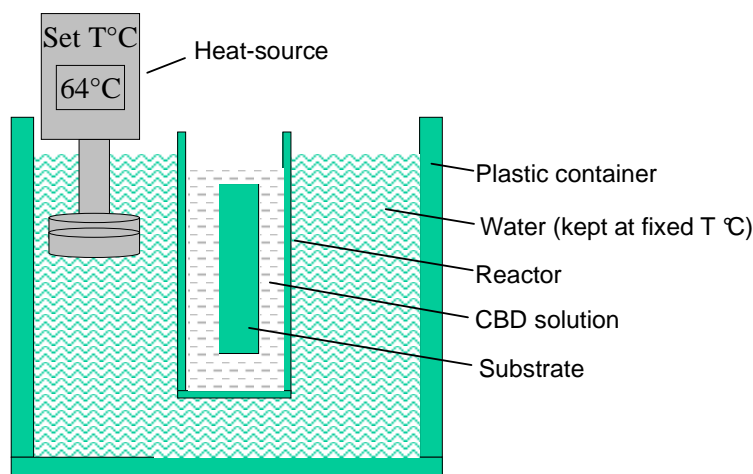


Figure 3.2: *The experimental set-up for the chemical bath deposition of the buffer films used in the present research work.*

performed according to the following procedure: the aqueous solutions of the metal salt (cadmium acetate or indium chloride) and sulfide source (thiourea or thioacetamide) is poured in a glass beaker (ca. 80 ml). The CIGS substrate is immersed in this room temperature CBD solution (50 ml). The beaker is then immediately placed in a water bath kept at a fixed temperature T_B ($T_B = 64\text{ °C}$ for the CdS and $T_B = 74\text{ °C}$ for the In(OH,S)). During the deposition, the CIGS substrate is shaken in order to homogenize temperature and concentrations. After the deposition, the sample is rinsed in de-ionized water and blown dry with nitrogen.

Table 3.1 shows the main parameters of the chemical solutions for the CdS and In(OH,S) depositions. The basic difference between the solutions is their pH values. While the In(OH,S) film is deposited at a low pH (3.3), the solution for the CdS deposition with added ammonia as a complex agent has a pH value of 11.6.

Table 3.1: *Parameters of the chemical bath conditions used in this thesis*

Buffer	Metal salt	S source	Complex	pH	T_B (°C)	t (min)
CdS	$\text{Cd}(\text{CH}_3\text{COO})_2$	$(\text{H}_2\text{N})\text{CS}$	NH_3	11.6	64	5
	1.4 mM	140 mM	1 M			
In(OH,S)	InCl_3	CH_3CSNH_2	-	3.3	74	15
	5 mM	150 mM				

3.1.3 Preparation of the ZnO window layers

After the buffer layer deposition, the solar cells are completed by sputtering a bilayer ZnO window (i-ZnO/Al:ZnO) and vacuum vapor deposition of the Al-grid contact. In the following, the basic aspects of the sputtering method are briefly described. More details can be found elsewhere in the literature [89,90].

In a vacuum chamber, in the presence of an inert gas, e.g. Ar (pressure $p = 0.1\text{-}10\text{ Pa}$), a plasma is obtained by applying a suitable voltage between a target and substrate (see Fig. 3.3). Due to the electrical field, the ionized Ar atoms in the gas are accelerated and bombard the target. Due to the bombardment, the target atoms or molecules are emitted and deposited on the substrate. Depending on whether the type of the applied voltage is direct or alternating at high frequency (13.56 MHz), we have DC-sputtering or RF-sputtering, respectively. A built-in magnet close to the target increases the plasma density (magnetron sputtering), and hence increases the deposition rate. In this case, we have magnetron sputtering.

In the present work, a commercial sputtering system from CJT is used to prepare the ZnO window layers. The system consists of two parts: a chamber with pre-pump and a main chamber with turbo pump. This combination guaranties a stable base pressure of 5×10^{-7} bar in the main chamber. The system contains three target-stations with a diameter of 6 inches, two of them contain clean ZnO for the preparation of the undoped intrinsic ZnO (i-ZnO) and the third contains a mixture of 98% ZnO + 2% Al₂O₃ for the preparation of the highly doped ZnO (Al:ZnO). The distance between the targets and the substrate is 8 cm. All the layers are deposited by RF-magnetron sputtering with a power of 200 W. Table 3.2 lists the parameters of the ZnO sputtering processes.

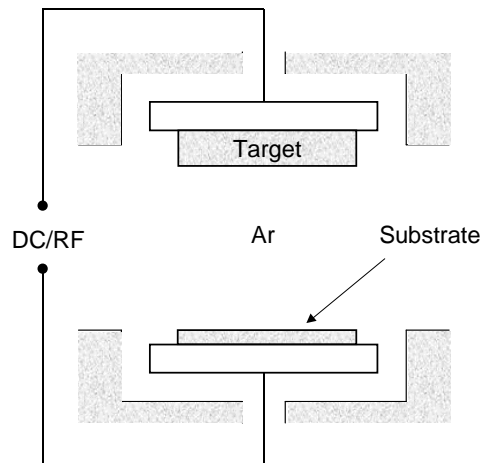


Figure 3.3: Schematic representation of sputtering system for the preparation of ZnO layers.

Table 3.2: Parameters of the sputtering processes used in this thesis (sccm is denoted for standard cubic centimeter)

Window layer	Target material	Gas	Gas flux f (sccm)	Pressure p (Pa)
i-ZnO	ZnO (99.99%)	Ar	10	0.35
Al:ZnO	ZnO + 2wt% Al ₂ O ₃	Ar	10	0.35

3.2 Analysis methods

3.2.1 X-ray Photoelectron Spectroscopy (XPS)

The XPS technique is an analytical tool for extracting the elemental composition and chemical states of the uppermost few atomic layers of a sample. This is accomplished by irradiating the sample in ultrahigh vacuum by soft X-rays and analyzing the number and the kinetic energy of the emitted electrons. Normally MgK α (1253.6 eV) or AlK α (1486.6 eV) X-rays are used.

Irradiating the sample with X-rays leads usually to the ejection of three kinds of electrons:

i) Photoelectrons, emitted by the photoelectric effect (Fig. 3.4), with kinetic energy

$$E_{\text{kin}} = h\nu - E_{\text{B}} - \Phi_{\text{S}} \quad (3.1)$$

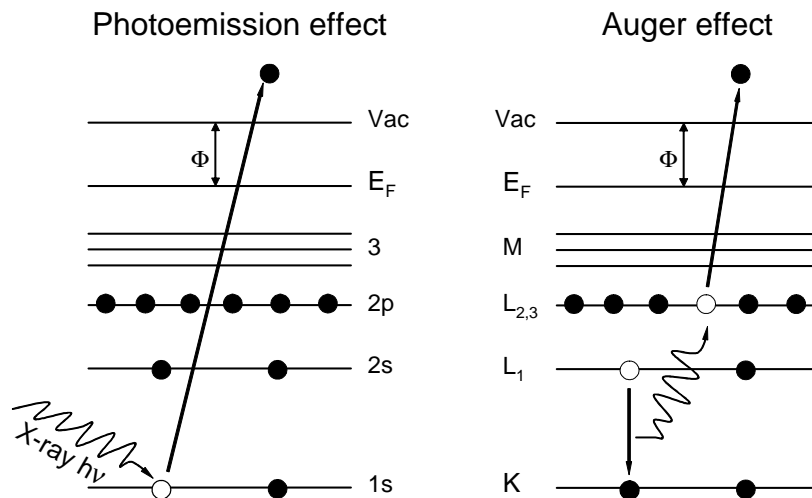


Figure 3.4: Schematic representation of the photoemission and Auger effects.

where $h\nu$ is the energy of the incident X-ray photon, E_B is the binding energy of the atomic orbital from which the electron is ejected, and Φ_S is the work function of the X-ray photoelectron spectrometer.

ii) Auger electrons are emitted by the sequence of events following ionization of a core level as described on the right-hand side of Fig. 3.4. In this example, the K level is ionized by an incident X-ray photon. Then, the created hole in the K level is filled by a transition of an electron from the outer level L_1 . As a result of that transition, the energy difference ($E_K - E_L$) can appear as an emitted photon (fluorescence effect) or can be transferred to another electron (for example of the $L_{2,3}$ level), whereupon the second electron is ejected (Auger effect). The energy of the ejected Auger electron of the example in Fig. 3.4 is

$$E_{KL_1L_{2,3}} = E_K - E_{L_1} - E_{L_{2,3}}^* - \Phi_S \quad (3.2)$$

where E_i are the binding energies of the i th atomic energy levels. Note that $E_{L_{2,3}}^*$ is different from $E_{L_{2,3}}$ due to the presence of a hole in level L_1 .

iii) Electrons emitted from the valence band of the sample: The energies of this kind of electrons lay between the zero binding energy (by definition of the Fermi level E_F) and the first 10-20 eV below. From this low binding energy region it is in principle possible to extract valence band-offsets between the semiconductor layers.

Chemical analysis

The XPS analysis can give information about the chemical states of the elements on the sample surface. The electron binding energies are shifted compared to those in the free atom by different amounts, depending on formal oxidation states and molecular environment of the atom. The physical basic of that so-called “chemical shift” effect is illustrated by a relatively simple model, the charge potential model [91]. In general, the higher the oxidation state and the polarity of the bond to the neighbor atoms the larger are the binding energies of the photoelectrons. A consideration to take into account when interpreting chemical shifts in XPS spectra of the semiconductors is a possible Fermi-level shift due to charging or band bending

at the surface [92]. This problem can be overcome by using the Auger parameter, which was introduced by Wagner [93] and is given by

$$\alpha = E_{\text{kin}}(\text{KLM}) + E_{\text{B}}(\text{D}) \quad (3.3)$$

where $E_{\text{kin}}(\text{KLM})$ is the kinetic energy of the Auger transition KLM and $E_{\text{B}}(\text{D})$ is the binding energy of the photoelectron ejected from level D. This parameter is used as a fingerprint of the chemical state of the element. A large number of Auger parameters of the elements in different compounds is given in handbooks [94,95].

Experimental setup

The XPS experiments were carried out using a commercial XPS system Leybold. The system consists of a semispherical analyzer (EA 200), an X-ray source of a twin Mg/Al-anode and the data registration system DS100. The measurements are conducted in an ultra high vacuum of 10^{-8} bar with the Mg-anode X-ray source (1253.6 eV). The analyzed area of the samples is $4 \times 7 \text{ mm}^2$.

3.2.2 Secondary Ion Mass Spectroscopy (SIMS)

In the SIMS technique, the surface of a sample is bombarded by primary ions (e.g. O_2^+ , O^- , Ar^+ , Cs^+ , and N_2^+). Simultaneously, secondary ions are emitted from the sample surface and detected by mass spectroscopy. The SIMS method permits to make a depth profiling of all elements and their isotopes in a film.

In this work, the SIMS experiments are carried out with a ‘‘Atomika 6500’’ analysis system. O_2^+ was used as the primary ion to bombard Cd-treated $\text{Cu}(\text{In},\text{Ga})\text{Se}_2$ samples to avoid a mass interference between Cd and In signals. The ion beam is scanned over an area of $300 \times 300 \text{ }\mu\text{m}^2$ and positive secondary ions were collected from a central part about $5 \text{ }\mu\text{m}$ in diameter of this area.

3.2.3 Current/Voltage measurements

The performance of solar cells is normally studied through current/voltage (I/V) measurements at 25°C in the dark and under AM1.5 illumination ($100\text{mW}/\text{cm}^2$), where

parameters like the open-circuit voltage V_{OC} , short-circuit current J_{SC} , fill factor FF and conversion efficiency η can be extracted. The maximum power that can be delivered from the solar cell is indicated by the area of the rectangle (i.e. $P_{max} = V_{max} \times J_{max}$) in Fig. 3.5. The fill factor FF is given by $(V_{max} \times J_{max}) / (V_{OC} \times J_{SC})$. Then the conversion efficiency η is given by

$$\eta = \frac{V_{OC} \times J_{SC} \times FF}{P} \quad (3.4)$$

where P is the illumination power.

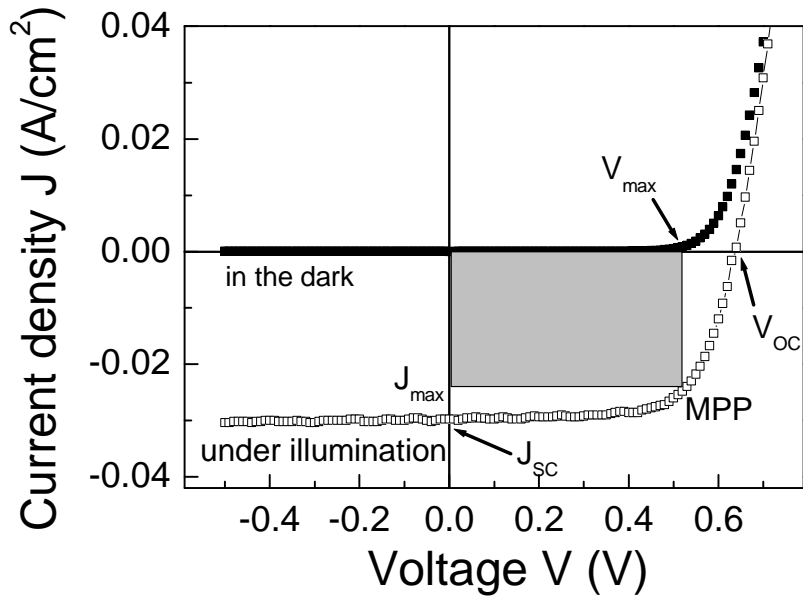


Figure 3.5: Current/Voltage characteristics of the ZnO/CdS/Cu(In,Ga)Se₂ heterostructure in the dark and under illumination displaying the common parameters used to define the performance of the solar cell.

In the dark, the device follows the well-known rectifying current/voltage characteristics of the simple p-n-diode. Under illumination, the extra current generated from the light absorption (J_{Light}) is added to give the following ideal equation for a p-n-junction solar cell [96]:

$$J = J_{Dark} - J_{Light} = J_0 [\exp(qV/nkT) - 1] - J_{Light} \quad (3.5)$$

where J is the current density flowing through the solar cell, J_0 the saturation current, q the electrical charge, V the applied voltage, n the diode ideality factor, k the Boltzmann constant and T the temperature of the solar cell.

In order to infer the dominant recombination process in the solar cell, temperature-dependent current/voltage measurements were also carried out. The principle of the method is described in Refs. [97,98] and based on the interdependence of short circuit current density J_{SC} and V_{OC} as

$$J_{SC} = J_0 \exp\left[\frac{qV_{OC}}{nkT}\right] = J_{00} \exp\left[\frac{-E_A}{nkT}\right] \exp\left[\frac{qV_{OC}}{nkT}\right] \quad (3.6)$$

Where J_{00} is a weakly temperature-dependent prefactor and E_A is the activation energy of the dominant recombination process in the solar cell. Reorganizing Eq. 3.6 yields

$$n \times \ln(J_0) = -E_A/kT + n \times \ln(J_{00}) \quad (3.7)$$

Thus, an Arrhenius plot of $n \times \ln(J_0)$ versus the inverse thermal energy $1/kT$ yields a straight line with the slope $-E_A$. Dependent on the recombination mechanism, the activation energy E_A has different values. In the case of recombination in the space charge region in the absorber layer, the activation energy E_A equals the band gap energy E_g , whereas in the case of the interface recombination E_A equals the barrier for holes at the CIGS surface Φ_b^p .

3.2.4 Thermally stimulated capacitance measurements

Thermally stimulated capacitance (TSC) measurements are used to investigate the different metastable states that are achieved by different biasing conditions. To characterize the equilibrium state of the devices, the junction capacitance is measured versus temperature in the dark at zero voltage bias in a temperature range from $T = 80$ K to 300 K using a heating rate $r_h = 5$ K/min. To obtain a metastable state, a reverse voltage bias of -1V is applied for 1 hour (stage 1 in Fig. 3.6) and then the samples are cooled to 80 K within 5 min after switching off the voltage (stage 2). The junction capacitance is scanned again up to 300 K with $r_h = 5$ K/min (stage 3). At 300 K the measurement continues for some ten minutes to show the relaxation of the junction capacitance. A better visualization of the contribution of defects to the metastable state can be obtained by monitoring the capacitance alternately at two slightly different frequencies (e.g., at $f_1 = 100$ kHz and $f_2 = 110$ kHz). Then, the frequency

dispersion of the capacitance, determined by calculating $f \times dC/df \approx [C(f_1) - C(f_2)] / [f_1 - f_2] \times [f_1 + f_2] / 2$, transforms capacitance transitions to minima in the TSC curve.

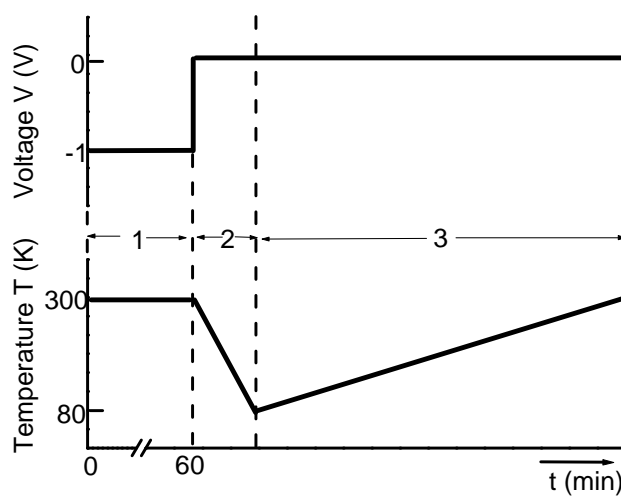


Figure 3.6: Schematic representation of the time-dependent temperature and applied voltage for the thermally stimulated capacitance measurements.

3.2.5 Other analysis methods

For the determination of the crystallinity of the deposited CdS buffers, X-ray diffraction as non destructive method was used. The diffraction spectra of the CBD-CdS is compared afterwards with reference data from single crystal or powder samples (Joint Committee on Power Diffraction Standard: JCPDS). From the width and intensity of the measured lines, information about the crystal quality and a preferred orientation can be gained. The buffer films in this work were characterized with a powder diffractometer DIFFRAC 500 of Siemens with Cu-K α excitation (840 kV/30 mA).

In order to obtain an optical impression of the quality of the buffer layers a high resolution scanning electron microscope from Philips is used.

For the investigation of the optical Transmission, a commercial UV-Vis-NIR spectrophotometer (VARIAN CARY 5E) with implemented data acquisition and evaluation system is used.

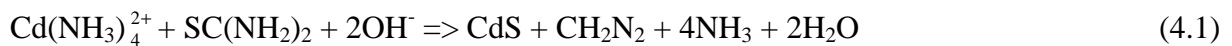
For the electrical characterisation of the heterostructure, spectral response measurements were also carried out. The solar cell is illuminated with a monochromatic light of defined intensity and the photocurrent developing thereby is measured by a lock-in technique. The system for the quantum efficiency measurements consists of individual components of the company BENTHAM INSTRUMENTS (monochromator TM300/2, variable frequency Optical Chopper model 218, current amplifier model 277) and an ITHACO 3961 lock-in amplifier. The calibration is made by a HAMAMATSU pyrodetector and a silicon calibration cell.

4 The CdS buffer solar cell

In this chapter, the investigations are focused on the interactions between the Cu(In,Ga)Se₂ substrate and the chemical bath solutions for the CdS deposition. It includes influences of the substrates on the characteristics of the CdS layer grown from the standard solution. Thereafter, the modification of the CIGS absorber layer by treatments in solutions containing Cd-salt and its influence on the solar cell performance are investigated.

4.1 Background of chemical bath deposited CdS

Until today, the most efficient buffer for the Cu(In,Ga)Se₂ solar cells is CdS deposited by the chemical bath method (CBD). CdS is usually formed from the reaction between dissolved cadmium ions and thiourea molecules in ammonia solutions, according to the overall reaction

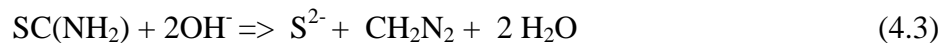


The commonly accepted reaction scheme [99-102] is the following

- i) Release of Cd²⁺ from the ammonia complex



- ii) Release of S²⁻ from thiourea



- iii) Precipitation of CdS



When the ionic product exceeds the solubility product of CdS, it precipitates (reaction 4.4) either in the bulk of the solution with the formation of colloids or at the surface of the substrates leading to the formation of a film. Consequently, the film can be formed by two different mechanisms: i) the sedimentation of the colloids from the solution (heterogeneous growth) and/or ii) the direct reaction of the ions at the surface of the substrates (ion-by-ion growth).

CdS has been reported to grow epitaxially on single crystals such as InP by the CBD method [103]. This observation supports the ion-by-ion mechanism. Further evidence comes from HRTEM studies [104,105].

Beside the reaction between the ions, another mechanism of CdS formation called thiourea metathesis at the surface of cadmium hydroxide is proposed. In early work, Kitaev *et al.* [106] suggested that the presence of hydroxide particles in solution was necessary for the growth of good quality CdS films, the decomposition of thiourea being stimulated by a solid phase such as cadmium hydroxide. This proposal was supported by the observations of Kaur *et al.* [107] in that adherent films were only prepared in the presence of Cd(OH)₂ in solution. Froment and Lincot [108] suggested that the mechanism of film formation, similar to that proposed by Parfitt [109], could be represented by the following series of consecutive surface adsorption/reaction steps:



Where C* is a reaction intermediate.

4.2 Growth characteristics of CdS

4.2.1 Coverage

One of the roles of the CdS buffer is the protection of the Cu(In,Ga)Se₂ surface from a damage caused by the ZnO-sputtering process. Therefore, complete coverage is a matter of primary interest. Since x-ray photoelectron spectroscopy is a very surface sensitive analysis method, it can be used to observe how completely the CBD-CdS thin films deposited during different durations cover the CIGS absorber layer.

Figure 4.1 shows the evolution of the XPS signals from the CIGS substrate (In 3d_{5/2} and Se 3s) and from the deposited CdS (Cd 3d_{5/2} and S 2s) after different times in the chemical bath. After 30 s, the Cd signal is already clearly seen on the CIGS substrate, whereas the signal of S is still quite small. At this moment, a S/Cd atom ratio of only about 0.1 is derived. With longer deposition times, both these signals increase continuously with a simultaneous

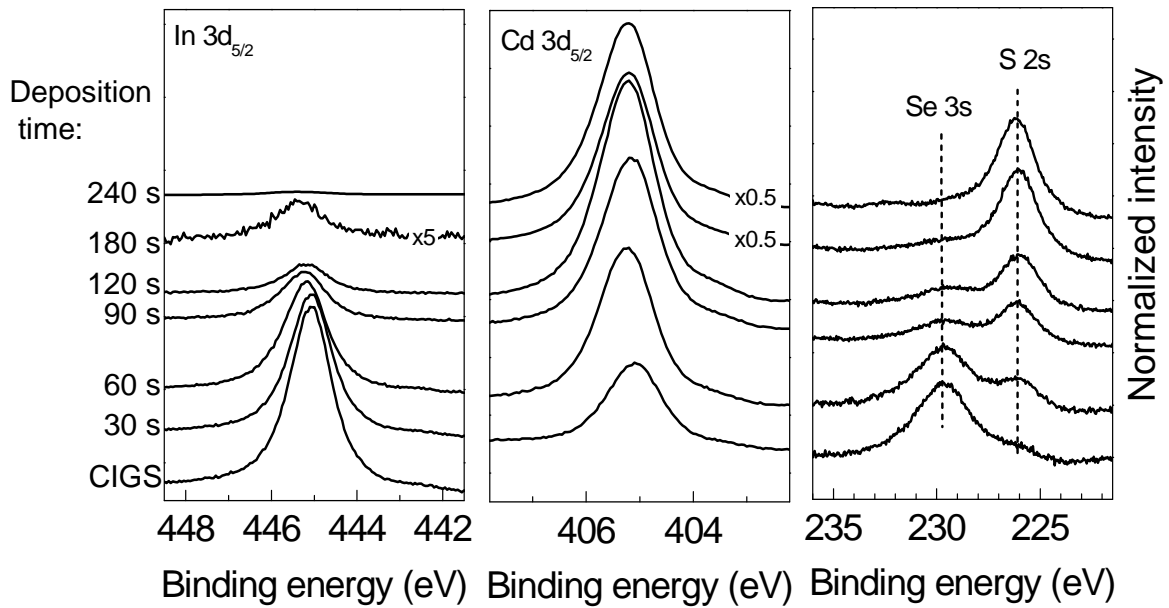


Figure 4.1: The XPS region of In 3d_{5/2}, Cd 3d_{5/2}, Se 3s and S 2s showing the evolution of those elements after different times in the CBD bath. The signals of In 3d_{5/2} and Se 3s from the Cu(In,Ga)Se₂ substrate disappear after 240 s dip time in the chemical bath.

decrease of the In and Se signals. The binding energies of In 3d_{5/2} and Cd 3d_{5/2} have a small tendency to shift to higher values. However the Auger parameters of In (= 853.0 eV) and Cd (= 786.7 eV) all remain constant within ± 0.1 eV for successive deposition times.

After 240 s of CdS deposition, the signals of In and Se from the underlying CIGS substrate disappear. This time corresponds to the complete coverage of the Cu(In,Ga)Se₂ surface with a CdS overlayer.

Influence of coverage on the cell performance

Chemical bath deposited CdS thin films have a band gap of about 2.4 eV [110] and therefore absorb strongly the short wavelength light with $\lambda \leq 520$ nm. Only about half of the carriers generated in the CdS layer by light absorption contribute to the output current [111,112]. A decrease of the CdS film thickness would reduce a loss in the short circuit current density J_{SC} .

Unfortunately, attempts to decrease the CdS thickness, e.g. by reduction of the deposition time, results in a degradation of cell performance. Figure 4.2 shows the parameters of the solar cells as a function of CdS deposition time. Without the buffer layer, the cell

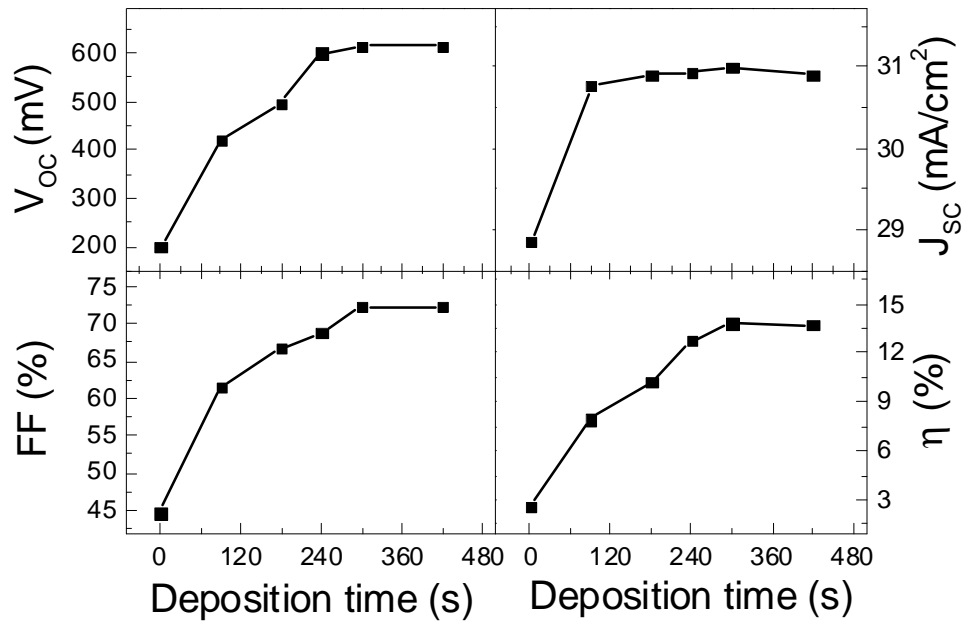


Figure 4.2: Evolution of the cell parameters as a function of the CdS deposition time. The solar cells with the CdS buffer deposited in 5 min obtain the best performance. The decrease of the deposition time aiming to yield thinner CdS results in a dramatic decrease of the open circuit voltage and the fill factor.

efficiencies are quite poor, with low V_{OC} , J_{SC} and FF. This is because of a high surface recombination due to i) a physical damage of the CIGS surface during the ZnO sputtering [113] and ii) unfavorable conduction band alignment between the ZnO and CIGS layer [114]. Solar cells with the CdS buffer deposited in 5 min have the best performance with an efficiency of about 14%. Shorter deposition times result in a strong decrease in V_{OC} and FF. Longer deposition (420 s) results in a slight decrease of J_{SC} .

The evolution of the cell parameters can be explained by the coverage factor. By the XPS measurements, it was deduced that the CIGS absorber layer is completely covered only after a deposition time of CdS of 240 s. On the other hand, the damage by the ZnO sputtering can reach 5 nm depth in the substrate layer [113]. Thus, a CdS deposition time of 300 s is required to protect successfully the underlying CIGS layer.

4.2.2 Deviation from stoichiometry

In general, the CBD-CdS films reported in the literature [113,115-117], contain more Cd compared to S, i.e. the S/Cd ratio is smaller than 1. The origin of the deviation from a 1:1 stoichiometry in the CdS films is still not clear.

The aim of this section is to elucidate the question whether the S/Cd ratio depends on the CBD solution or the interaction of this solution with the CIGS substrate. Influences of the elements of solution chemistry, like NH_3 concentration, the thiourea metathesis and as well the bath temperature, on the S/Cd ratio are investigated.

4.2.2.1 Influence of the NH_3 concentration.

Experiment

CdS films are deposited for different durations onto the CIGS substrate from the chemical bath with different NH_3 concentrations: 1 M (standard recipe) and 1.7 M. Quantitative XPS analysis is applied to derive the S/Cd ratios on the surface of the deposited CdS films.

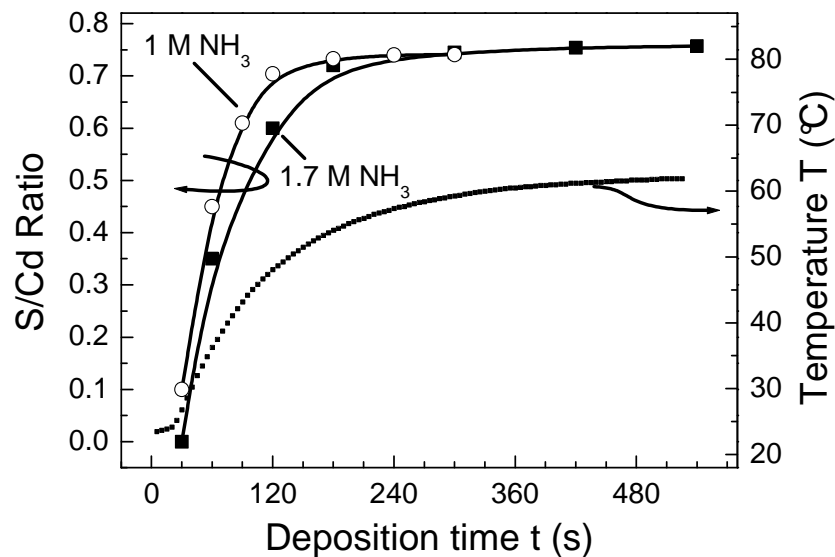


Figure 4.3: The trend of the evolution of the S/Cd ratio as a function of the CBD deposition time for the two different CBD baths: with 1 M (open circles) and 1.7 M NH_3 (full squares). Also displayed is the measured temperature profile in the CBD bath (dotted line).

Results

As shown in Fig. 4.3, in the standard solution with 1 M NH_3 , the S/Cd ratio increases with longer deposition times and tends to saturate at a value of 0.75 after 240 s. Note that this time is the starting point for the complete coverage of the CIGS absorber surface as described in the previous section.

The S/Cd ratio in the case of 1.7 M NH_3 is slightly lower than in the case of the standard solution in the time range of 30-300 s. After 30 s in this solution, the signal of S is even not yet detected on the CIGS substrate whereas the signal of Cd is already clearly visible. The increase of the S/Cd ratio saturates at almost the same value as in the case of 1 M NH_3 . However, it takes longer to reach the saturation in 1.7 M NH_3 solution.

Discussion

Hariskos [113] and Kylner [117] suggested that the creation of impurities from the chemical bath (like e.g. $\text{Cd}(\text{OH})_2$, $\text{Cd}(\text{CN})_2$, CdCO_3) somehow explains the excess of Cd. In this context, it is not possible to explain the experimental observation with varying NH_3 concentration. As will be shown by the calculation in section 4.2, from the thermodynamical point of view, the precipitation of $\text{Cd}(\text{OH})_2$ will be strongly reduced or does not even occur by adding more NH_3 into the CBD solution. Hence, we should expect that the S/Cd ratio of the CdS films deposited in the 1.7 M NH_3 solution is higher than in the standard solution due to a reduction of the $\text{Cd}(\text{OH})_2$ precipitation. Surprisingly, the experimental observations have shown an opposite influence of NH_3 .

This contradiction indicates that the impurities in the CdS film play only a minor role in the S/Cd ratio at the CdS/CIGS interface. In previous XPS investigations [115,116], the formation of compounds like CdSe or CdIn_xSe_y as products of the interaction between the CBD bath and the CIGS layer has been proposed to explain the strong deviation of the S/Cd ratio. The facts that the S/Cd ratio increases with the increase of the coverage and saturates at the same time with the complete coverage support the dominant role of the CIGS substrate. The lower rate of the increased S/Cd ratio in 1.7 M NH_3 solution can be explained by a slower coverage in this case, since a high concentration of NH_3 not only terminates the precipitation of $\text{Cd}(\text{OH})_2$ but also slows down the formation of the CdS film.

4.2.2.2 Influence of the bath temperature

The increase in the S/Cd ratio has been suggested [115] to originate from the gradual heating of the CBD bath (see the temperature profile in Fig. 4.3), since the thiourea decomposition is known to evolve faster at increased temperature. However, the following experiment shows that not only the temperature factor but also the CIGS substrate influences the increased S/Cd ratio.

Experiment

The CdS films are deposited in 60 s sequentially in several times on the same CIGS substrate. Note that the end temperature of the deposition after 60 s is only 35°C compared to 60°C after 300 s of the continuous deposition. After each deposition, the surface composition is analyzed by XPS.

Results

As can be seen from the XPS measurement (Fig. 4.4a), with more time of the deposition, the intensity of S 2s continuously increases with a decrease of the Se 3s signal from the substrate. There is no further change after four times of the deposition. Simultaneously, the signal from the substrate disappears, corresponding to the complete coverage of the CIGS substrate.

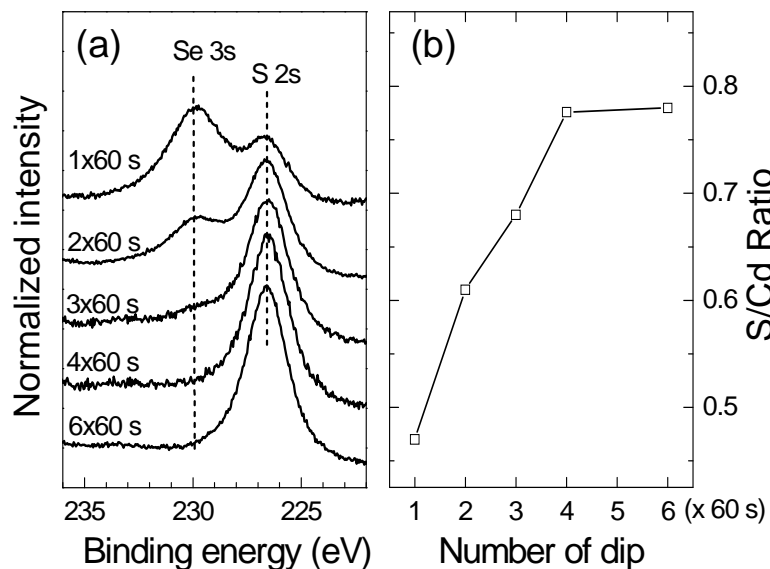


Figure 4.4: a) The evolution of the XPS signals Se 3s from the substrate and S 2s from the deposited CdS after several times of deposition in 60 s; b) the corresponding evolution of the S/Cd ratio.

Figure 4.4b shows the evolution of the S/Cd ratio derived from the XPS measurements. Though the bath temperature of each deposition is the same, this ratio increases with more times of the deposition. It is interesting to note that the increase saturates after four times of the deposition that coincides with the times needed to make the signal of the substrate disappear. Moreover, the saturation value of the S/Cd ratio in this experiment is as high as after 5 min of continuous deposition where the end temperature is much higher. Therefore, it can be concluded that the bath temperature does not play a decisive role in increasing the S/Cd ratio. The increase of this ratio as long as the CIGS surface is present in contact with the CBD-solution points again to the role of their interaction in the observed stoichiometric deviation.

4.2.2.3 Role of the thiourea-Cd(OH)₂ metathesis

Friedlmeier *et al.* [118] have observed precipitation islands by atomic force microscopy after a 30-second chemical bath deposition, whereas no S was detected by XPS. Therefore they postulated these islands to be composed mainly of Cd(OH)₂. A conversion of Cd(OH)₂ into CdS by the metathesis of thiourea can be an important step in the growth of the CdS films (see Section 4.1). It is of interest to examine the role of the thiourea-Cd(OH)₂ metathesis in the trend of increasing the S/Cd ratio.

Experiment

CdS is deposited in 90 s from the standard solution onto the CIGS substrates. Then, the sample with the deposited CdS film is treated in the solution containing only thiourea at 60°C and subsequently the sample surface is analyzed by XPS. The concentration of thiourea used for the treatment is the same in the standard solution for the CdS deposition.

Results and discussion

Figure 4.5a shows the evolution of the XPS region of O 1s on the surface of the CdS film treated for different durations. The intensity of the O 1s peak strongly decrease after 3 min treatment. A treatment of 15 min reduces further the O 1s signal, but with a lower rate. No evident changes in the appearance of the peak shapes are found for the successive treatment times. The treatment results also in a slight increase of the S/Cd ratio from 0.51 to 0.58 after 15 min (Fig. 4.5b).

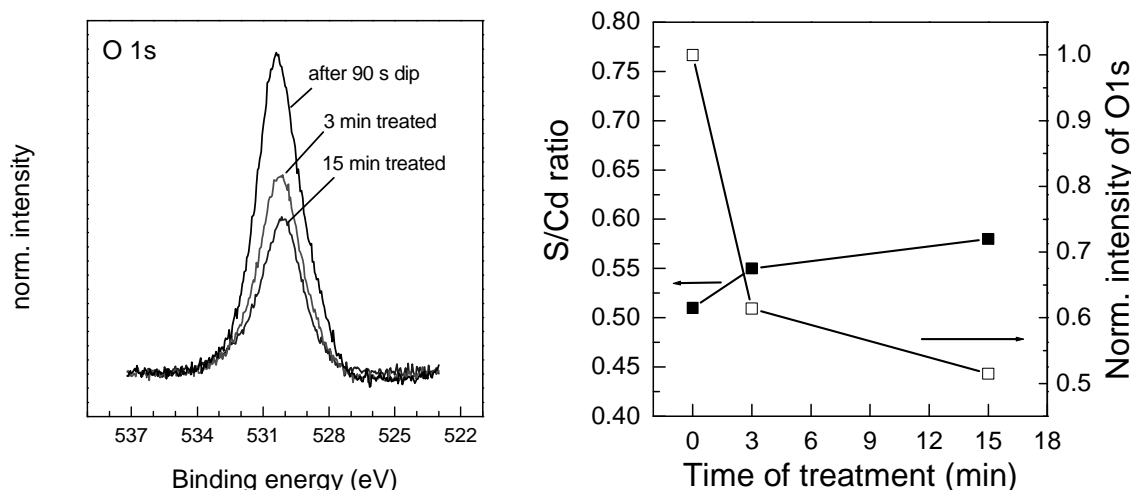


Figure 4.5: Evolution of the O 1s peak (left-hand side) and the S/Cd ratio (right-hand side) versus the treatment time in the solution containing thiourea at 60 °C.

The observations in the experiment with the treatment in the thiourea solution fit well to the process of the thiourea metathesis at the surface of cadmium hydroxide. Due to this reaction, $\text{Cd}(\text{OH})_2$ converts to CdS, and hence the concentration of oxygen on the surface is reduced whereas the amount of S increases. However, the increase of the S/Cd ratio by this process has a much smaller rate compared to that during the standard CdS deposition. Therefore, it can be concluded that the thiourea metathesis does not play a significant role in the increased S/Cd ratio.

After 15 min treatment, the concentration of the hydroxide due to the conversion of $\text{Cd}(\text{OH})_2$ to CdS decreases by a factor of 2 whereas the proportion of CdS increases only by 1.14 times. A quantitative analysis of this relation yields 14% of $\text{Cd}(\text{OH})_2$ fraction and 35% of other Cd-compounds on the sample surface. Note that the saturation value of the S/Cd ratio is 0.75, i.e. the fraction of the $\text{Cd}(\text{OH})_2$ and other Cd-impurities like CdCO_3 , $\text{Cd}(\text{CN})_2$ is 0.25. Then the fraction of Cd-compounds formed from an interaction between CBD solution and the substrate is about 25%.

4.2.3 Crystallography

Figure 4.6 shows the X-Ray diffraction spectra from the CdS films deposited onto different substrates. It can be concluded that there is no preferential crystal orientation in the CdS films deposited onto the glass substrate. Both the hexagonal (wurtzite) as well as the cubic (zinblende) phase exist in the films. The peaks have a large width, indicating a poor crystalline quality in the CBD-CdS film. Using the monocrystalline Si with (111) orientation as a substrate does not influence the structure of the CdS films. However, in the case of using a Si (100) substrate, the cubic phase with the orientations 311 and 222 appears more clearly.

Comparing to the reference data from CdS single crystal (Joint Committee on Power Diffraction Standard: JCPDS), the peaks in the XRD diffraction shift into the region of higher θ (smaller lattice parameters), indicating stress in the grains. The shift is not dependent on the substrates, and hence the stress is caused by impurities in the CdS films rather by an influence of the substrates.

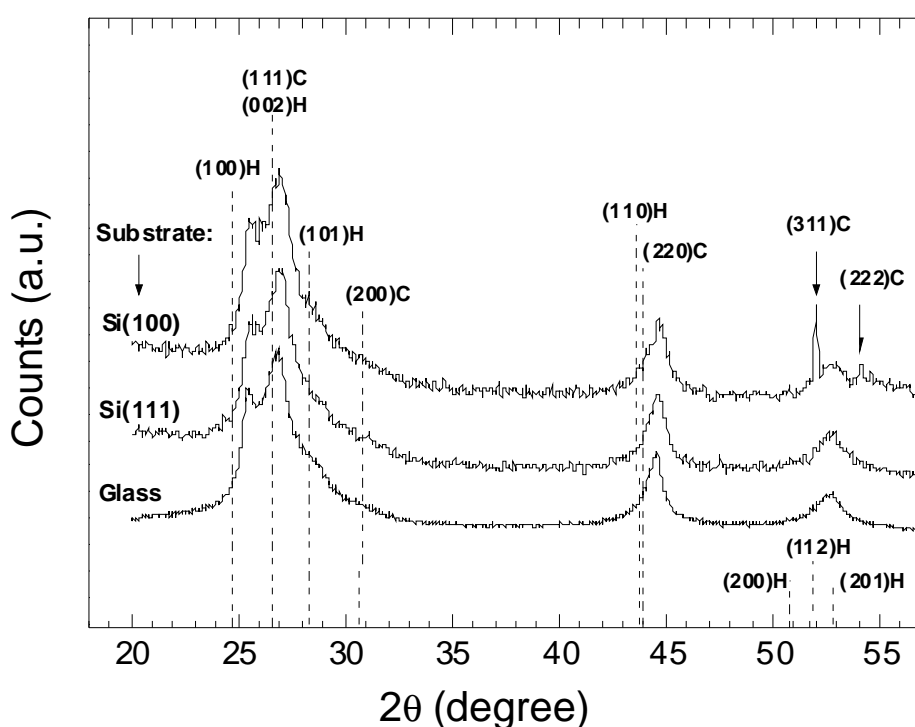


Figure 4.6: X-ray diffraction pattern of the CdS films deposited in 5 min from the standard solution onto the different substrates: glass, monocrystalline Si with orientations (111) and (100). The dotted lines point to the positions of the reference data from CdS single crystal (Joint Committee on Power Diffraction Standard: JCPDS). H and C refer to the hexagonal and cubic phase, respectively.

4.3 Modification of the Cu(In,Ga)Se₂ surface

The deviation of the S/Cd ratio from its 1:1 stoichiometric value at the beginning stage of the CdS deposition can be attributed mainly to two effects:

- i) Co-deposition of impurities like Cd(OH)₂ from the solution on the CIGS surface
- ii) Incorporation of Cd into the CIGS surface layer.

The second effect has attracted a big interest during recent years. Observations of Cd incorporation in a shallow top CIGS layer were reported based on different techniques [119-123]. The authors postulated that it is not the CdS thin film itself, but that the incorporation of the Cd results in the positive effect on the solar cell performance. However, it is still not understood how the CBD solution reacts with the CIGS substrate to introduce Cd into this layer.

In this Section, I will demonstrate that both processes, Cd-diffusion and the formation of Cd(OH)₂ are intimately tied to the CIGS surface reduction-oxidation process and that they are controlled by the [NH₃] concentration used in the chemical bath.

4.3.1 Experiments

CIGS absorbers are treated for 15 min. at 60°C in cadmium acetate (1.4 mM) solutions without and with different [NH₃] concentrations: 0.5 M, 1 M and 1.5 M. After the treatment, the samples are completed with the standard deposition of the CdS and double ZnO window layers.

Secondary ion mass spectroscopy (SIMS) with an oxygen beam of 12.8 keV energy is used to determine the distribution of the diffused Cd in the treated CIGS absorber. The surfaces of the CIGS absorber layers, with and without the treatment, are analyzed by X-ray photoelectron-spectroscopy, using Mg K_α X-rays (1253.6 eV).

4.3.2 Thermodynamical considerations

Partitioning of Cd in the solutions

In ammonia solutions, cadmium ions, Cd²⁺, form different complex species, with hydroxide ions (Cd(OH)_n²⁻ⁿ, n = 1-4), and ammonia (Cd(NH₃)_n²⁺, n = 1-6) corresponding to the reactions



I assume that free Cd^{2+} ions with much smaller size than their complexes would more easily diffuse into the CIGS layer. Therefore, it is a matter of interest to know their concentration in the solutions.

At equilibrium, the partitioning of the cadmium complex species and free $[\text{Cd}^{2+}]$ is determined by the stability products $\beta_{L,n}$ of the complexes given in the Table 4.1 [124]:

$$\beta_{L,n} = \frac{[\text{Cd}^{2+}(\text{L})_n]}{[\text{Cd}^{2+}][\text{L}]^n} \quad (4.2)$$

Table 4.1. Values of the stability constants used in the calculation.

n	$\log \beta_{L,n}$					
	1	2	3	4	5	6
OH^-	4.3	7.7	10.3	12		
NH_3	2.6	4.65	6.04	6.92	6.6	4.9

The concentration of the free Cd^{2+} ions is related to the total concentration of cadmium, $[\text{Cd}]_T$, by

$$[\text{Cd}]_T = \alpha [\text{Cd}^{2+}] \quad (4.3)$$

where α is the overall complexation coefficient given by

$$\alpha = 1 + \sum_L \sum_{n=1}^{n_i} \beta_{L,n} [\text{L}]^n \quad (4.4)$$

The partitioning of free $[\text{Cd}^{2+}]$ in dependence of $[\text{NH}_3]$ calculated for the case of $[\text{Cd}]_T = 1.4$ mM is shown in Fig. 4.7. By adding 0.5 M $[\text{NH}_3]$ into the solution, the concentration of free $[\text{Cd}^{2+}]$ is dramatically reduced from 1.4×10^{-3} to 10^{-9} M and decreases further to 10^{-10} M and 10^{-11} M with increasing $[\text{NH}_3]$ to 1 M and 1.5 M, respectively. Thus, if Cd-diffusion depends only on the concentration of free Cd^{2+} ions, which has much smaller size than the Cd^{2+}

complexes, its quantity should have a maximum in the case without NH_3 and should decrease with an increase of $[\text{NH}_3]$ in the solution.

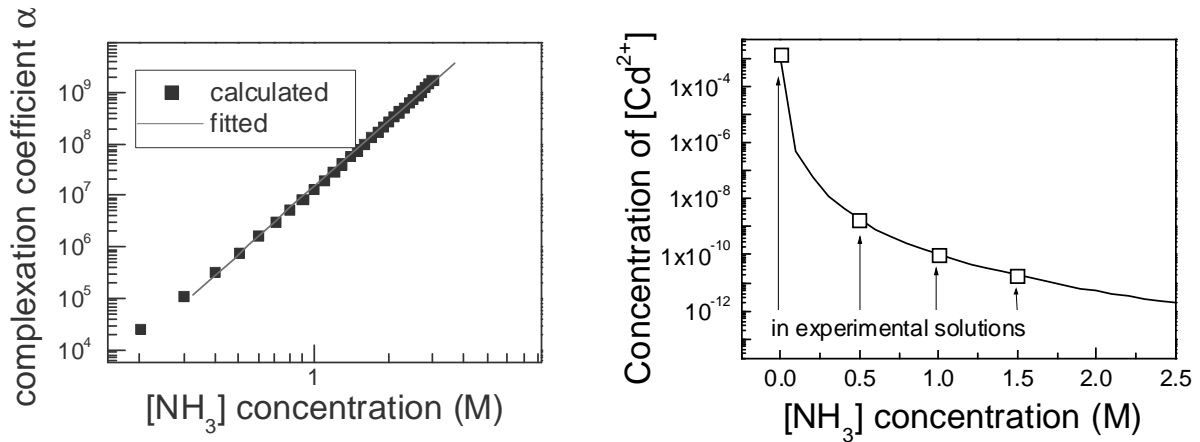


Figure 4.7: Left-hand side: Dependence of the overall complexation coefficient on NH_3 concentration (dots) and fitted line by $\alpha = 10^{7.15} [\text{NH}_3]^{4.28}$. Right-hand side: The partitioning of free Cd^{2+} in the ammonia solution containing 1.4 mM of $[\text{Cd}]_T$.

Precipitation of $\text{Cd}(\text{OH})_2$

Another important point is the formation of $\text{Cd}(\text{OH})_2$ on the CIGS surface and its influence on the solar cell performance. Now, we consider the thermodynamic condition for the precipitation of $\text{Cd}(\text{OH})_2$. The $[\text{OH}^-]$ concentration, i.e., the pH of the ammonia solution, is controlled by the acid-base equilibrium



with $\text{pK}_B = 4.8$ [124].

With $\text{pK}_S = 14.3$ for $\text{Cd}(\text{OH})_2$ [124], the precipitation line of cadmium hydroxide calculated as a function of the ammonia concentration is shown in Fig. 4.8. The part above the the solid line corresponds to the concentration zones of $[\text{Cd}]_T$ and $[\text{NH}_3]$ where $\text{Cd}(\text{OH})_2$ precipitates, whereas in the shaded part of the figure all introduced cadmium salt is fully dissolved. For 1.4 mM $[\text{Cd}]_T$ (standard concentration for our CdS deposition and used for Cd-pretreatment, dashed line), $\text{Cd}(\text{OH})_2$ will precipitate if the $[\text{NH}_3]$ concentration is lower than 0.7 molar and

will dissolve when more NH_3 is added.

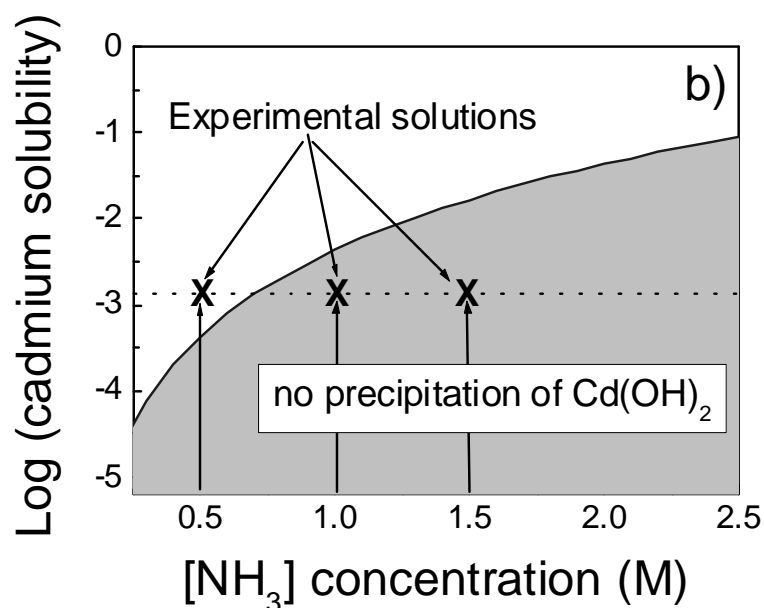


Figure 4.8: Solubility diagram of $\text{Cd}(\text{OH})_2$ as a function of NH_3 concentration

4.3.3 Chemical analysis

Cd-diffusion into the CIGS

Figure 4.9 shows the SIMS depth profile of Cd in the CIGS absorber layer treated in Cd-solutions without NH_3 (full line), with 1M (dashed line) and 1.5 M $[\text{NH}_3]$ (dotted line). In contrast to our expectations, almost the same amount of Cd is observed in the CIGS absorber in both cases of using 1 M and 1.5 M $[\text{NH}_3]$. Moreover, Cd-diffusion is significantly weaker in the absence of NH_3 , although the concentration of free $[\text{Cd}^{2+}]$ in the solution in this case is some orders of magnitude higher as shown before. I do not observe significant change in the Cu profiles after the treatment. Thus, an introduction of Cd into the CIGS in our experiment is related to another process, e.g., to an adsorption of anions onto the surface, rather than to the dissolving Cu.

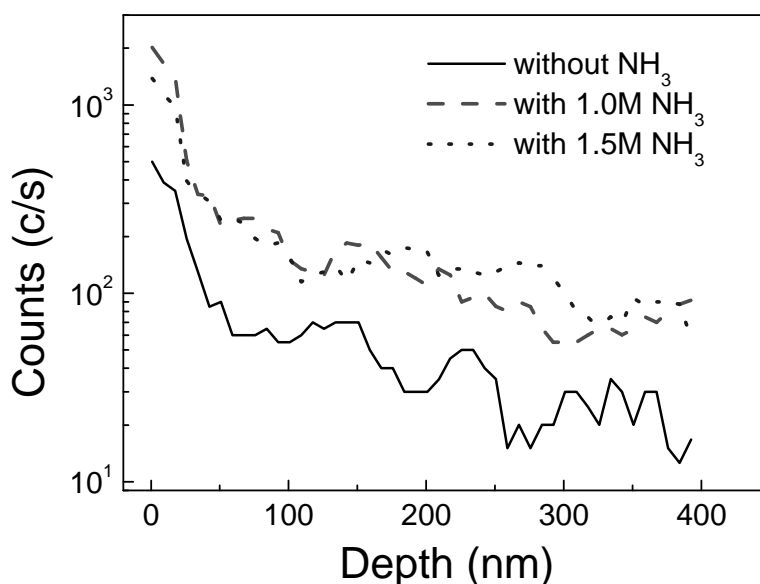


Figure 4.9: SIMS depth profiles of Cd in the CIGS absorber layers treated in the Cd-solutions: without NH₃ (full line), with 1M [NH₃] (dashed line) and 1.5 M [NH₃] (dotted line).

Surface modification

Figure 4.10 displays the XPS spectra of elements on the CIGS surface before and after the Cd-treatments. Cd is observed on the surface of all the treated samples. The highest amount of Cd appears in the case of the treatment in 0.5 M NH₃ (Fig. 4.10b). The Auger parameter of Cd for this case is 785.15 eV, indicating the presence of Cd(OH)₂ (=785.1 eV, [93]). From the thermodynamical consideration in the previous section, Cd(OH)₂ is also expected to precipitate in this solution. On treatment in 1.5 M NH₃ solution, the Cd Auger photoemission peak shifts to higher kinetic energy (Fig. 4.10a). The Auger parameter of Cd in this case is 786.3 eV and close to that of CdSe (=786.7 eV, [93]).

Due to the short exposure to air after the preparation, the CIGS surface is oxidized and the O 1s signal has a peak at 530.85 eV (Fig. 4.10c). Based on the equilibrium condition, the precipitation of Cd(OH)₂ is expected in the 0.5 M [NH₃] solution. In this case, a decrease in intensity observed for all signals of Cu 2p_{3/2}, In (MNN) and Se 3d implies that the CIGS surface is covered by an over-layer of Cd(OH)₂. Consequently, the shifted O 1s signal observed at 530.35 eV belongs to oxygen in the hydroxide group. Moreover, it can be seen that the XPS peaks of the elements are significantly changed due to the treatment: the Cu 2p_{3/2}

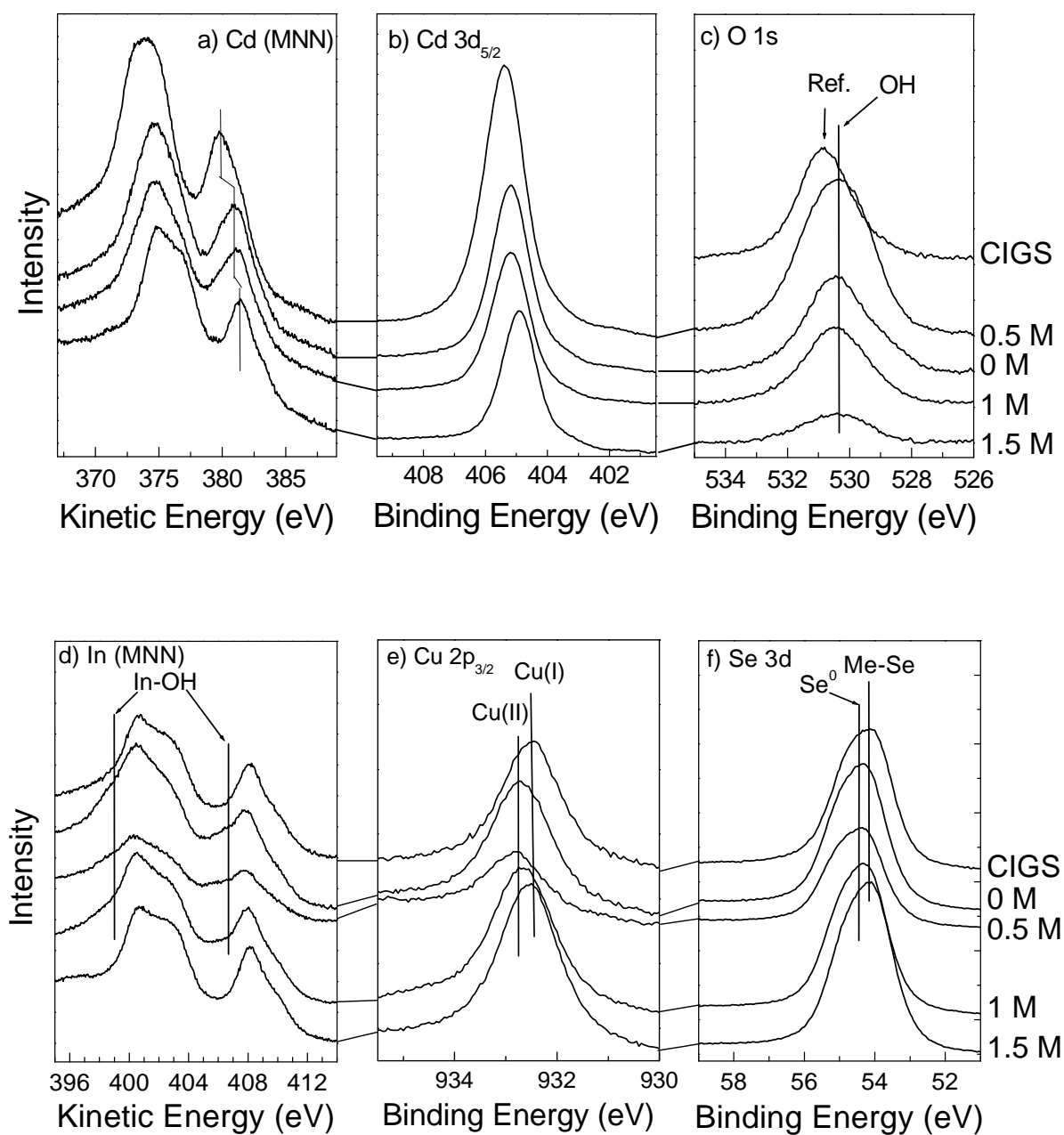


Figure 4.10: The XPS spectra of the elements on the CIGS surface: a) Cd MNN, b) Cd $3d_{5/2}$, c) O 1s, Cu $2p_{3/2}$, In (MNN), and Se 3d without and with Cd-treatment in the solutions with varying $[\text{NH}_3]$: 0 M, 0.5 M, 1.0 M and 1.5 M.

and the Se 3d peaks are shifted and expanded to the higher binding energy, and the In (MNN) signal is flattened at 406 eV. The same behavior of the XPS spectra is also reported in Ref. [125] when the CIGS is oxidized in air and in an environment with high humidity, where it was attributed to the formation of Cu(II), In-O bond, and elemental Se on the CIGS surface. The connection between the shift in the binding energy of core levels and the chemical environment can be explained by the charge potential model [91], where the increase in binding energy accompanies the increase in the formal oxidation states of atoms. An adsorption of charges on the surface can shift the Fermi level at the surface and lead to an equal shift in all core level binding energies. However, the position of the Auger peaks In (MNN) remains unchanged after the treatment, and this result excludes an influence of the charge accumulation on the sample surface on the core level shifts.

The CIGS surface oxidation is also observed by the treatment in the solutions without NH_3 and with 1 M $[\text{NH}_3]$. All the above mentioned peaks locate at the same binding and kinetic energy as in the case of 0.5 M $[\text{NH}_3]$ but with higher intensities. This result indicates that the formation of $\text{Cd}(\text{OH})_2$ in both these cases is less. Nevertheless, the presence of the O 1s peak at 530.35 eV implies that some hydroxide groups are still bound to the CIGS surface. The amount of hydroxide is strongly reduced in the case of using 1.5 M $[\text{NH}_3]$, and the signals of oxidized species of the CIGS surface disappear.

4.3.4 Solar cell performance

Figure 4.11 compares the performance of the solar cells pre-treated in the Cd-solutions with that of the reference cell without treatment. A decrease in open circuit voltage V_{OC} and Fill Factor FF is observed in all treated cells with different degrees depending on the $[\text{NH}_3]$ concentration used in the solution. This result implies that both the formation of hydroxides on the CIGS surface and the Cd-diffusion are unfavorable for solar cell performance. The treatment with 1M and 1.5 M $[\text{NH}_3]$ introduce more Cd into the CIGS and the cell performance is degraded more strongly compared to the treatment without NH_3 . The formation of hydroxides on the CIGS surface contributes additional degradation effects in the case of the treatment with 1M compared to the case with 1.5 M $[\text{NH}_3]$.

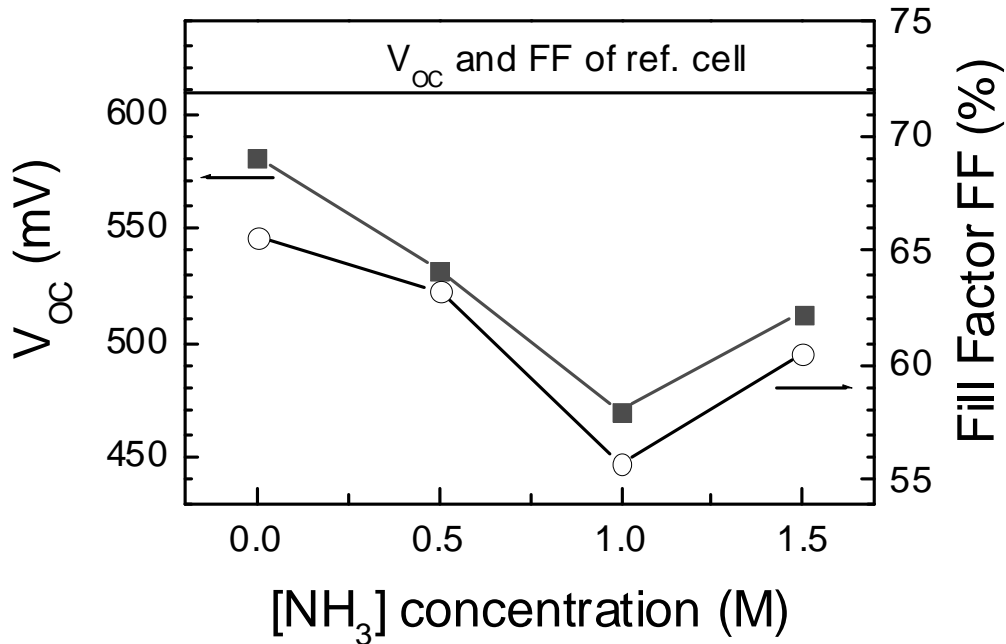
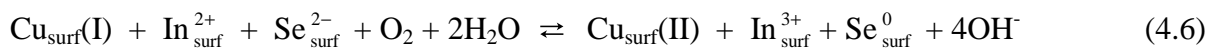


Figure 4.11: The best performance of the solar cells with pre-treatment in the Cd-solutions as compared to the reference cell (untreated): V_{OC} (full squares) and FF (open circles).

4.3.5 Discussion

Based on the XPS results, I propose a model to explain the observed dependence of the Cd-diffusion and the formation of $\text{Cd}(\text{OH})_2$ on the $[\text{NH}_3]$ concentration used in the solution. Both processes are intimately tied to the CIGS surface oxidation which is controlled by pH, i.e. by $[\text{NH}_3]$ concentration. The following three processes as described in Fig. 4.12 are involved when the CIGS absorber film is dipped into the Cd-solution:

- (1) Cd^{2+} ions adsorb at the CIGS surface, probably at the V_{Cu} site. They can either create a bond with Se to form CdSe and/or diffuse into the CIGS film. Simultaneously, the hydroxide groups adsorb at the In and Cu ions on the CIGS surface to balance the charge in the solution.
- (2) the CIGS surface is oxidized by oxygen dissolved in the solution under formation of hydroxide



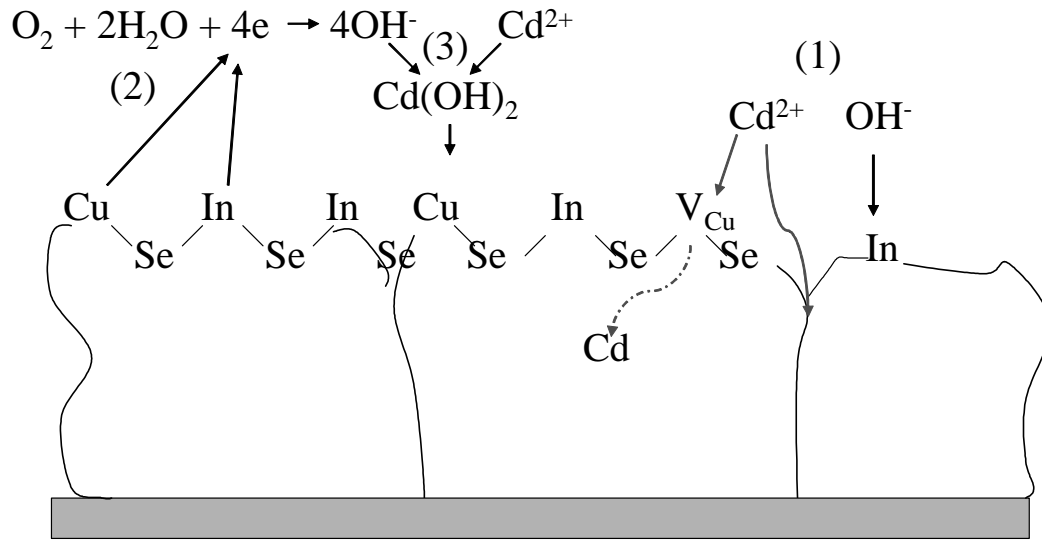


Figure 4.12: Schematic representation of the processes occurring when the CIGS layer is treated in a Cd-solution.

(3) precipitation of $\text{Cd}(\text{OH})_2$:



In the solutions without NH_3 , the pH value is close to 7, and therefore the hydroxide concentration is too small to form $\text{Cd}(\text{OH})_2$. However, at low pH, reaction (4.6) occurs strongly and quickly to create an additional amount of hydroxide, whereas the diffusion of the Cd into the CIGS film occurs more slowly. Consequently, close to the CIGS surface region, the product $[\text{Cd}^{2+}][\text{OH}^-]^2$ exceeds the solubility product of $\text{Cd}(\text{OH})_2$. Therefore, in spite of high free $[\text{Cd}^{2+}]$ in the solution, almost all Cd^{2+} ions precipitate in form of $\text{Cd}(\text{OH})_2$ (reaction 4.7) on the surface and only a small amount can diffuse into the CIGS film.

In the solution with 1.5 M $[\text{NH}_3]$, the $[\text{OH}^-]$ is higher. Following the principle of Le Chatelier, reaction (4.6) is slowed down or even terminated. Consequently, the precipitation of $\text{Cd}(\text{OH})_2$ induced by reaction (4.6) occurs slowly. In this case, the adsorbed Cd^{2+} ions can

diffuse further into CIGS. Following this model, the CIGS absorber treated in 1 M $[\text{NH}_3]$ solution should contain more diffused Cd than in the case without NH_3 and more hydroxide on the CIGS surface than in the case of 1.5 M $[\text{NH}_3]$. The experimental results support well this model.

5 The In(OH,S) buffer device

One of the ways to improve further the cell performance is replacing the standard CdS buffer by more transparent, preferably also less toxic buffers. Though many attempts of using alternative materials were reported with efficiencies more or less close to that of the standard device, their developments were normally approached by “trial and error” experiments. Hence, a number of questions concerning stability and lack of efficiency compared to the CdS buffer device are still open. The aim of this Chapter is not to try new recipes for the alternative buffers, but an approach to find the answers to those questions in the case of the well known CBD-In(OH,S) buffer. Comparing the chemical and electronic properties of the CdS and In(OH,S) buffers indicates that poor performance as well as metastabilities of the solar cells with the In(OH,S) buffer are predominantly controlled by properties of the ZnO/In(OH,S) interface. A treatment of the In(OH,S) buffer surface with Cd- or Zn-solutions strongly improves and stabilizes the cell performance. An electronic model derived by numerical simulation is proposed to explain influences of defects at this interface.

5.1 Characteristics of the In(OH,S) buffer

5.1.1 Solution chemistry

In the solution containing InCl₃ and thioacetamide, In₂S₃ precipitates due to reaction between the indium ions and H₂S. The latter is formed from the hydrolysis of thioacetamide given by

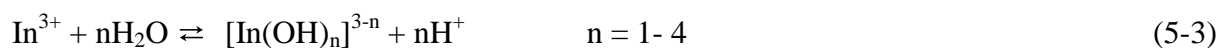


This reaction depends strongly on temperature and pH of the solution. Swift and Butler [126] found that the reaction kinetics is time-dependent in second order

$$-\frac{d[\text{CH}_3\text{CSNH}_2]}{dt} = k [\text{CH}_3\text{CSNH}_2][\text{H}^+] \quad (5-2)$$

where $k \approx 0.21 \text{ l mol}^{-1} \text{ min}^{-1}$ at 90°C.

Besides the formation of indium sulfide, $\text{In}(\text{OH})_3$ can precipitate due to the hydrolysis of In^{3+} in an aqueous medium. As is the case for cadmium, In^{3+} forms different complexes with hydroxide groups



The stability constants β of the complexes in Table 5.1 [127] are given by

$$\beta = \frac{[\text{In}(\text{OH})_n^{3-n}][\text{H}^+]^n}{[\text{In}^{3+}]} \quad (5-4)$$

Table 5.1: *Stability constants of the complexes $\text{In}(\text{OH})_n^{3-n}$*

	InOH^{2+}	$\text{In}(\text{OH})_2^+$	$\text{In}(\text{OH})_3$	$\text{In}(\text{OH})_4^-$
Log β	-4.42	-8.3	-12.4	-22.07

With the solubility product of $\text{In}(\text{OH})_3$, $\text{pK}_s = 36.92$ [127], Figure 5.1 gives the precipitation line of $\text{In}(\text{OH})_3$ in dependence of pH in the solution. In the zone under the curve, $\text{In}(\text{OH})_3$ is not formed. The upper zone (gray) corresponds to the conditions of the solutions (pH and total concentration of In salt added into the solution) where $\text{In}(\text{OH})_3$ precipitates. The star in the precipitation zone corresponds to the parameters of the CBD solution used in this work (0.005 M InCl_3 and pH = 3.3), and hence we can expect that $\text{In}(\text{OH})_3$ will be formed.

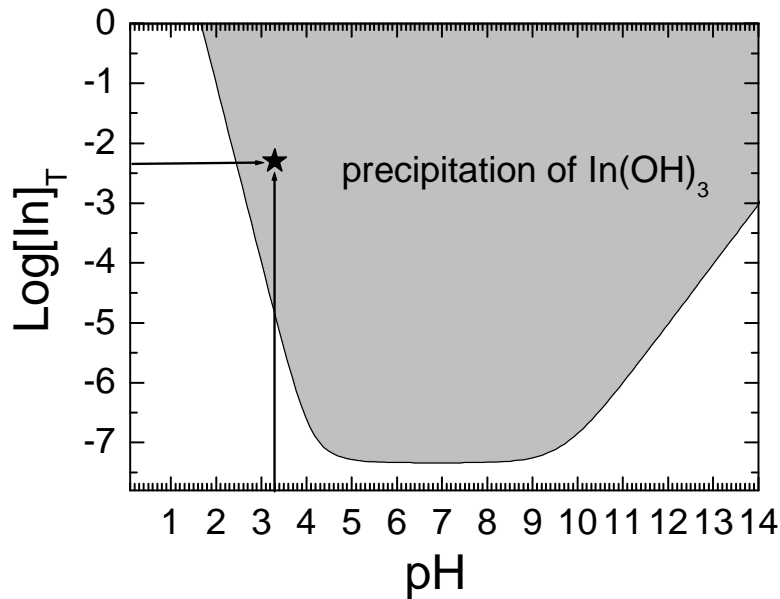


Figure 5.1: Solubility of In(OH)_3 in the aqueous solutions with different pH values. The gray area above the curve corresponds to the region of In concentration and pH where In(OH)_3 precipitates. The star corresponds to the condition in the solution for In(OH,S) deposition used in this work (0.005 M InCl_3 and $\text{pH} = 3.3$).

5.1.2 Buffer properties

The SEM pictures in Fig. 5.2 reveal the different structures of the CdS and In(OH,S) films deposited onto the CIGS substrate. The CdS film, deposited within 5 minutes onto the CIGS substrate, has a polycrystalline structure with a thickness of about 50 nm. The film consists of grains with 10-15 nm size, which are grown on the substrate mainly by the atom-by-atom mechanism [128]. However, larger CdS particles, formed simultaneously in the solution, can also be incorporated in the film (the big particle on the CdS surface in Fig. 5.2a).

In contrast, the growth mechanism of the In(OH,S) buffer appears to be an aggregation of colloidal particles, resulting in the formation of the film with an amorphous structure (Fig. 5.2b). The In(OH,S) buffer, deposited in 15 min, with a thickness of about 15 nm is much thinner than the standard CdS buffer. Nevertheless, XPS measurements of In(OH,S) covered CIGS do not detect any signal from the CIGS substrate, indicating that the absorber layer is completely covered by the In(OH,S) buffer.

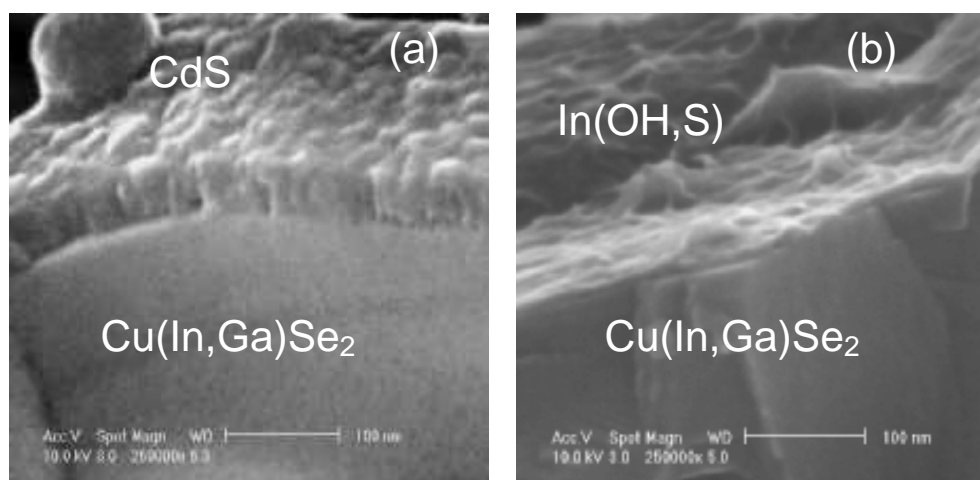


Figure 5.2: SEM picture revealing an amorphous structure of the In(OH,S) film grown on the Cu(In,Ga)Se_2 . The bar corresponds to 100 nm.

The XPS measurements show that both buffer layers contain oxygen-related impurities. An average amount of oxygen of 10-15 at.% is observed in the bulk of the CdS buffer, and the oxygen at the surface is mostly bonded to carbon [129]. In the case of the In(OH,S) buffer, besides a formation of In_2S_3 , a competitive precipitation of hydroxide occurs due to pronounced hydrolysis of InCl_3 in the aqueous medium, and hence a large amount of oxygen in hydroxide is found in the bulk and on the surface of this buffer. Indeed, quantitative analysis by XPS of our In(OH,S) buffer surface gives an O:In:S ratio of 34.1:38.3:27.6.

Figure 5.3 shows a typical signal of O 1s observed by XPS measurement of the In(OH,S) buffer surface. The spectrum can be fitted by two peaks, a small one centered around 529.9 eV and a larger one at 531.7 eV, corresponding to oxide and hydroxide, respectively. The observation by XPS of hydroxide and oxide signals at similar binding energies was reported earlier for an In(OH,S) buffer deposited in the chemical bath at lower pH value (pH = 1.7) [130] than the pH value of 3.3 used in this work.

The In(OH,S) buffer is more transparent than the standard CdS buffer. From the transmission and reflection measurements, the optical band gap energies of the CBD-CdS and In(OH,S) are estimated from Fig. 5.4 to be 2.42 eV and 3.1 eV, respectively. The involvement of a large fraction of hydroxides in the film could be a reason why the In(OH,S) buffer layer has a larger optical bandgap than In_2S_3 (2.2 eV, [131]). From the optical point of view, the large band gap makes the In(OH,S) buffer very interesting for buffer layer applications.

However, as it will be shown in the next section, the optical advantage of the In(OH,S) is offset by electrical losses caused by defects in this film.

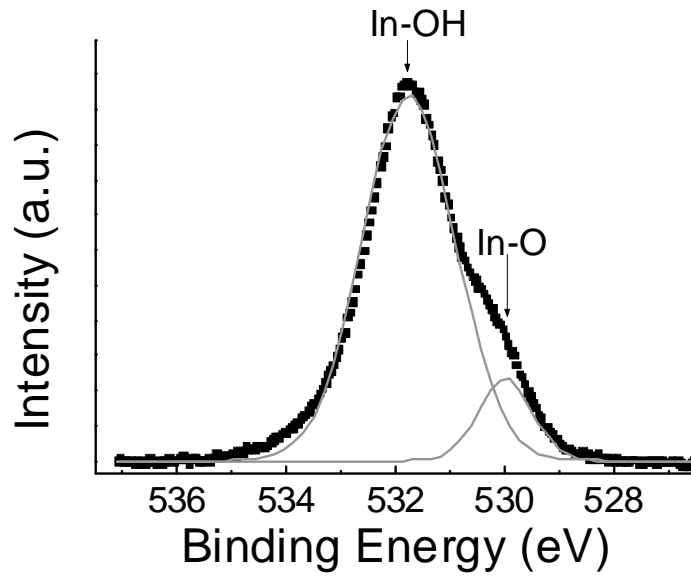


Figure 5.3: XPS spectrum of O 1s on surface of the In(OH,S) buffer layer.

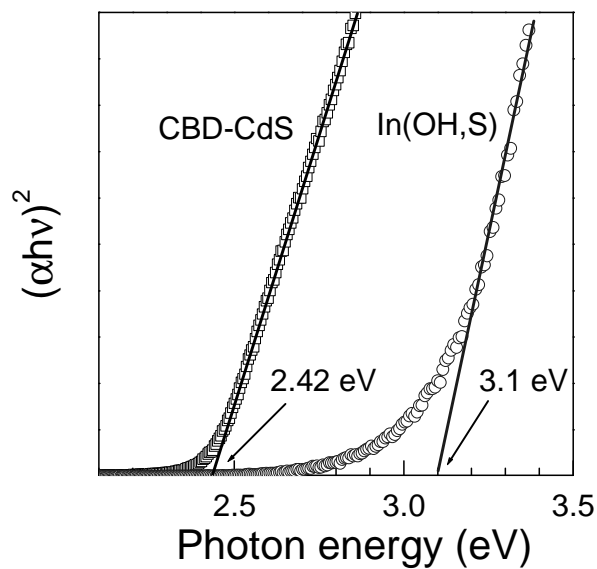


Figure 5.4: Dependence of optical absorption on photon energy for CBD-CdS and In(OH,S) thin films.

5.2 Characteristics of the solar cell with the In(OH,S) buffer

As-prepared solar cells with In(OH,S) buffer have quite a poor performance with typical efficiency of only around 1% (see Fig. 5.5). Air annealing at 200°C improves remarkably the cell efficiency from 1% to 10%. Heat treatment influences differently the solar cell parameters. Open circuit voltage and Fill Factor increase gradually with annealing time, and the increase seems saturate after 40 min of annealing. The short circuit current jumped strongly already after 3 min annealing, reached the highest value after 10 min and decreased slightly with longer annealing.

Light soaking the sample under simulated solar spectrum (AM 1.5, 100 mW/cm² illumination) improves further all the parameters (the circles in Fig. 5.5). After 30 min of light soaking, the efficiency of the In(OH,S) buffer solar cell reaches 12.64 %, i.e. close to the efficiency of the reference standard CdS cell (13.2%). However, the effects of annealing and light soaking are reversible, i.e. the cell performance deteriorates again on storing the samples in the dark for few weeks.

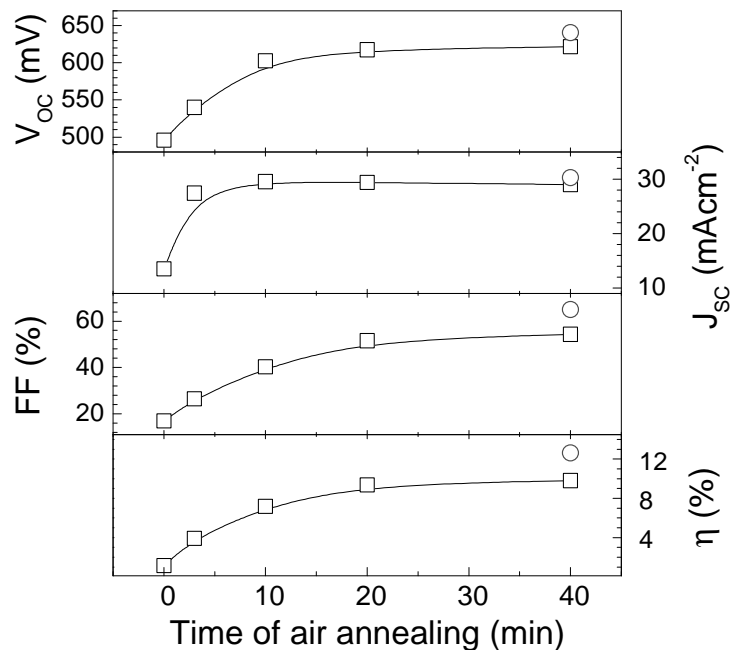


Figure 5.5: Evolution of the performance of the In(OH,S) buffer solar cell upon air annealing at 200°C (open squares). The open circles correspond to the parameters of the cell annealed for 40 min in air and soaked for 30 min under illumination of white light .

5.3 Role of the heterointerfaces

Explanations for difficulties to replace CdS by the alternative buffers in the literature are mainly focused on the interface between the buffer and the CIGS absorber. It is suggested that the presence of Cd at this interface is favorable for the heterojunction formation. However, the entire buffer layer is part of the space charge region of the heterojunction, and hence any imperfection not only at the buffer/CIGS interface but also in the bulk of the buffer and/or at the buffer/ZnO interface can influence the electronic properties of the heterojunction. Thus, an analysis whether the reduced performance of the In(OH,S) buffer materials originates from either of its interfaces or from its bulk properties is essential.

This Section provides evidence for the dominant influence of the interface between the In(OH,S) buffer and the ZnO window layer on the performance and on the metastable electronic behavior of the solar cell. In order to separate the effects of the two interfaces, I investigate double buffer structures that use CdS/In(OH,S) as well as In(OH,S)/CdS combinations. In this way, I obtain devices where the buffer/window and the buffer/absorber interface are made up by different buffer materials. The electronic properties of these double buffer devices are compared to those of devices with single layers of CdS or In(OH,S) buffers. Surprisingly, the behavior of ZnO/CdS/In(OH,S)/CIGS heterojunctions comes close to that of the standard CdS-buffered device with its high photovoltaic performance, whereas ZnO/In(OH,S)/CdS/CIGS rather resembles the device with a single In(OH,S) buffer. Hence, devices that share the material towards the ZnO window layer exhibit a similar performance.

5.3.1 Experiments with double buffers

Two series of devices are fabricated with different double buffer combinations by sequentially depositing either CdS on In(OH,S) or the other way around. In the following, I denote the combination In(OH,S)/CdS/CIGS *type A* and CdS/In(OH,S)/CIGS *type B* double buffers. The thickness of the CdS layer of the double buffer devices is varied by the deposition time. In the first series, the solar cells are completed by sputtering a bilayer ZnO window (i-ZnO/Al:ZnO) and evaporated Al grid contact. In the second series of the samples, the i-ZnO layer is omitted. A schematic representation of the two types of devices is shown in Fig. 5.6.

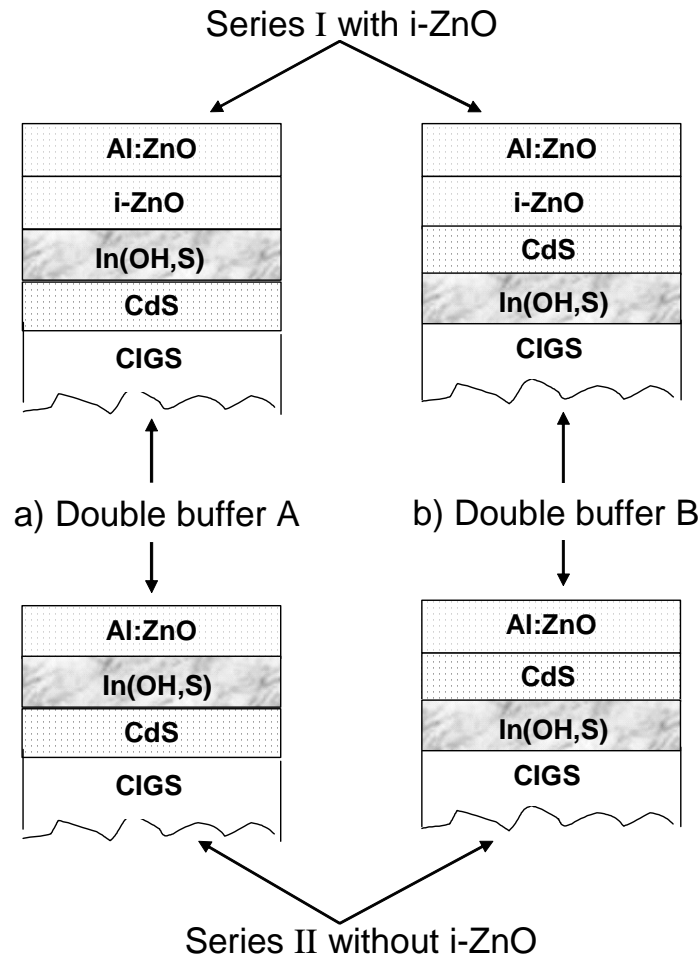


Figure 5.6: Schematic representation of the investigated samples with different buffer structures: a) with the double buffer type A, where a CdS layer separates the In(OH,S) and CIGS layers, b) with the double buffer type B, where a CdS layer separates the In(OH,S) and ZnO layers. Samples in series II differ from those in series I by omitting the i-ZnO layer. The thickness of the CdS layer in both types of the double buffer devices is varied by its deposition time.

5.3.2 Solar cell performance

Although the In(OH,S) buffer has quite different properties in the bulk and at both interfaces compared to the CdS, a comparison of the cell parameters of the double buffer devices will show that the In(OH,S)/ZnO interface predominantly controls electronic loss processes in the In(OH,S) buffer device.

Open circuit voltage

Figure 5.7 shows the open circuit voltage V_{OC} taken from the I/V measurements under illumination for samples with and without i-ZnO layer. The as-grown device with single In(OH,S) buffer and double ZnO-window exhibits a poor performance with much lower V_{OC} and FF compared to those of the standard CdS device (dotted line). Let us first consider the parameters of the sample series that includes the i-ZnO (full squares). Putting a thin CdS film in between the In(OH,S) and the CIGS absorber layers in the *type A* double buffer devices (left hand side) strongly improves V_{OC} to a level that is even higher than that of the reference CdS device. At this point a likely explanation would be [132] that replacing the In(OH,S)/CIGS interface by the CdS/CIGS interface implies a reduction of interface recombination. Interestingly, even the smallest CdS deposition time of 1 min is sufficient to achieve the increase of V_{OC} , whereas with further increasing CdS thickness V_{OC} slightly re-decreases.

Turning now to the *type B* double buffer devices (right hand side of Fig. 5.7), we also

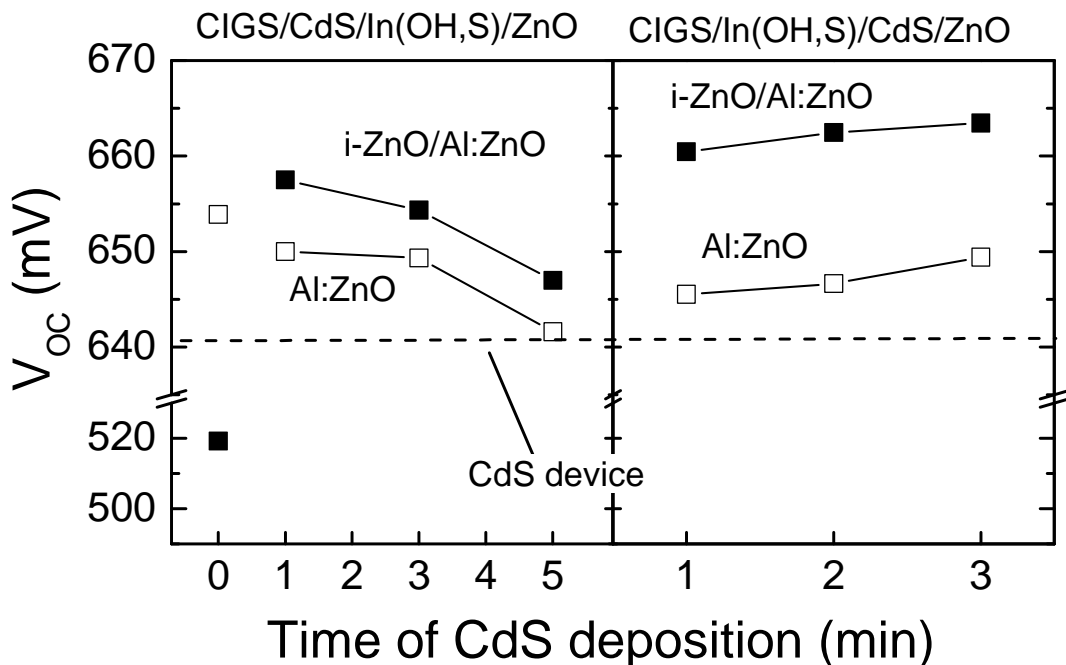


Figure 5.7: Open circuit voltages V_{OC} of the devices with double buffers type A (left hand side) and type B (right hand side) in comparison with those of the reference CdS (dotted line) and single In(OH,S) buffer devices (CdS deposition time is zero).

observe an improvement of V_{OC} by the insertion of the CdS-layer (now between the In(OH,S) and the ZnO window). This improvement is similar to that achieved with the *type A* devices but now increases further with increasing CdS thickness. In this situation, a reduction of recombination at the buffer/absorber interface (that is still In(OH,S)/CIGS) cannot explain the V_{OC} improvement. Instead, I conclude that the CdS/i-ZnO interface is less defective and hence less electronically charged than the In(OH,S)/i-ZnO interface. As will be shown in section 5.5, charges at the buffer/window interface can control the recombination rate at the buffer/absorber interface via electrostatic interaction. Thus, the degradation of V_{OC} observed in single layer In(OH,S) devices is a combined result of a high defect density at the buffer/absorber interface and a high negative charge density at the buffer/window interface. Note that the omission of the i-ZnO layer results in a slight decrease of V_{OC} in both series of samples, and this could be explained by an inhomogeneity of absorber as suggested for the CdS device [133].

Figure 5.8 shows the Arrhenius plots of $n \times \ln(J_0)$ versus the inverse thermal energy $1/kT$ for some devices. The activation energy E_A extracted from the Arrhenius plots for the standard CdS device is 1.13 eV (full squares in Fig. 5.8), close to the absorber band gap energy $E_g = 1.15$ eV derived from spectral quantum efficiency measurements. This coincidence supports the dominant recombination in the bulk of the absorber material. In contrast, we find $E_A = 0.78$ eV in the case of the In(OH,S) buffer device with the bilayer window (full circles in Fig. 5.8) which suggests the dominant interface recombination with $E_A = \Phi_b^p$, where Φ_b^p is the barrier for holes at the interface. However, bulk recombination appears to dominate again in case of the In(OH,S) buffer device *without* the i-ZnO layer ($E_A = 1.10$ eV) and in the double buffer B device ($E_A = 1.16$ eV). This observation clearly indicates a participation of the i-ZnO/In(OH,S) interface in the deterioration of V_{OC} .

It is interesting to note that $E_A \approx E_g$ is also observed in the case of the double buffer A device *with* the bilayer window ($E_A = 1.20$ eV). This finding implies that, though the defect density at the i-ZnO/In(OH_x,S_y) interface is large, it is not sufficient to deteriorate V_{OC} . The In(OH,S) buffer needs an additional number of acceptor defects at the In(OH,S)/CIGS interface to reduce Φ_b^p below a critical value from which the interface recombination becomes dominant. This conclusion implies further that the defect density at the CdS/CIGS interface is lower than that at the In(OH,S)/CIGS interface.

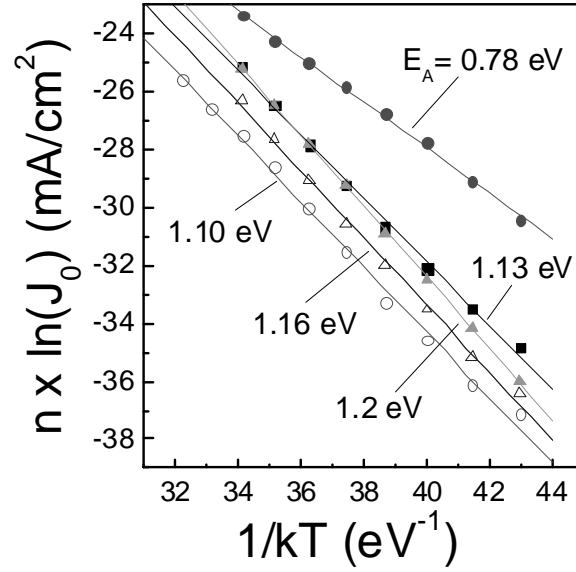


Figure 5.8: Corrected Arrhenius plot of the saturation current density J_0 versus $1/kT$ of: the standard CdS device (closed squares), double buffer A CdS/In(OH_xS_y)/i-ZnO (closed triangles), double buffer B In(OH_xS_y)/CdS/i-ZnO (open triangles), In(OH_xS_y)/i-ZnO (closed circles), In(OH_xS_y)/Al:ZnO (open circles). The straight lines are fits to Eqn. (3.4).

Fill Factor

Exclusion of the In(OH,S)/CIGS interface in the *double buffer A* devices increases the fill factor FF with increasing CdS film thickness. However, the increase of FF seems to saturate at a relatively low level of 55 % (for devices *with* i-ZnO) and of 67-68 % (for devices *without* i-ZnO). In contrast, the *double buffer B* devices have (after a CdS deposition time of 3 min) fill factors up to FF ≈ 72 % that are comparable to those of the CdS-buffer devices. The moderate fill factors that are possible as long as In(OH,S) is present at the buffer/window interface points to the fact that a barrier for photocurrent is formed at this interface. Such a barrier that hinders photocarrier collection, again, is a consequence of negative charges at the buffer/window interface.

The results from our sample series that omits the low-doped i-ZnO nicely fit into the above picture. We observe higher fill factors in all devices with In(OH,S)/ZnO interface when

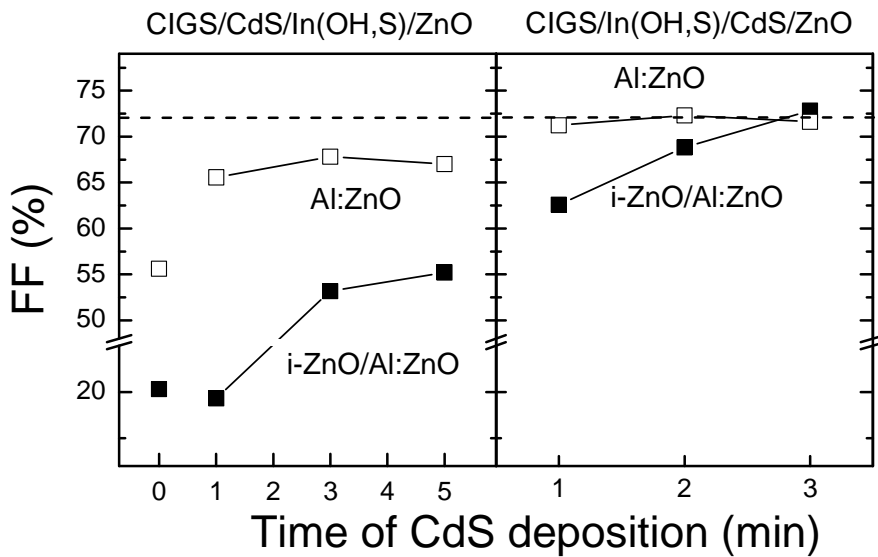


Figure 5.9: Fill Factors FF of the devices with double buffers type A (left hand side) and type B (right hand side) in comparison with those of the reference CdS (dotted line) and single In(OH,S) buffer devices (CdS deposition time is zero).

omitting the i-ZnO layer, i.e. bringing the highly doped Al:ZnO layer closer to the buffer/window interface reduces the aforementioned barrier. The same effect, but much smaller, is also observed in the *double buffer B* devices, perhaps due to an incomplete coverage of the In(OH,S) buffer by the CdS films deposited in a short time.

Internal Quantum Efficiency

The influence of the In(OH,S)/CIGS and In(OH,S)/ZnO interfaces on the electronic properties of the junctions is more clearly seen by analyzing the internal quantum efficiency (IQE) of the samples. As shown in Fig. 5.10, the IQE curve of the single In(OH,S) buffer device is much lower than that of the standard CdS device. In the *double buffer A* devices, the spectral response increases by insertion of a very thin CdS film, deposited in 1 min (≈ 5 nm), in between the CIGS and In(OH,S) layers. However, longer CdS deposition times of 3-5 min are needed to bring the IQE of *type A* double buffer devices close to the IQE of the CdS reference cell. It is important to notice, that the differences among the IQE curves in Fig. 5.10a are dependent on the wavelength and more pronounced in the long wavelength region. Hence, the replacement of the In(OH,S)/CIGS interface by the CdS/CIGS interface results not only in a

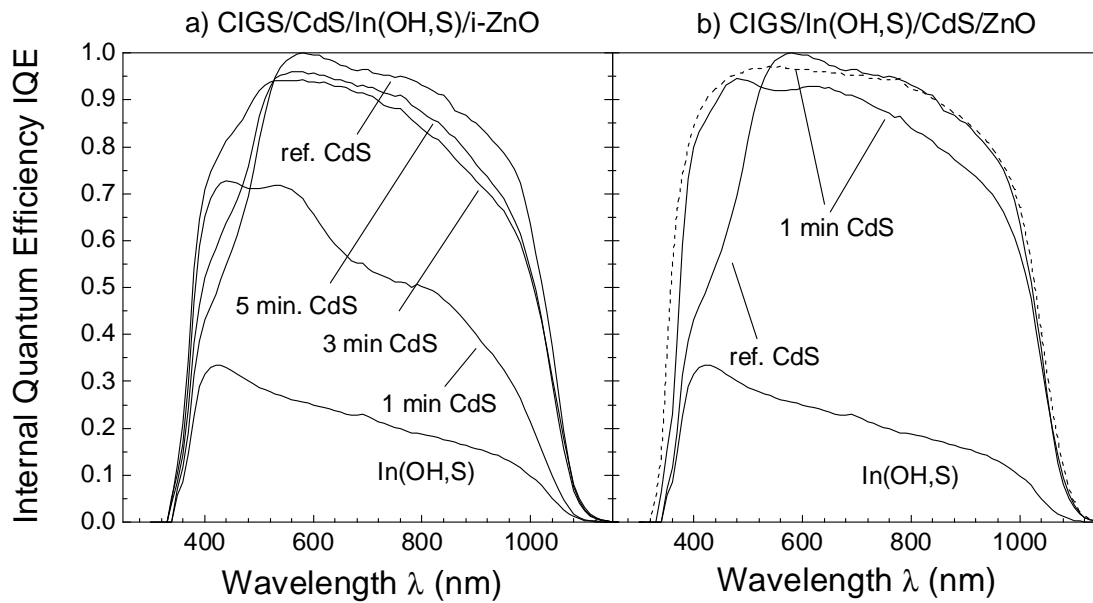


Figure 5.10: Internal quantum efficiency (*IQE*) curves of the devices with double buffers in comparison with the single reference CdS and In(OH,S) buffer devices: a) double buffer type A with different times of CdS deposition and b) double buffer type B with a CdS layer deposited in 1 min (≈ 5 nm), with i-ZnO (full line) and without i-ZnO (dashed line).

reduction of interface recombination leading to an increase of the *IQE* that is independent of wavelength, but also leads to an increase of the collection probability deeper in the absorber. As will be shown in section 5.4, the latter effect results from an increasing width of the space charge region (*SCR*) in the absorber.

With the thin CdS deposited in 1 min, the *IQE* curve of the *double buffer B* devices with such defective CIGS/In(OH,S) interface (Fig. 5.10b) is much higher with a small loss in the red light region compared to the CdS buffer device, which is compensated by a yield in the blue light region. A further improvement in *IQE* is obtained by omission of the i-ZnO layer (dashed line). It is worth to note that the double buffer B cells without i-ZnO has higher V_{OC} and *IQE* and the same *FF* as the CdS cell and hence yields additional 1% in efficiency.

5.3.3 Metastability behavior

5.3.3.1 Observation by current/voltage measurements

Figure 5.11 compares current/voltage (I/V) curves of illuminated samples with double buffers to those of devices with standard CdS and with single In(OH,S) buffer. All devices in Fig. 5.11 have a window layer that includes i-ZnO. The worst I/V curve in Fig. 5.11 having an abnormal S-shape, the so-called double diode behavior, is that of the In(OH,S) device. In addition, this curve displays a hysteresis of the I/V curves under illumination, i.e., the fill factor is even lower if measured from reverse to forward bias (V-/+ mode) compared to the opposite situation (V+/- mode). In the case of the *type A* double buffer device (with the In(OH,S)/ZnO interface), the deformation of the I/V curves and the hysteresis is reduced, but both features are still present. In contrast, in the *type B* double buffer device, the I/V hysteresis disappears completely, and this device even provides a better cell performance than the present standard CdS reference devices. Thus, the comparison of the I/V characteristics of the double buffer devices to the single buffer devices leads to the conclusion that both features, the I/V hysteresis as well as the overall poor *FF*, relate directly to the properties of the In(OH,S)/ZnO interface.

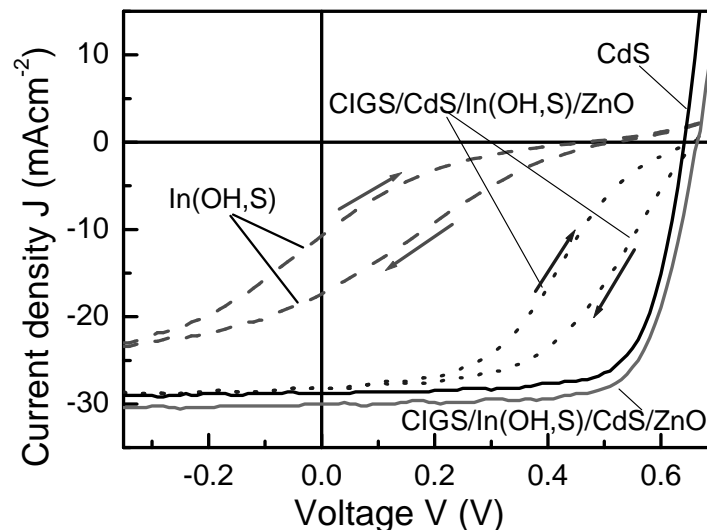


Figure 5.11: Current/voltage characteristics of samples in series I under illumination. The I/V hysteresis loops appear only in the samples with the In(OH,S)/i-ZnO interface. The arrows show the direction of applied voltage bias for measurement.

Effect of air annealing

Figure 5.12 illustrates the effects of air annealing at 200° C on the devices with the In(OH,S)/ZnO interface (*type A* double buffers as well as In(OH,S) devices). Figure 5.12a reveals that air annealing up to 40 min continuously increases the fill factor FF . Figure 5.12b takes the relative fill factor difference $\Delta ff = (FF^{+/-} - FF^{-/+})/FF^{+/-}$, i.e. the relative difference between the fill factors $FF^{+/-}$, $FF^{-/+}$ derived from the I/V curves measured either from forward or from reverse direction, to quantify the hysteresis. We can see from Fig. 5.12b that the hysteresis decreases considerably with increasing annealing time, making $\Delta ff \approx 10\%$ for the In(OH,S) device and almost zero for the *type A* double buffer device. Note that air annealing at 200 °C for a few minutes can *gradually* improve the performance of standard CdS buffer devices as well. However, air-annealing with annealing times up to several tens of minutes appears *mandatory* for devices with an In(OH,S)/ZnO interface. Nevertheless, the beneficial effect of air annealing on these devices is reversible, i.e. the performance re-degrades again after storing the sample in the dark for a few days.

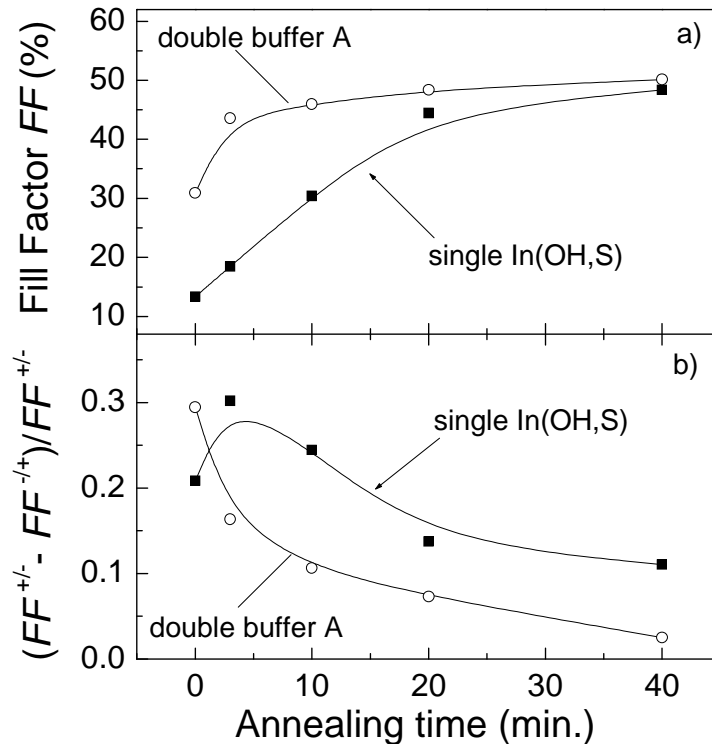


Figure 5.12: Effect of air annealing on the I/V characteristics of the samples with the In(OH,S)/i-ZnO interface: a) annealing increases FF and b) simultaneously decreases the hysteresis.

Effect of light soaking

Light soaking does not improve the performance of the devices with the CdS/ZnO interface (standard CdS and double buffer B devices), but it improves significantly the devices with the In(OH,S)/ZnO interface. Figure 5.13 shows the effects of light soaking under simulated solar spectrum AM 1.5 on the double buffer A device. After 75 min light soaking, FF increased strongly from 55% to 67%, whereas V_{OC} and J_{SC} remained almost unchanged (Fig. 5.13 a). Simultaneously, the I/V hysteresis disappeared.

Figure 5.13b shows the semi-logarithmic I/V characteristics of the device taken in the dark before and after 75 min light soaking. Before light soaking, the current in the forward direction is very low, indicating a high barrier at the In(OH,S)/ZnO interface, which hinders the electrons move from the ZnO emitter to the In(OH,S) buffer. Light soaking decreases this barrier and increases strongly the current.

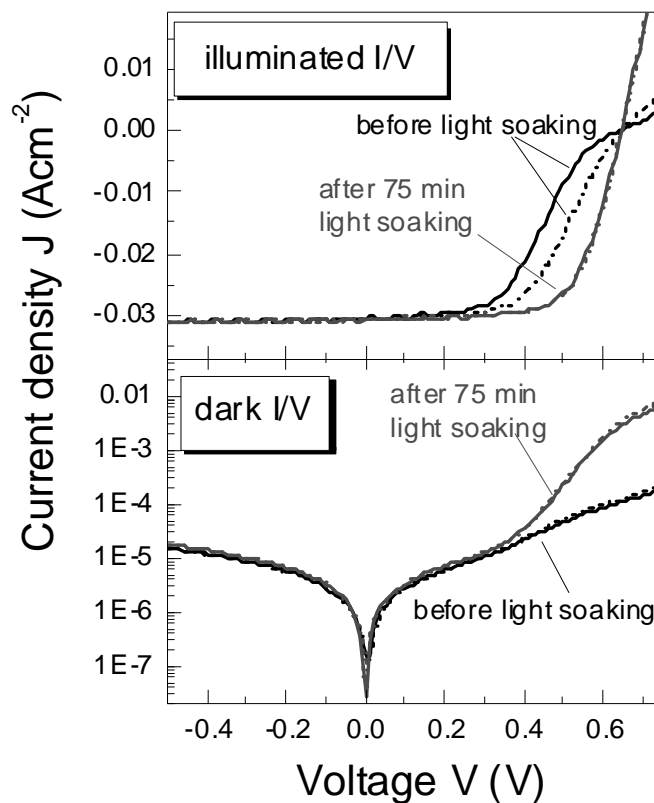


Figure 5.13: Effect of light soaking on the I/V characteristics of the double buffer A sample with the In(OH,S)/i-ZnO interface under illumination and in the dark: increase of FF and simultaneous decrease of the hysteresis.

5.3.3.2 Observation by capacitance/voltage measurements

Figure 5.14 shows the C/V characteristics at room temperature of the devices measured at 100 kHz. The junction capacitance of the In(OH,S) buffer device is much higher than that of the CdS device over the whole range of applied voltages. Moreover, as in the case of the I/V characteristics, the C/V characteristic of the In(OH,S) buffer device exhibits a hysteresis, i.e., the junction capacitance is lower when measured from negative bias to positive bias (V-/+ mode) compared to the opposite situation (V+/- mode). A high junction capacitance and the C/V hysteresis are observed also in the double buffer A device, whereas the double buffer B device has the same capacitance level of the CdS device. The comparison indicates that the C/V characteristics of the In(OH,S) buffer device are directly related to the properties of the In(OH,S)/ZnO interface.

Metastability upon voltage bias treatment has been well known in Metal-Oxide-Silicon (MOS) devices where a shift of capacitance/voltage profile is caused by mobile positive ions

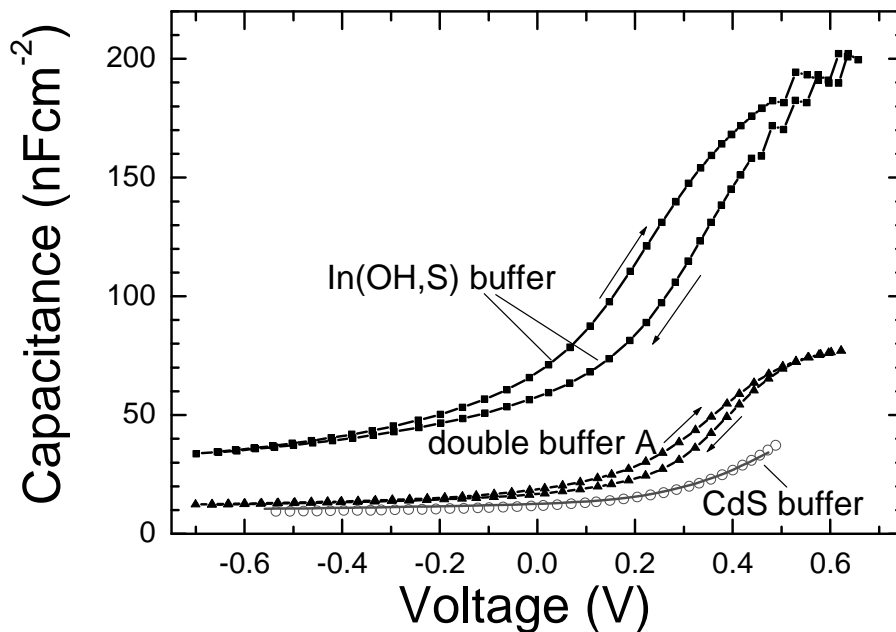


Figure 5.14: Capacitance/Voltage characteristics of the samples in series I in the dark at 100 kHz. The curve of the double buffer B device (open circles) coincides with that of the CdS device (full line). The C/V hysteresis loops appear only in the sample with the In(OH,S)/i-ZnO interface. The arrows show the direction of applied voltage bias for the measurements.

in the oxide layer [134]. I note that the metastability observed in the In(OH,S) device has a different origin. If under reverse bias a quantity Q_m of positive ions would move from the buffer/window interface to the buffer/CIGS interface, this would induce additional negative charges in the CIGS layer (Fig. 5.15). As a result, the space charge region in the CIGS absorber layer would be wider and the junction capacitance would be lower. The experimental observations for the In(OH,S) buffer device contradict this situation.

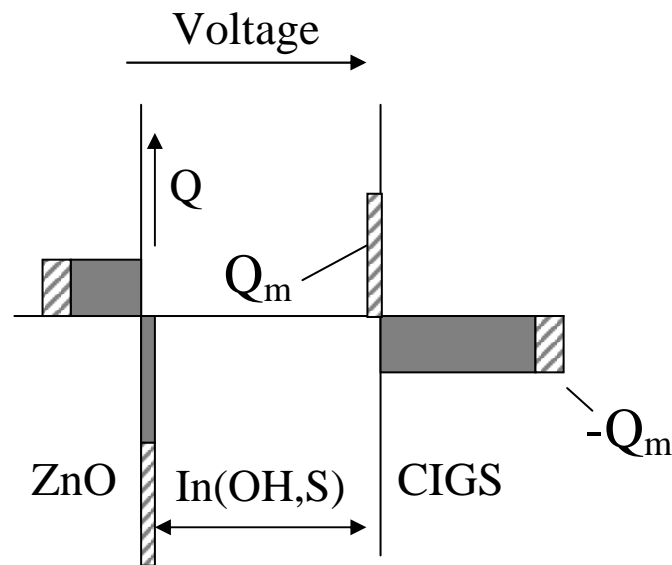


Figure 5.15: Schematic representation of the charge redistribution in the ZnO/In(OH,S)/CIGS heterojunction in the case when a quantity Q_m of mobile positive ions would move from the ZnO/In(OH,S) interface to the In(OH,S)/CIGS interface under a reverse voltage bias. An additional negative charge $-Q_m$ is induced in the bulk of the CIGS layer. The same effect occurs in the ZnO layer. This would result in a widening of the space charge region and a lowering of the junction capacitance.

5.3.3.3 Thermally stimulated capacitance measurements

In this section, I used thermally stimulated capacitance (TSC) measurements to investigate the nature of the electronic metastability that is caused by reverse voltage bias on devices with different buffer layers or different buffer layer combinations. Note here that different types of metastabilities are routinely observed in CIGS solar cells [135]. The so-called reverse bias type [135] is the one that most significantly affects the electronic behavior of devices with CBD-deposited non-CdS buffer layers. Therefore, avoiding this type of metastability is of primary importance for all alternative buffer devices. I note further that the reverse bias treatment (application of a reverse voltage $V_r = -1$ V for 1 h at 300 K) used to create a metastable state in the present TSC analysis is harder than the -0.5 V that is experienced by the sample for a few seconds when measuring the I/V curve in (-/+) direction as described in the previous subsection.

TSC of the CdS device

The upper part of Fig. 5.16a displays a typical TSC spectrum at 100 kHz of a standard CdS buffer device at equilibrium (full squares). The TSC spectrum has two transitions at 125 K and 275 K. These capacitance steps transform into two minima N1 and N2 in the differentiated capacitance curve $f \times dC/df$ in the lower part of Fig. 5.16a. The transition N1 is normally attributed to the charging and discharging of the donor states at [136] or close [137] to the CdS/CIGS interface and transition N2 belongs to a deep acceptor in the bulk of the CIGS layer. After applying reverse voltage bias for 1 h at 300 K, the junction capacitance (open squares) at low temperatures increases slightly. This increase is more significant at higher temperatures, where deep defects do contribute to the capacitance. Also seen in this curve is the onset of relaxation to the initial equilibrium state at temperatures $T > 270$ K. The lower part of Fig. 5.16a displays the differentiated $f \times dC/df$ spectra. Comparison of the equilibrium curve (full squares) with the metastable one (open squares) unveils the origin of the reverse bias metastability in standard CdS-buffer devices. The increase of the peak N2 indicates the metastable creation of deep defects in the CIGS absorber by the reverse bias treatment. Thus, the effect of reverse bias on devices with CdS buffer layers seems to be an absorber rather than an interface effect [138, 139].

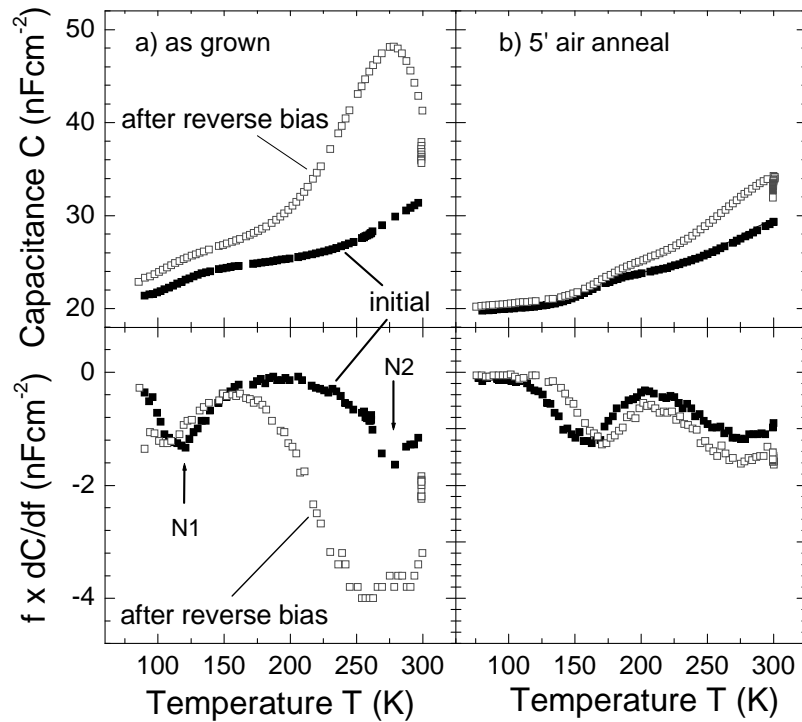


Figure 5.16: Thermally stimulated capacitance TSC (upper part) and its frequency differential $f \times dC/df$ (lower part) spectra of the CdS buffer device in the equilibrium state (closed squares) and after applying reverse voltage bias in the dark for 1 hour (open squares): a) as grown and b) after 5 minutes of air annealing at 200 °C.

The behavior of the samples changes significantly after an air-anneal at 200 °C for 5 min. As shown by Fig. 5.16b, air annealing leads only to gradual changes of the direct and of the differential TSC spectrum, as far as the equilibrium state is concerned. The overall capacitance decreases slightly and the peak N1 shifts to higher temperature due to a passivation of Se vacancies at the CdS/CIGS interface [140]. The TSC spectrum of the air-annealed device after reverse bias looks almost unchanged compared to the equilibrium one. Thus, air annealing stabilizes CIGS solar cells against the reverse bias metastability. Note that in a photovoltaic module reverse bias may easily occur to single cells, e.g. by shadowing. The slightest degradation of a single cell, even if reversible, has a deleterious effect on the overall module performance. Therefore, the finding that air annealing greatly reduces the reverse bias metastability is of great practical importance.

TSC of the In(OH,S) device

The initial state of In(OH,S) buffer device (closed squares in Fig. 5.17a) has a much higher capacitance over the entire temperature range compared to the capacitance of the CdS device. The two familiar transitions N1 and N2 are observed at the same temperatures, i.e. as peaks in the $f \times dC/df$ spectrum. Like in the case of the CdS device, we obtain after the reverse voltage treatment an increase of the junction capacitance in the entire temperature range. However, the change of the TSC spectra of the In(OH,S) buffer devices has another fingerprint than that of the CdS device. A large capacitance step appears already at low temperatures and, accordingly, we observe a huge increase of the peak N1 for the In(OH,S) buffer sample after reverse bias. Here, air annealing at 200 °C for 10 min reduces considerably the effect of the reverse voltage bias, though the metastable change of the N1 transition remains the dominant feature of the reverse bias metastability.

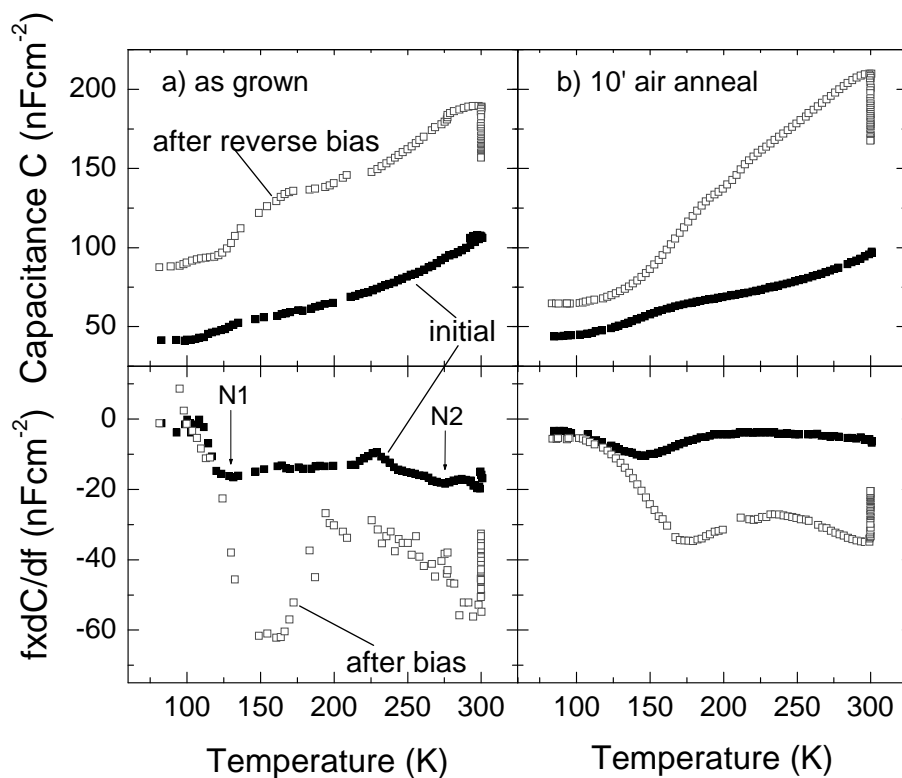


Figure 5.17: TSC (upper part) and $f \times dC/df$ (lower part) spectra of the In(OH,S) buffer device in the equilibrium state (closed squares) and after applying reverse voltage bias in the dark for 1 hour (open squares): a) as grown, b) after 10 minutes of air annealing at 200°C.

Comparison of the consequences of reverse biasing on In(OH,S) buffer devices (Fig. 5.16) with those on CdS buffer devices (Fig. 5.16) suggests a quantitative and qualitative difference. Whereas the reverse bias metastability in CdS buffer devices appears primarily as an effect in the absorber (increase of transition N2), in In(OH,S) buffer device the metastability seems to be dominated by an interfacial effect resulting in an increase of N1. Thus, the so-called reverse bias metastability is not a single effect. Instead, reverse bias voltage has different physical consequences that depend on the buffer material used for the device.

TSC of the double buffers device

Figure 5.18 compares the TSC spectra and the reverse bias effect of the two different double buffer devices. Interestingly, the *type A* device (CIGS/CdS/In(OH,S)/ZnO) clearly exhibits an increase of N1 upon reverse biasing whereas we do not observe a change for the N2 transition. In contrast, the metastable behavior of the *type B* device (CIGS/ In(OH,S)/CdS/ZnO) mainly concerns the higher temperature range much as observed for the CdS buffer device. This result demonstrates that the In(OH,S)/i-ZnO interface causes the dramatic metastable enhancement of the transition N1, whereas exclusion of the In(OH,S)/i-ZnO interface in the *type B* device reduces the junction capacitance and the metastable behavior approximately to the level of the CdS device.

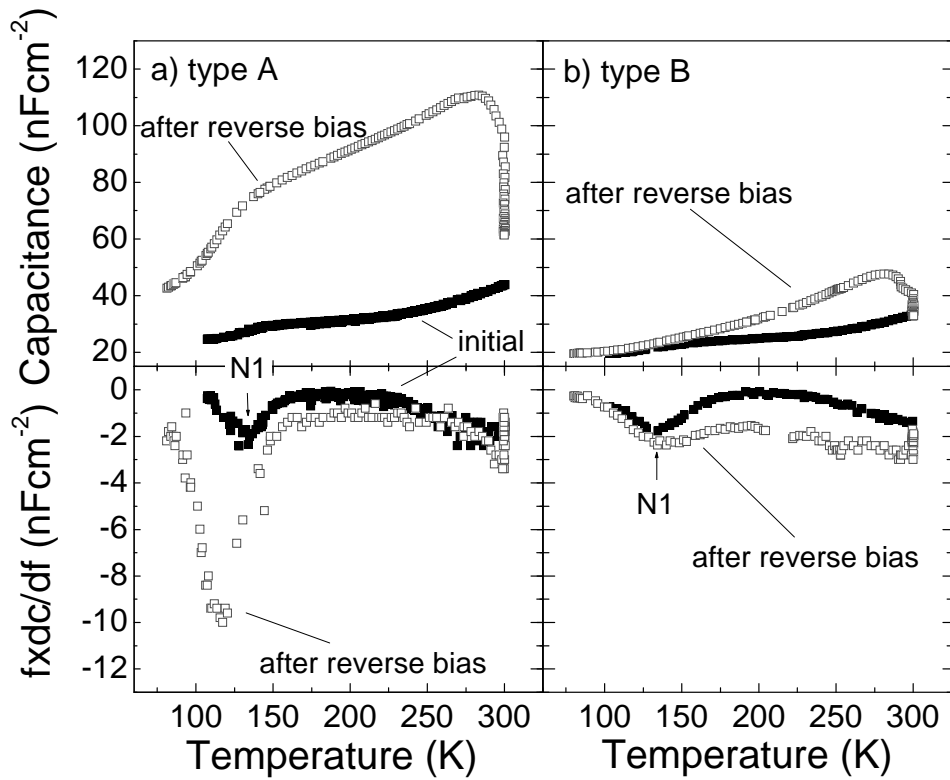


Figure 5.18: TSC (upper part) and $f \times dC/df$ (lower part) spectra of the double buffer A (left hand side) and double buffer B (right hand side) devices in the equilibrium state (closed squares) and after applying reverse voltage bias in the dark for 1 hour (open squares).

5.4 Modifications of the ZnO/In(OH,S) interface

All the electrical analysis in the previous sections pointed to the same fact that properties of the ZnO/In(OH,S) interface cause the poor performance and metastabilities in the In(OH,S) buffer device. It has also been shown that the insertion of the thin CdS layer in the double buffer type B removed bad characteristics of that device. There are two possibilities of the effect of the CdS insertion:

- i) The CdS layer protects the In(OH,S) surface from the damage of the ZnO sputtering process or prevents an intermixing at the ZnO/In(OH,S) interface which could cause unfavorable properties;
- ii) Not the CdS layer by itself but the chemical bath for the CdS deposition modified the properties the In(OH,S) surface in the favorable way.

In order to test the first case, I used an In₂O₃-window instead of the standard ZnO layers to complete the solar cell with the In(OH,S) buffer. The performance of this device was not improved, and hence the intermixing is not a cause for the unfavorable interface properties.

To test the second case, the CIGS with the overlayer In(OH,S) were treated prior the ZnO sputtering process in different solutions containing NH₃ (with and without thiourea) or Cd²⁺ cations. Only the latter improved the solar cell characteristics, which will be illustrated in this section.

Treatment in a solution containing Cd²⁺

After the deposition of the In(OH,S) buffer layer onto the CIGS substrate, I treated the sample with a solution containing cadmium acetate and ammonia at 60 °C for 5 min. The concentrations of the reagents were chosen to be the same as in the solution for the CdS deposition. The surface of the treated and untreated sample underwent an analysis by XPS measurement. The treated sample was then completed with the ZnO window layers, and its solar cell performance was compared to that of the standard CdS and untreated In(OH,S) buffer device.

Figure 5.19 show an amazing feature of the treatment. By treatment for 5 min, the I/V characteristic of the In(OH,S) buffer device is strongly improved (curve 3) and does not exhibit a hysteresis. The performance of the treated solar cell is even better than the annealed and light soaked In(OH,S) buffer device (curve 2) and exhibits long term stability. I did not observe a degradation of the cell even after six months. The treated cell had still a lower FF

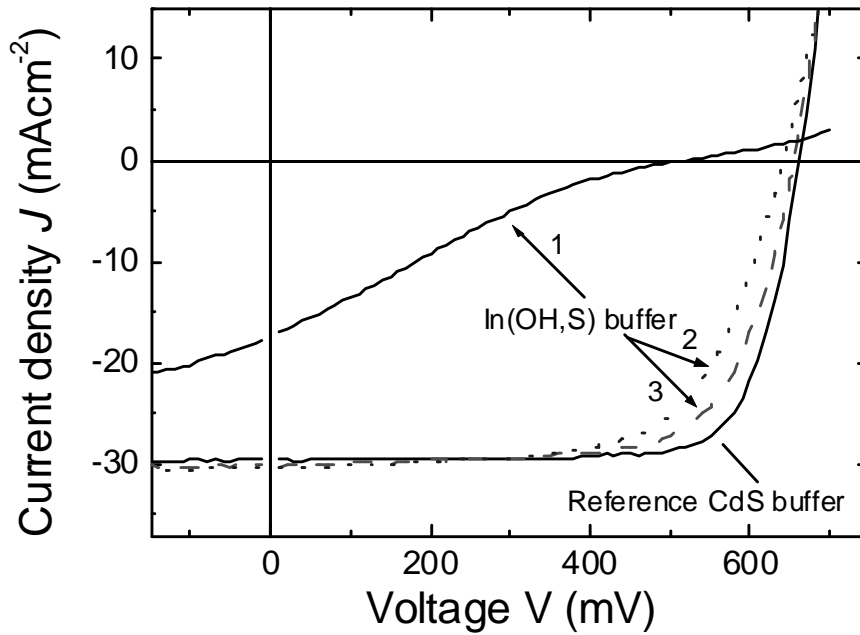


Figure 5.19: The I/V characteristics of the In(OH,S) buffer devices under illumination in comparison to the reference CdS buffer device: 1) as prepared, 2) after 40 min air annealing and 30 min light soaking, 3) treated in the solution containing Cd^{2+} and without annealing and light soaking.

compared to the CdS device. However, I believe that with an optimization of the treatment parameters (concentration, time, temperature), the In(OH,S) buffer device should lead to a stable efficiency comparable to the CdS device.

The results of the XPS measurement (Fig.5.20) reveals that after the treatment, a small amount of Cd is adsorbed on the surface of the In(OH,S) buffer. The Auger parameter of the absorbed Cd is 786.75, suggesting the formation of CdS. The peak intensities of In and S are slightly decreased whereas the signal of oxygen is increased. The Auger parameter of the In is slightly decreased from 406.55 to 406.35 eV, i.e. it shifts closer to the Auger parameter of $\text{In}(\text{OH})_3$.

Based on the results of the XPS analysis, I suppose that the Cd^{2+} ions from the treatment solution reacts with the S on the In(OH,S) surface, and simultaneously hydroxide adsorbs onto the In site



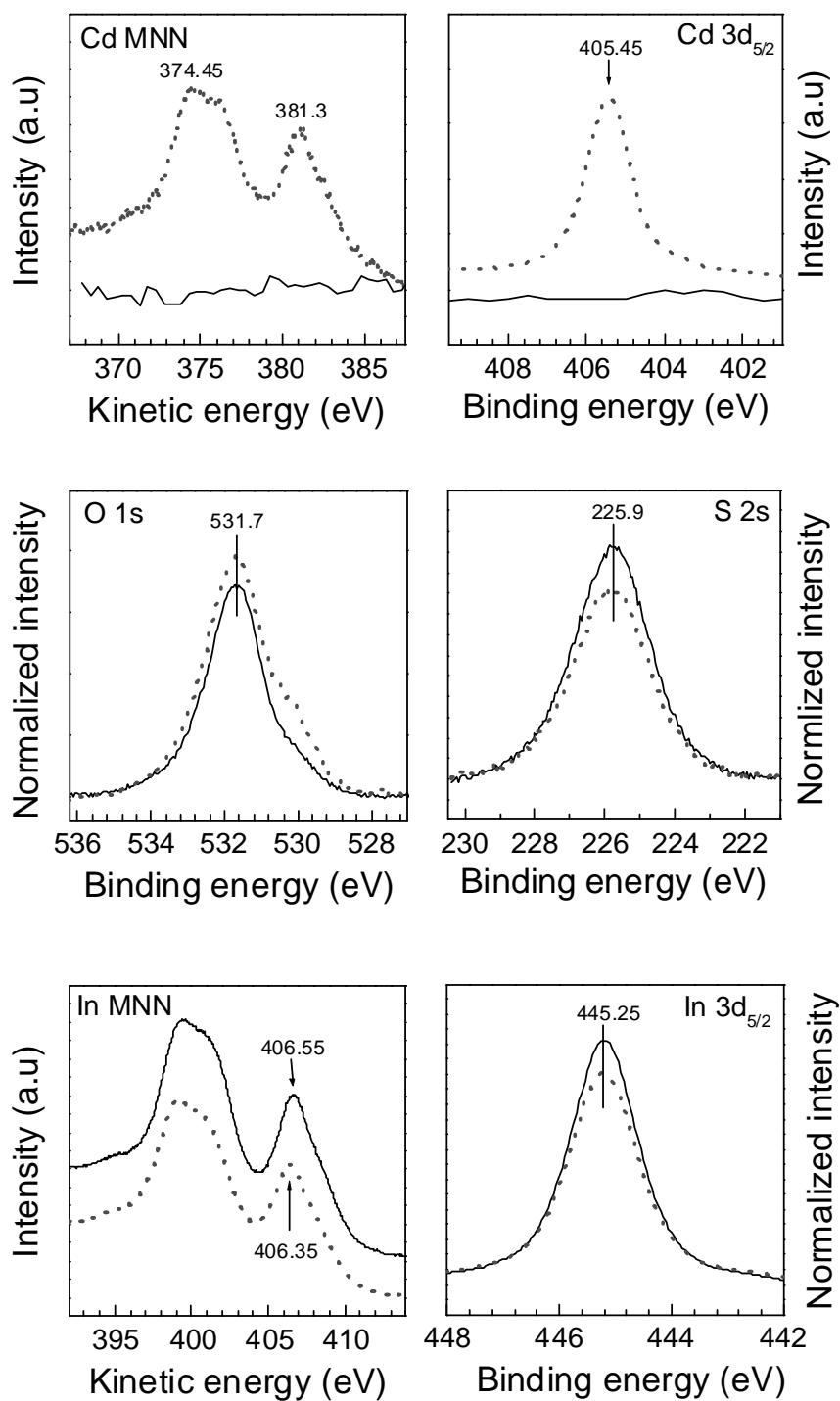


Figure 5.20: The evolution of x-ray photoelectron and Auger spectra of elements on the $\text{In}(\text{OH},\text{S})$ buffer surface before (full lines) and after (dotted lines) 5 min treatment in the ammonia solution containing 1.4 mM $\text{Cd}(\text{CH}_3\text{COO})_2$.

Treatment in Zn-solutions

The experiment with Cd-treatment indicated that the metal ions in the solution can somehow repair electronic defects at the In(OH,S) buffer surface. Hence, we can try with a solution of another metal salt to obtain a Cd-free solar cell. Therefore, I treated the In(OH,S) buffer layers, deposited onto the CIGS absorber, in 1M ammonia solutions with different concentrations of $ZnCl_2$ for 5 min at $60^\circ C$.

In the case of using 1.4 mM $ZnCl_2$ (the same concentration as for the Cd-treatment), the efficiency of the In(OH,S) buffer device improves slightly ($\sim 4\%$ compared to $\sim 1\%$ of the untreated device). The use of $ZnCl_2$ solution with higher concentration (14 mM) increases strongly all the parameters V_{oc} , J_{sc} and FF of the device (Fig. 5.21). The cell has even higher values V_{oc} and J_{sc} than the reference CdS device. However, the FF of the treated In(OH,S) cell is still lower than in the case of the standard cell. Nevertheless, the treatment provides the In(OH,S) buffer cell with an efficiency as high as the CdS buffer device.

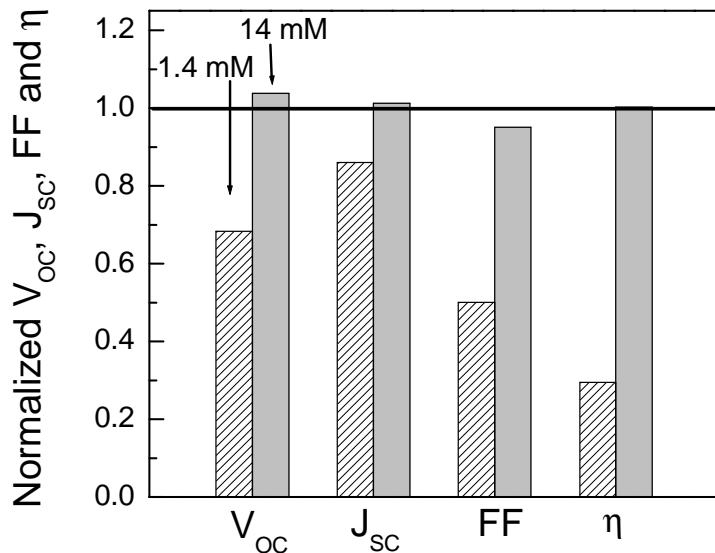


Figure 5.21: Relative deviation of V_{oc} , J_{sc} , FF and η of the In(OH,S) buffer device treated for 5 min in the ammonia solutions with 1.4 mM and 14 mM $ZnCl_2$. All the parameters are normalized to those of the reference standard CdS buffer device, which has the $Cu(In,Ga)Se_2$ absorber layer prepared in the same run and an efficiency of 13%.

5.5 Discussion

All experimental results show that the In(OH,S)/i-ZnO interface plays a predominant role for the poor electronic properties and the huge electronic metastability in the alternative In(OH,S) buffer device. The following will specify this conclusion in terms of an electronic model and numerical simulations using the program SCAPS-1D [141]. In section 5.5.1, I define a model for the buffer/CIGS interface. Then, the influence of the defects at the buffer/window interface on the electronic properties and the I/V curves of the devices is demonstrated in section 5.5.2. Finally, I propose explanations for the electrical metastabilities observed in the experiments.

5.5.1 Electronic model

5.5.1.1 Band diagram approach

Buffer/window interface

Figure 5.22 shows the basic band diagram of the ZnO/buffer/CIGS heterojunction in equilibrium. In the ideal case without interface states, positive charges in the window/buffer part of the junction are balanced by negative charges in the SCR of width w_a in the CIGS absorber:

$$Q_n + qd_w N_w + qd_b N_b = qN_a w_a \quad (5.6)$$

Here Q_n are the charges per unit area in a depletion layer of the high-doped Al:ZnO window layer, q is the elementary charge; N_w , N_b and N_a are the doping concentrations in the i-ZnO, the buffer and CIGS layers with the thickness d_w , and d_b , respectively; w_a is the width of the SCR in the CIGS layer.

From this equation, it can easily be seen that an introduction of negatively charged states at the interfaces (a negative quantity of charges is added to the left side of the Eqn. 5.6) reduces the width w_a of the space charge region in the absorber layer. From the capacitance measurements, we have seen that the devices with the In(OH,S)/ZnO interface have a

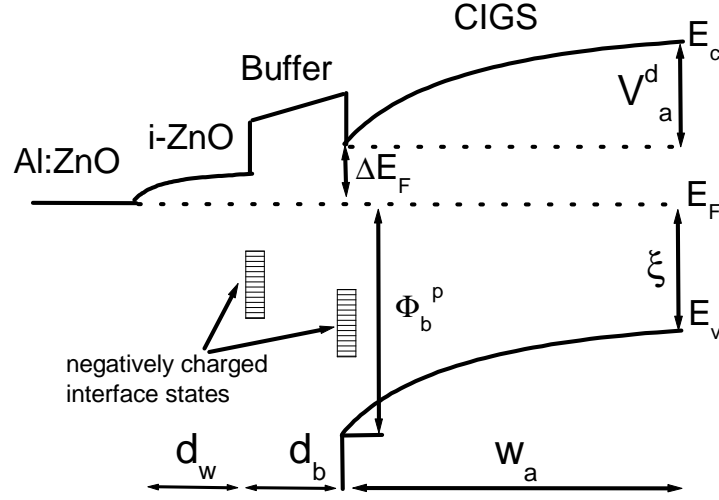


Figure 5.22: Basic band diagram of the ZnO /buffer/CIGS heterojunction

narrower SCR. Therefore, this interface has to contain a large number of negatively charged defects.

From the depletion approximation, the relation between w_a and the Fermi level ΔE_F at the buffer/CIGS interface is given by

$$V_D^a = qN_a w_a^2 / 2\epsilon_a \quad (5.7)$$

and

$$\Delta E_F + \xi + V_D^a = E_g \quad (5.8)$$

where V_D^a is a drop of the built-in potential in the absorber layer, ξ is the Fermi level in the neutral part in CIGS and ϵ_a is the relative dielectric permittivity of the absorber.

Thus, a reduction of w_a by adding negative charges in the buffer goes hand in hand with a reduction of the band bending V_D^a and an increase of ΔE_F . Simultaneously, the barrier for holes at the interface Φ_b^p , defined by $\Phi_b^p = E_g - \Delta E_F$, decreases. This leads to a higher recombination velocity at the buffer/CIGS interface.

Buffer/CIGS interface

The observed high V_{OC} and dominant bulk recombination in the double buffer B devices suggest a minor role of the recombination at the In(OH,S)/CIGS interface in the electronic loss processes. This result implies further that not the presence of Cd at the interface as suggested by other authors [79-81], but properties of the CIGS surface itself play the essential role for the heterojunction formation.

Se vacancies V_{Se} at the CIGS surface [142] can cause a large band bending. By an analytical calculation [140] and a simulation [63], the authors show that densities of interface states in order of $10^{13} \text{ cm}^{-2} \text{ eV}^{-1}$ are sufficient to pin the Fermi level E_F at the CdS/CIGS interface at the neutrality level. Furthermore, Fermi level pinning at close to the CIGS conduction band is also proposed [135] to argue a capacitance transition of the interface states derived from the admittance spectroscopy. However, if the V_{Se} plays such an important role for heterojunction formation, air annealing with the well-known effect of a passivation of V_{Se} by oxygen [142] would strongly influence the cell performance. This contradicts the experimental result, where I did not find a significant change upon air annealing in solar cell parameters (except for the shift of the N1 peak) for the CdS buffer device. Moreover, the increase of IQE curves with increasing CdS buffer thickness in the double buffer A devices suggests that the density of V_{Se} is actually not sufficiently high to predominantly control the SCR in the absorber layer and the position of the Fermi level at the interface.

To explain the effects observed in the experiment with double buffers, I propose that the high barrier for holes at the interface, which hinders the surface recombination, originates from a lowering of the valence band energy in a thin layer on the top of the CIGS absorber. In the following, numerical simulations by using the SCAPS-1D program demonstrate the results in our experiment for four types of devices. I assume that the CIGS absorber naturally involves a 20 nm weak n-type surface defect layer (SDL) with a bandgap of 1.35 eV, i.e. the valence band is 0.2 eV lower than in the bulk.

Input parameters for the simulation

Table I lists the main parameters of the semiconductor layers in the simulation. The parameters of the interface states are listed in Table II. More details are given in the Appendix A at the end of the thesis.

Table I. Parameters of semiconductor layers used in the simulation. The quantities N_C and N_V denote the conduction and valence band effective density of states, $v_{th,n}$, $v_{th,p}$ and μ_n , μ_p are the thermal velocities and mobilities for electrons and holes, ϵ is the relative dielectric permittivity.

	CIGS	SDL	CdS	In(OH,S)	i-ZnO	ZnO:Al
Thickness (μm)	1.980	0.02	0.05	0.015	0.05	0.3
Band gap (eV)	1.15	1.35	2.4	3.0	3.3	3.3
Electron affinity (eV)	4.5	4.5	4.5	4.5	4.55	4.55
N_C (cm^{-3})	6.7×10^{17}	6.7×10^{17}	2×10^{19}	2×10^{19}	5×10^{18}	5×10^{18}
N_V (cm^{-3})	1.5×10^{19}	1.5×10^{19}	2×10^{19}	2×10^{19}	5×10^{18}	5×10^{18}
$v_{th,n}$ (cm/s)	3.9×10^7	3.9×10^7	1×10^7	1×10^7	1×10^8	1×10^8
$v_{th,p}$ (cm/s)	1.4×10^7	1.4×10^7	1×10^7	1×10^7	1×10^8	1×10^8
μ_n (cm^2/Vs)	50	50	50	50	50	50
μ_p (cm^2/Vs)	20	2	20	20	20	20
Doping (cm^{-3})	5×10^{15} (p)	1×10^{13} (p)	5×10^{16} (n)	5×10^{14} (n)	1×10^{16} (n)	1×10^{18} (n)
ϵ	10	10	10	10	10	10

Table II. Defect densities at the interfaces of the CdS and In(OH,S) buffers to the CIGS and ZnO layers. The type of defects is denoted (d) for positively charged donors and (a) for negatively charged acceptors. The quantities marked with an asterisk are the energy levels of the defects counted from the maximum of the valence band edge.

Density of defects		CdS	In(OH,S)
at CIGS/buffer interface N_{ba} (cm^{-2})	(1.25 V)*	2×10^{10} (d)	2×10^{10} (d)
	(0.65 V)*	1×10^{10} (a)	1×10^{11} (a)
at ZnO/buffer interface N_{wb} (cm^{-2})	(1.2 V)*	7×10^9 (a)	7×10^{11} (a)

5.5.1.2 Results of simulations

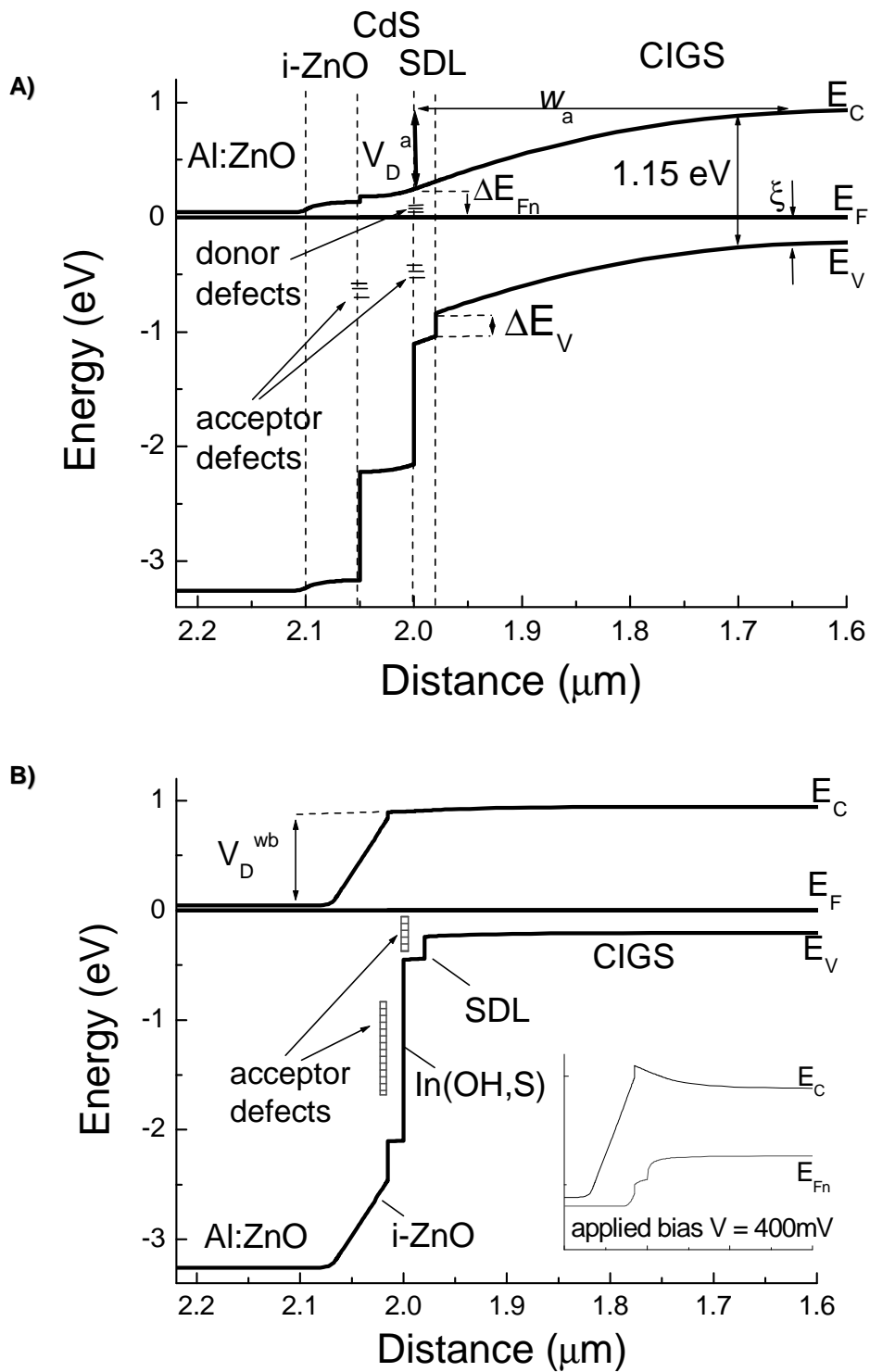


Figure 5.23: Simulated by SCAPS-1D band diagrams: a) of the CdS buffer device with low densities of acceptor defects at the interfaces and b) of the In(OH,S) buffer device with high densities of those.

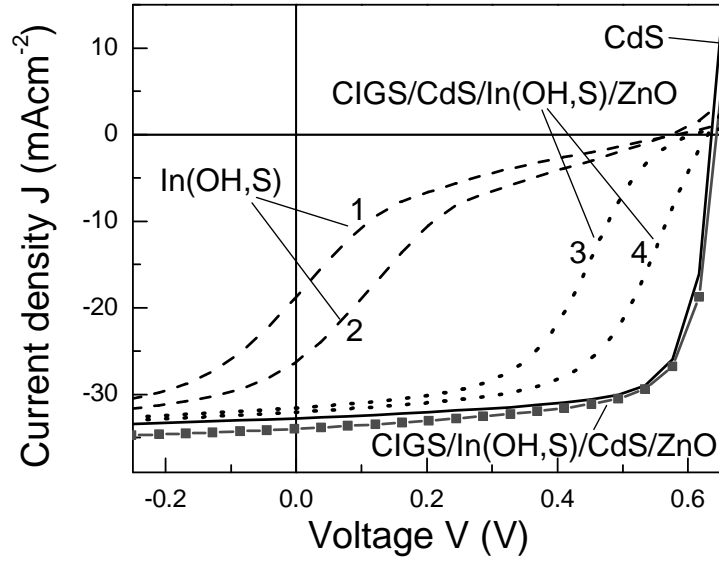


Figure 5.24: Simulated I/V curves of the devices with different buffer layers: CdS (solid line), In(OH,S) (dashed lines), double buffer A (dotted lines) and double buffer B (closed squares). The densities of the donor interface states at the buffer/CIGS interface are assumed to be low for all types of buffer: $2 \times 10^{10} \text{ cm}^{-2}$ (donor, $S_p = 10^4 \text{ cm/s}$). The CdS buffer also has low acceptor defect densities at both interfaces: $1 \times 10^{10} \text{ cm}^{-2}$ ($S_p = 10^5 \text{ cm/s}$) at the CdS/CIGS interface and $7 \times 10^9 \text{ cm}^{-2}$ at the CdS/i-ZnO interface, whereas in the case of the In(OH,S) buffer they are much higher: 1×10^{11} ($S_p = 10^6 \text{ cm/s}$) at the In(OH,S)/CIGS interface and $7 \times 10^{11} \text{ cm}^{-2}$ (curves 2 and 4) and $8 \times 10^{11} \text{ cm}^{-2}$ (curves 1 and 3) at the interface to the ZnO window.

Figure 5.23 displays the simulated band diagrams of the CdS buffer (a) and In(OH,S) buffer devices (b). The CdS buffer device is characterized by a wide SCR in the absorber layer and a large band bending V_D^a . This simulated device provides an efficiency $\eta = 15.44\%$ with $V_{OC} = 641.9 \text{ mV}$ and $FF = 73.6\%$, i.e. very close to the experimental data, even with a surface recombination rate of 10^5 cm/s .

Figure 5.23b displays the simulated band diagram for the In(OH,S) buffer device, where we have a higher density of acceptor charges at both interfaces ($N_{ba}^a = 1 \times 10^{11} \text{ cm}^{-2}$, $N_{wb}^a = 7 \times 10^{11} \text{ cm}^{-2}$). The increase of the densities of the negatively charged defects at both interfaces

results in a decrease of the width of the SCR in the CIGS absorber w_a , and hence the collection of the photogenerated electrons is reduced.

The drop of the built-in potential in the absorber region V_D^a is related to w_a and ΔE_F as described in Eq. 5.7 and Eq. 5.8. Therefore, the decrease of w_a leads to a decrease of V_D^a and simultaneously to an increase of ΔE_F . Consequently, the barrier for holes is reduced and opens a path for surface recombination through the interface states, which are many more in this case. Thus, V_{OC} is much lower in the In(OH,S) buffer device.

Moreover, with a high density of negatively charged defects at the buffer/window interface N_{wb}^a the electrical field splits in two parts: V_D^b drops steeply across the i-ZnO layer and less in the absorber and buffer layers. When the voltage is applied, the built-in potential between the contacts is lower in a specific manner: V_D^b is almost unaffected, while V_D^a flattens. As the applied voltage increases further, the lower of the built-in potential appears in an opposite band bending of V_D^a , which hinders the movement of the photogenerated electrons to the emitter (see the inset in Fig. 5.23b). Thus, the FF also decreases.

Double buffer A device: a high density of the negatively charged defects at the In(OH,S)/i-ZnO interface causes a barrier for electrons and results in a low FF. The Fermi level at the buffer/CIGS interface is also affected. Nevertheless, the surface recombination does not contribute a significant loss to V_{OC} due to the low density of states at the CdS/CIGS interface and the lowering of the valence band in the SDL.

Double buffer B device: the density of acceptor states at the buffer/CIGS interface and the recombination rate are one order of magnitude higher than in the case of the CdS device. Nevertheless, the valence band barrier of the SDL reduces the contribution of these defects to losses in V_{OC} .

Note that in both cases of double buffer devices, the recombination rate at the interface is higher than in the case of the CdS device, due to the shift of the Fermi level at this interface. Nevertheless, it plays still a minor role, due to the enlarged valence band of the SDL and the bulk recombination becomes dominant. On the other hand, the width of the SCR in the absorber layer is reduced as analyzed before. Thus, the double buffer devices yield a higher V_{OC} than the CdS device. With the increase of the CdS buffer thickness, w_a widens. Since the bulk recombination is still dominant, V_{OC} decreases as observed in the double buffer A devices. In both cases, w_a is narrower than in the CdS device, and hence the collection of photogenerated electrons in the absorber is reduced. Then, a direct contact with high-doped

ZnO, i.e. omission of the low doped i-ZnO, shifts the Fermi level again up to the conduction band and restores the QE.

It is worth noticing that the simulation based on our model shows quite different positions of the Fermi level at the buffer/CIGS interface in four types of devices, whereas the N1 peak in our experiments remains at the same temperature. Thus, the transition N1 is connected to the charge and discharge of discrete donor states on the CIGS surface, but does not indicate the Fermi level at the interface. Since the latter controls the surface recombination, a definition of its position in the complete device becomes a challenge for device characterization.

5.5.2 Metastabilities

From the experimental results and the simulation we can see that the defects at the buffer/window interface creates the barrier and controls the FF of the solar cells. Then, the fact that the I/V hysteresis loop is obtained only in the devices with an In(OH,S)/ZnO interface indicates that the reverse voltage bias induces additional negatively charged defects at this interface. Figure 5.24 shows the simulated I/V curves for four devices with 50 nm CdS buffer, 15 nm In(OH,S) buffer, and double buffers based on their combination. We obtain the I/V hysteresis loops for the devices having the In(OH,S)/i-ZnO interface by increasing the defect density of $1 \times 10^{11} \text{ cm}^{-2}$ at that interface. The results fit qualitatively well to the experimental results described in Fig. 5.11 and discussed above.

As analyzed before in Section 5.3.3.2, the metastability upon reverse voltage observed in our experiment is not caused by mobile ions as in the MOS devices. The increase of the negatively charged defects upon reverse voltage bias in the devices with the In(OH,S)/ZnO interface can be explained as follows: at the equilibrium state, the number of the charged acceptor defects is defined by a thermal equilibrium between the total density of acceptor defects and the hole concentration at the interface (Fig. 25a). As the reverse bias is applied, holes move to the absorber base, and some of them cannot immediately return to the buffer/window interface after switching off the voltage. Consequently, the hole concentration at that interface is reduced and hence, the thermal equilibrium between holes and acceptor defects is shifted. Now, there are not enough holes at the interface to discharge the negative defects as under equilibrium. Thus, we get more negatively charged defects at this interface. Consequently, the barrier for electrons at this interface is higher. When the *ac* voltage is

applied, the possibility of electrons in the conduction band to overcome this barrier is lower, i.e. the possibility of that they are trapped in the donor defects at the buffer/window interface increases. This explains why after reverse bias the N1 peak is increased, although the defect density at this interface remains the same as before applying the bias.

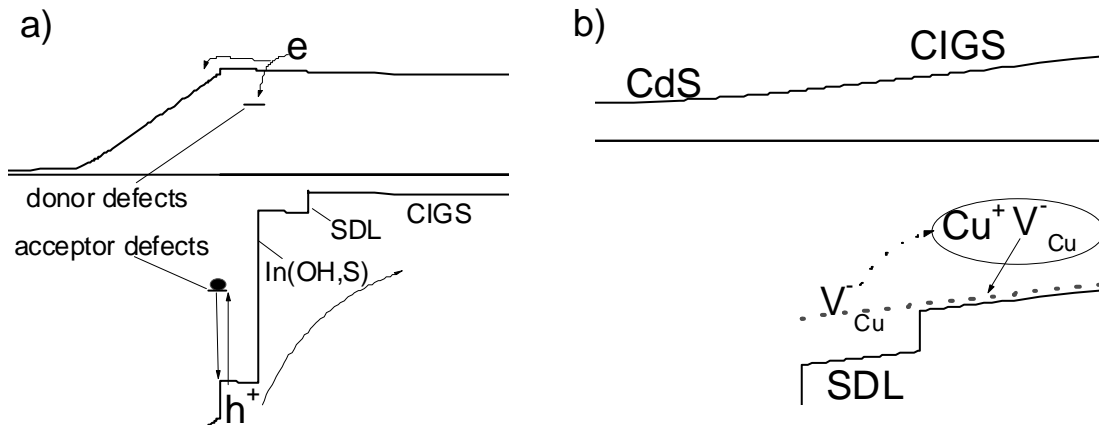


Figure 5.25: Models of the effects of a reverse voltage bias applied to: a) *In(OH,S)* buffer device and b) *CdS* buffer device.

The situation is different if the defect density at the buffer/window interface is low. In this case, the built-in potential drops mostly in the absorber region. Thus, the reverse bias affects only the absorber layer. A possible explanation for the metastability in this case could be a migration of Cu into the CIGS layer, as Cu is known to be mobile in Cu(In,Ga)Se_2 [143]. Under the effect of reverse voltage bias, Cu atoms from the surface region move deeper into the CIGS absorber layer and leave behind in the surface layer a large number of V_{Cu} (Fig. 5.25b). The latter is known as a shallow acceptor defect with an energy of 30 meV above the valence band. However, taking the V_{Cu} level as reference and stick to our assumption of the lowering of the valence band in the SDL, we could think that the metastable deep defects observed at 250 K in the TSC spectra in Fig. 5.16 are just the V_{Cu} located in the SDL. Since the diffusion of Cu is enhanced by a field of the positively charged V_{Se} , a passivation of the latter by air annealing reduces the metastability upon voltage bias in the device.

In conclusion, the reverse voltage induces a number of acceptor defects in the device junction. The location of the induced defects depends on whether the field mainly distributes

in the junction, that is in the CIGS absorber surface region in the case with the CdS buffer or at the In(OH,S)/ZnO interface in the case with the In(OH,S) buffer.

5.5.3 Chemical origin of the defects at the ZnO/In(OH,S) interface

The experiments with the modifications of the ZnO/In(OH,S) interface indicate that the defects at this interface belong to properties of the In(OH,S) surface. However, the question about the chemical origin of these defects remains open. In the investigations for Zn(OH,S) buffers, hydroxides involved in these buffers are attributed to a control factor that limits the cell performance. Reversible effects of soaking under UV-light in these buffer devices are explained by a reversible dehydration of Zn(OH)₂ in the Zn(OH,S) buffer by the photochemical reaction [44]:



In the case of the In(OH,S) buffer, XPS investigations of its surface before and after air annealing at 200 °C do not observe any significant change either in photoelectron or Auger spectra of the elements on this buffer surface that could be related to the desorption of water from In(OH,S). Furthermore, the Cd-treatment, inducing more hydroxide onto the In(OH,S) buffer surface, improves strongly the cell performance. Thus, hydroxide on the surface of the In(OH,S) buffer is not a defect. On other hand, I do not observe so critical metastability behavior in the device with a pure In₂S₃ buffer deposited by the PVD method. Therefore, the defects should arise rather from intermixing of In(OH)₃ and In₂S₃ than from any bonds in those compounds alone.

It is worth to note that hydroxide is also observed by the deposition at low pH value [55], where its precipitation is thermodynamically unfavorable. Therefore, hydroxide could be involved in the In-buffer by a reaction between the In[OH]³⁻ⁿ complexes and S²⁻ ions, e.g.:



In this case, In(OH)S is not a mixture of In(OH)₃ and In₂S₃, but it is a new chemical compound. By the XPS investigation of the Auger peak of In (MNN), Hariskos et. al. [54] proposed also the presence of such new compound In-OH-S. However, the question if this new compound causes the charged defects remains an open question.

5.5.4 Role of the chemical bath

CdS and In(OH,S) buffers are deposited from the chemical bath solutions with rather different conditions: the first at high pH value with adding of the complex agent NH_3 , whereas the latter was done at low pH value. Therefore, they have quite different properties in the bulk and at the interfaces. In the CdS buffer solar cell, Cd diffuses into the CIGS layer during CdS deposition. However, the diffusion of Cd should obey the charge balance condition in both the chemical solution and in the CIGS layer. Cd-diffusion into the CIGS layer goes hand in hand with the adsorption of hydroxide onto the CIGS surface as shown in chapter 4 or with an out-diffusion of Cu from the CIGS layer as reported in Ref. [79,80], where the Cd-treatment is done at a higher temperature and a higher $[\text{NH}_3]$ concentration. In other words, the CIGS layer should not yield any charge excess to invert the doped type of the surface layer as currently proposed [80,81,83]. Therefore, Cd at the buffer/CIGS interface does not enhance the cell performance. In the opposite, we find that Cd-diffusion results in the degradation of the cell efficiency.

Role of the chemical bath in the formation of the buffer/CIGS interface is minor due to a presence of the inverted CIGS surface layer. Thus, CBD deposition of buffer has an advantage over the other method due to its “soft deposition” ability, i.e. it minimizes a deterioration of the valuable inverted CIGS surface layer.

Outlook for the future work

In this thesis, I show that the negatively charged defects at the In(OH,S)/ZnO interface cause the poor performance in the In(OH,S) buffer solar cell. However, the chemical origin of these defects is still not clear. They can be surface states of the mixture of two compounds In_2S_3 and $\text{In}(\text{OH})_3$. They can also result from an adsorption of molecules from the chemical bath onto the In(OH,S) buffer surface. Further investigations, focusing on a correlation between the buffer deposition conditions (pH, concentrations) with the buffer properties and electrical performance of the solar cells, could lead to a determination of the chemical origin of these defects.

Since the treatments in the solutions containing Zn^{2+} passivate the defects on the surface of the In(OH,S) buffer layer, an optimization of the conditions like treatment time, Zn^{2+} concentration and temperature, is a key to further improve the performance of the In(OH,S) buffer solar cell. Using solutions containing other cations could be also meaningful. To prevent the treatment step, I would try to deposit the In(OH,S) buffer with adding a small amount of cations directly into the chemical solution.

The CIGS surface layer is very important for a reduction of the charge recombination at the buffer/CIGS interface. Therefore, an investigation of this layer in dependence on CIGS preparation parameters is essential.

The results of this work indicate that the role of the chemical bath deposited buffer is rather to save the CIGS inverted surface layer than modify it. Thus, the application of other “soft” deposition methods should have quite a high potential.

Appendix A:

Parameters used for the simulations

convergence

clamp_psi : 1.00e+00 units kT

clamp_n : 1.00e+00 units kT

clamp_p : 1.00e+00 units kT

termination_psi : 1.00e-03 units kT

termination_Fn : 1.00e-03 units kT

termination_Fp : 1.00e-03 units kT

maxiter : 500

back contact

Fi_m : 5.45 [eV]

Sn : 1.00e+00 [m/s]

Sp : 1.00e+06 [m/s]

Layer name : CIGS

d : 2.00e-06 [m]

v_th_n : 3.90e+05 [m/s]

v_th_p : 1.40e+05 [m/s]

eps : 10.00

chi : 4.50 [eV]

Eg : 1.15 [eV]

Nc : 6.70e+23 [m³]

Nv : 1.50e+25 [m³]

mu_n : 1.00e-02 [m²/Vs]

mu_p : 1.00e-03 [m²/Vs]

Na : 1.00e+22 [m³]

Nd : 0.00e+00 [m³]

A : 6.00e+06 [/(m×sqrt(eV))]

B : 0.00e+00 [sqrt(eV)/m]

SRH recombination

type : acceptor

sigma_n : 2.50e-17 [m²]sigma_p : 2.40e-19 [m²]

energy distribution : tail

Et : 0.30 [eV]

Ekar : 0.10 [eV]

profile : homogenous

Lkar : 1.00e-07 [m]

Nleft : 1.00e+21 [/m³ eV]Nright : 1.00e+21 [/m³ eV]**Interface recombination**

type : donor

sigma_nleft : 2.00e-24 [m²]sigma_nright : 2.00e-24 [m²]sigma_pleft : 1.00e-24 [m²]sigma_pright : 1.00e-24 [m²]

energy distribution : uniform

Et : 1.01 [eV]

Ekar : 0.20 [eV]

N : 5.00e+16 [/m² eV]**Layer name : CdS**

d : 5.00e-08 [m]

v_th_n : 1.00e+05 [m/s]

v_th_p : 1.00e+05 [m/s]

eps : 10.00

chi : 4.40 [eV]

Eg : 2.40 [eV]

Nc : 2.00e+25 [/m³]

Nv : 2.00e+25 [1/m³]
mu_n : 1.00e-04 [m²/Vs]
mu_p : 5.00e-04 [m²/Vs]
Na : 0.00e+00 [1/m³]
Nd : 1.00e+21 [1/m³]
A : 5.00e+07 [1/(m×sqrt(eV))]
B : 0.00e+00 [sqrt(eV)/m]

SRH recombination

type : acceptor
sigma_n : 1.00e-19 [m²]
sigma_p : 1.00e-19 [m²]
energy distribution : single
Et : 1.60 [eV]
Ekar : 0.10 [eV]
profile : homogenous
Lkar : 1.00e-07 [m]
Nleft : 1.00e+21 [1/m³]
Nright : 1.00e+21 [1/m³]

Interface recombination

type : acceptor
sigma_nleft : 1.00e-19 [m²]
sigma_nright : 1.00e-19 [m²]
sigma_pleft : 1.00e-19 [m²]
sigma_pright : 1.00e-19 [m²]
energy distribution : single
Et : 1.60 [eV]
Ekar : 0.10 [eV]
N : 1.40e+15 [1/m²]

Layer name : i-ZnO

d : 5.00e-08 [m]

v_th_n : 1.00e+06 [m/s]

v_th_p : 1.00e+06 [m/s]

eps : 10.00

chi : 4.60 [eV]

Eg : 3.30 [eV]

Nc : 5.00e+24 [/m³]

Nv : 5.00e+24 [/m³]

mu_n : 1.00e-04 [m²/Vs]

mu_p : 1.00e-04 [m²/Vs]

Na : 0.00e+00 [/m³]

Nd : 1.00e+22 [/m³]

A : 1.00e+08 [(m×sqrt(eV))]

B : 0.00e+00 [sqrt(eV)/m]

SHR recombination

type : neutral

sigma_n : 1.00e-19 [m²]

sigma_p : 1.00e-19 [m²]

energy distribution : single

Et : 2.00 [eV]

Ekar : 0.10 [eV]

profile : homogenous

Lkar : 1.00e-07 [m]

Nleft : 1.00e+17 [/m³]

Nright : 1.00e+17 [/m³]

Layer name : a-ZnO

d : 3.00e-07 [m]

v_th_n : 1.00e+06 [m/s]

v_th_p : 1.00e+06 [m/s]

eps : 10.00

chi : 4.60 [eV]

Eg : 3.30 [eV]

Nc : 5.00e+24 [/m³]

Nv : 5.00e+24 [/m³]

mu_n : 1.00e-04 [m²/Vs]

mu_p : 1.00e-04 [m²/Vs]

Na : 0.00e+00 [/m³]

Nd : 1.00e+24 [/m³]

A : 1.00e+08 [(m×sqrt(eV))]

B : 0.00e+00 [sqrt(eV)/m]

front contact

Sn : 1.00e+05 [m/s]

Sp : 1.00e+05 [m/s]

illuminated from : right

Symbols and Abbreviations

Symbols

α	Absorption coefficient, Auger parameter, thermal expansion coefficient, overall complexation coefficient
β	Stability product of complexes
C	Capacitance
d_w, d_b	Window thickness, buffer thickness
ΔE_C	Conduction band discontinuity
ΔE_V	Valence band discontinuity
ϵ	Relative dielectric permittivity
E_A	Activation energy
E_B, E_{kin}	Binding energy, kinetic energy
E_C	Conduction band energy
E_F	Fermi energy level
E_g	Band gap energy
E_V	Valence band energy
FF	Fill Factor
Φ_b^p	Barrier for holes
η	Solar cell efficiency
J, J_{sc}	Current density, short circuit current density
J_0	Saturation current density
k	Boltzmann constant
λ	Wavelength
n	Diode ideality factor
N_a, N_b, N_w	Doping concentration in the absorber, buffer and window layers
N_{ba}	Defect density at the buffer/absorber interface
N_{bw}	Defect density at the buffer/window interface
N_C	Effective density states in conduction band

N_V	Effective density states in valence band
P	Illumination power
q	Electrical charge
S_p	Interface recombination velocity
T, T_B	Temperature, bath temperature
V_{bi}	Built-in potential
V_D^a	Potential drop in the absorber layer
V_{OC}	Open circuit voltage
V_r	Reverse voltage bias

Abbreviations

ALD	Atomic layer deposition
CBD	Chemical bath deposition
CGS	$CuGaSe_2$
CIS	$CuInSe_2$
CIGS	$Cu(In,Ga)Se_2$
EDX	Energy-dispersive X-ray spectroscopy
IQE	Internal quantum efficiency
MOCVD	Metal organic vapor deposition
PVD	Physical vapor deposition
SCR	Space charge region
SIMS	Secondary-ion mass spectroscopy
SDL	Surface defect layer
TSC	Thermally stimulated capacitance
XPS	X-ray photoelectron spectroscopy

References

- [1] O. Lundberg, M. Bodegard, J. Malmström, and L. Stolt, *Prog. Photovolt.: Res. Appl.* **11**, 77 (2003).
- [2] E. A. Alsema, *Prog. Photovolt.: Res. Appl.* **8**, 17 (2000).
- [3] K. Ramanathan, M. A. Contreas, C. L. Perkins, S. Asher, F. S. Hasoon, J. Keane, D. Young, M. Romero, W. Metzger, R. Noufi, J. Ward, and A. Duda, *Prog. Photovolt.: Res. Appl.* **11**, 225 (2003).
- [4] M. Powalla, and B. Dimmler, in *3rd World Conf. on Photovolt. Energy Conv.* (2003), to be published.
- [5] V. Probst, W. Stetter, J. Palm, R. Toelle, S. Visbeck, H. Calwer, T. Niesen, H. Vogt, O. Hernandez, M. Wendl, and F. H. Karg, in *3rd World Conf. on Photovolt. Energy Conv.* (2003), to be published.
- [6] V. Probst, F. Karg, J. Rimmasch, W. Riedl, W. Stetter, H. Harms, O. Eibl, in *Proc. of MRS Spring Meeting* (1996).
- [7] J. R. Tuttle, M. A. Contreas, A. M. Gabor, K. R. Ramanathan, A. L. Tennant, D. S. Albin, J. Keane, R. Noufi, *Prog. Photovolt.: Res. Appl.* **3**, 383 (1995).
- [8] D. S. Albin, J. R. Tuttle, R. Noufi, *Journal of Electronics Materials* **24**, 351 (1995).
- [9] L. Stolt, J. Hedström, J. Kessler, M. Ruckh, K. O. Velthaus, H. W. Schock, *Appl. Phys. Lett.* **62**, 597 (1993).
- [10] M. A. Gabor, J. R. Tuttle, D. S. Albin, M. A. Contreas, R. Noufi, A. M. Herman, *Appl. Phys. Lett.* **65**, 198 (1994).
- [11] V. Nadenau, D. Braunger, D. Hariskos, M. Kaiser, C. Köble, A. Oberacker, M. Ruckh, U. Rühle, R. Schöffler, D. Schmidt, T. Walter, S. Zweigart, H. W. Schock, *Prog. in Photovolt.: Research and Applications* **3**, 363 (1995).
- [12] K. Orgassa, Q. Nguyen, I. M. Kötschau, U. Rau, H. W. Schock, and J. H. Werner, in *Proceeding of 17th Europ. Photovolt. Solar Energy Conf.*, edited by B. Mc-Nelis, W. Palz, H. A. Ossenbrink, and P. Helm (WIP-ETA, Florence, 2001), p. 1039.

- [13] M. Powalla, E. Lotter, R. Wächter, S. Spiering, M. Oertel, and B. Dimmler, in 29th IEEE Photovolt. Energy Conf. (IEEE Inc. Piscataway, 2002), p. 571.
- [14] M. A. Green, Solar Cells (Prentice-Hall, Inc., Englewood Cliffs, N. J., 1982).
- [15] A. Goetzenberger, B. Voß, J. Knobloch, Sonnenenergie: Photovoltaik (B. G. Teubner, Stuttgart, 1994).
- [16] S. M. Sze, Physics of Semiconductor Devices, 2nd ed. (John Wiley & Sons, Inc., New York, 1981).
- [17] T. Haalboom, T. Gödecke, F. Ernst, M. Rühle, R. Herberholz, H. W. Schock, C. Beilharz, und K. W. Benz, Inst. Phys. Conf. Ser. **152**, 249 (1998).
- [18] W. Hönle, G. Kühn, U. C. Boehnke, Cryst.Res. Technol. **23**, 1347 (1988).
- [19] S. B. Zhang, S. H. Wei, and A. Zunger, Phys. Rev. Lett. **78**, 4059 (1997).
- [20] R. Herberholz, H. W. Schock, U. Rau, J. H. Werner, T. Haalboom, T. Gödecke, F. Ernst, C. Beilharz, K. W. Benz, D. Cahen, in Proc. 26th IEEE Photovolt. Spec. Conf. (IEEE, New York, 1997), p. 332.
- [21] W. Chen, J. M. Stewart, B. J. Stanbery, W. Devaney, and R. Mickelsen, in 19th IEEE Photovolt. Spec. Conf. (IEEE Inc., Piscataway, 1987), p. 1445.
- [22] B. Dimmler, H. Dittrich, R. Menner, and H. W. Schock, in 19th IEEE Photovolt. Spec. Conf. (IEEE Inc., Piscataway, 1987), p. 1454.
- [23] M. I. Alonso, M. Garriga, C. A. Durante Rincon, E. Hernandez, and M. Leon, Appl. Phys. A **74**, 659 (2002).
- [24] K. Orgassa, U. Rau, H. W. Schock, and J. H. Werner, in 3rd World Conf. on Photovolt. Energy Conv. (2003), to be published.
- [25] S. Zhang, S.-H. Wei, A. Zunger, and H. Katayama-Yoshida, Phys. Rev. B **57**, 9642 (1998).
- [26] G. Hanna, A. Jasenek, U. Rau, and H. W. Schock, Thin Solid Films **387**, 71 (2002).
- [27] S.-H. Wei, S. B. Zhang, and A. Zunger, Inst. Phys. Conf. Ser. **152**, 765 (1998).
- [28] U. Rau and H. W. Schock, in Clean Electricity from Photovoltaics, edited by M. D. Archer and R. Hill (Imperial College Press, London, 2001).

- [29] R. W. Birkmire, *Solar Energy Materials & Solar Cells* **65**, 17 (2001).
- [30] U. Rau and H. W. Schock, *Appl. Phys. A* **69**, 131 (1999).
- [31] L. L. Kazmerski, *Ins. Phys. Conf. Ser.* **35**, 217 (1997).
- [32] R. R. Potter, C. Eberpacher, L. B. Fabick, in *Conf. Rec. of the 18th IEEE Photovolt. Special. Conference, las Vegas (IEEE, New York, 1985)*, p. 1659.
- [33] R. W. Birkmire, B. E. McCandless, W. N. Shafarman, R. D. Varrin, in *Proc. 9th E. C. Photovoltaic Solar Energy Conference, (Kluwer Ed., Dordrecht, 1989)*, p. 134.
- [34] R. H. Mauch, M. Ruckh, J. Hedström, D. Lincot, J. Kessler, R. Klinger, L. Stolt, J. Vedel, H. W. Schock, in *Proc. 10th E. C. Photovoltaic Solar Energy Conference, Lissabon (Kluwer Ed., Dordrecht, 1991)*, p. 1031.
- [35] D. Lincot and J. Vedel, in *Proc. 10th E. C. Photovoltaic Solar Energy Conference, (Kluwer Ed., Dordrecht, 1991)*, p. 931.
- [36] J. Kessler, M. Ruckh, D. Hariskos, U. Rühle, R. Menner and H. W. Schock, in *Conf. Rec. of the 23th IEEE Photovoltaic Specialists Conference, Louisville (IEEE, New York, 1993)*, p. 447.
- [37] K. Orgassa, U. Rau, Q. Nguyen, H. W. Schock, J. H. Werner, *Prog. Photovolt: Res. Appl.* **10**, 457 (2002).
- [38] M. A. Contreas, H. Wiesner, J. Tuttle, K. Ramanathan, and R. Noufi, in *Technical Digest of the 9th International Photovoltaic Science and Engineering Conference, Miyazaki (1996)*, p. 127.
- [39] R. H. Bube, *Photovoltaic Materials, (Imperial College Press, London, 1998)*.
- [40] J. B. Turner, R. J. Schwartz, J. L. Gray, in *Conf. Rec. of the 20th IEEE Photovoltaic Specialists Conference, Las Vegas (IEEE, New York, 1988)*, p. 1457.
- [41] A. Niemegeers, M. Burgelman, and A. De Vos, *Appl. Phys. Lett.* **67**, 843 (1995).
- [42] M. A. Contreras, T. Nakada, M. Hongo, A. O. Pudov, and J. R. Sites, in *3th World Conf. on Photovolt. Energy Conv. (2003), 2LNCO8, to be published*.
- [43] T. Nakada, K. Furumi, and A. Kunioka, *IEEE Trans. on Electron. Devices* **46**, 2093 (1999).

- [44] K. Kushiya and O. Yamase, *Jpn. J. Appl. Phys.* **39**, 2577 (2000).
- [45] K. Kushiya, M. Tachiyuki, T. Kase, Y. Nagoya, T. Miura, D. Okumura, M. Satoh, I. Sugiyama, and O. Yamase, in *Proc. 26th IEEE Photovolt. Spec. Conf.* (IEEE, New York, 1997), p. 327.
- [46] W. Eisele, A. Ennaoui, P. Schubert-Bischoff, M. Giersig, C. Pettenkofer, J. Kauser, M. Lux-Steiner, S. Zweigart and F. Karg, *Solar Energy Materials and Solar Cells* **75**, 17 (2003).
- [47] A. Ennaoui, W. Eisele, M. Lux-Steiner, T. P. Niesen and F. Karg, *Thin Solid Films*, **431-432**, 335 (2003).
- [48] Y. Ohtake, M. Ichikawa, A. Yamada and M. Konagai, in *Proc. 26th Europ. Photovolt. Solar Energy Conf.* (Stephens, Bedford, 1995), p. 2088.
- [49] L. Olson, W. Addis, D. Huber, in *Proc. 23th IEEE Photovolt. Spec. Conf.* (IEEE, New York, 1993), p. 603.
- [50] Y. Ohtake, K. Kushiya, M. Ichikawa, A. Yamada and M. Konagai, *Jpn. J. Appl. Phys.* **34**, 5949 (1995).
- [51] Y. Ohtake, M. Ichikawa, T. Okamoto, A. Yamada, M. Konagai and K. Saito, in *Proc. 25th IEEE Photovolt. Spec. Conf.* (IEEE, New York, 1996), p. 793.
- [52] S. Chaisitsak, A. Yamada, M. Konagai, and K. Saito, *Jpn. J. Appl. Phys.* **39**, 1660 (2000).
- [53] A. Shimizu, S. Chaisitsak, T. Sugiyama, A. Yamada, M. Konagai, *Thin Solid Films* **361-362**, 193 (2000).
- [54] D. Hariskos, M. Ruckh, U. Rühle, T. Walter, H. W. Schock, J. Hedström, and L. Stolt, *Solar Energy Materials & Solar Cells* **41/42**, 345 (1996).
- [55] C. H. Huang, S. S. Li, W. N. Shafarman, C.-H. Chang, E. S. Lambers, L. Rieth, J. W. Johnson, S. Kim, B. J. Stanbery, T. J. Anderson, and P.H. Holloway, *Solar Energy Materials & Solar Cells* **69**, 131 (2001).
- [56] S. Spiering, D. Hariskos, M. Powalla, N. Naghavi and D. Lincot, *Thin Solid Films* **431-432**, 359 (2003).

- [57] D. Braunger, PhD. Thesis, Stuttgart University, p. 129, 1999.
- [58] A. Strohm, personal communication
- [59] M. Konagai, Y. Ohtake, T. Okamoto, *Mat. Res. Soc. Symp. Proc.* **426**, (1996) p. 153.
- [60] U. Rau, K. Weinert, Q. Nguyen, M. Mamor, G. Hanna, A. Jasenek, and H. W. Schock, *Mat. Res. Soc. Symp. Proc.* **668**, H9.1.1 (2001).
- [61] U. Rau, M. Schmidt, A. Jasenek, G. Hanna, and H. W. Schock, *Solar Energy Materials & Solar Cells* **67**, 137 (2001).
- [62] M. Turcu, O. Pakma, and U. Rau, *Appl. Phys. Lett.* **80**, 2598 (2002).
- [63] M. Turcu, U. Rau, *J. Phys. Chem. Sol.* **64**, 1591 (2003).
- [64] U. Rau and M. Turcu, in *Proceeding of MRS Spring Meeting (2003)*, B8.8.
- [65] R. Klenk, *Thin Solid Films* **387**, 135 (2001).
- [66] D. Schmid, M. Ruckh, F. Grunwald, and H. W. Schock, *J. Appl. Phys.* **73**, 2902 (1993).
- [67] T. Negami, N. Kohara, M. Nishitani, and T. Wada, *Jpn. J. Appl. Phys. Part 2*, **33**, L1251 (1994).
- [68] T. Walter, R. Herberholz, C. Müller, and H. W. Schock, *J. Appl. Phys.* **80**, 4411 (1996).
- [69] Y. Yan, K. M. Jones, J. Abushama, M. Young, S. Asher, M. M. Al-Jassim and R. Noufi, *Appl. Phys. Lett.* **81**, 1008 (2002).
- [70] S. B. Zhang and S.-H. Wei, *Phys. Rev. B* **65**, 081402 (2002).
- [71] M. Morkel, L. Weinhardt, B. Lohmüller, C. Heske, E. Umbach, W. Riedl, S. Zweigart, and F. Karg, *Appl. Phys. Lett.* **79**, 4482 (2001).
- [72] S. B. Zhang, S.-Wei, and A. Zunger, *J. Appl. Phys.* **83**, 3192 (1998).
- [73] D. Schmid, Ph.D Thesis, Stuttgart (1996).
- [74] D. Cahen and R. Noufi, *Solar Cells* **30**, 53 (1991).

- [75] U. Rau, D. Braunger, R. Herberholz, H. W. Schock, J.-F. Guillemoles, L. Kronik, and D. Cahen, *J. Appl. Phys.* **86**, 497 (1999).
- [76] R. Herberholz, U. Rau, H. W. Schock, T. Haalboom, T. Gödecke, F. Ernst, C. Beilharz, K. W. Benz, D. Cahen, *Eur. Phys. J. AP* **6**, 131 (1999).
- [77] J. E. Jaffe and A. Zunger, *Phys. Rev. B* **29**, 1882 (1984).
- [78] C. Heske, D. Eich, E. Umbach, T. van Buuren, C. Bosteds, L. J. Terminello, S. Kakar, M. M. Grush, T. A. Callcott, F. J. Himpsel, D. L. Ederer, R. C. C. Perera, W. Riedl, F. Karg, *Appl. Phys. Lett.* **74**, 1451 (1999).
- [79] T. Nakada, A. Kunioka, *Appl. Phys. Lett.* **74**, 2444 (1999).
- [80] K. Ramanathan, H. Wiesner, S. Asher, D. Nieves, R. N. Bhattacharya, J. Keane, M. A. Contreas, and R. Noufi, in *Proc. 2nd WCPEC, Viena, Austria, 1998*, p. 477.
- [81] T. Wada, S. Hayashi, Y. Hashimoto, S. Nishiwaki, T. Sato, T. Negami, M. Nishitani, in *Proc. 2nd World Conf. on Photovolt. Energy Conv.*, J. Schmidt, H. A. Ossenbrink, P. Helm, H. Ehmman, and E. D. Dunlop (Eds.) (E. C. Joint Res. Centre, Luxembourg, 1998), p. 403.
- [82] T. Nakada, *Thin Solid Films* **361-362**, 346 (2000).
- [83] Dongxiang Liao and Angus Rockett, *J. Appl. Phys.* **93**, 9380 (2003).
- [84] K. Ramanathan, R. N. Bhattacharya, J. Granata, J. Webb, D. Niles, M. A. Contreas, H. Wiesner, F. S. Hanson, R. Noufi, in *Conf. Rec. of the 26th IEEE Photovoltaic Spec. Conf. (IEEE, Piscataway, 1997)*, p. 319.
- [85] P. W. Yu, S. P. Faile, Y. S. Park, *Appl. Phys. Lett.* **26**, 384 (1975).
- [86] P. W. Yu, Y. S. Park, S. P. Faile, J. P. Faile, *Appl. Phys. Lett.* **26**, 717 (1975).
- [87] M. A. Gabor, J. R. Tuttle, D. S. Albin, M. A. Contreas, R. Noufi, A. M. Herman, *Appl. Phys. Lett.* **65**, 198 (1994).
- [88] M. A. Contreas, J. Tuttle, A. Gabor, A. Tennant, K. Ramanathan, S. Asher, A. Franz, J. Keane, L. Wang, J. Scofield, R. Noufi, in *Proc. 1st World Conf. on Photovolt. Energy Conv. (IEEE, New York, 1994)*, p. 68.

- [89] G. Franz, *Oberflächentechnologie mit Niederdruckplasmen*, 2. Auflage (Spring-Verlag, Berlin, 1994).
- [90] R. A. Haefler, *Oberflächen-und Dünnschicht-Technologie, Teil 1: Beschichtung von Oberflächen (Werkstoff-Forschung und-Technik; Bd. 5)*, (Spring-Verlag, Berlin, 1987)
- [91] K. Siegbahn et al., *ESCA Applied to Free Molecules*, North Holland, Amsterdam, (1969).
- [92] W. F. Egelhoff, *Surf. Sci. Rep.* **6**, 253 (1987).
- [93] C. D. Wagner, in *Practical Surface Analysis*, 2 Ed. Vol. 1; Auger and X-ray Photoelectron spectroscopy, Edited by D. Briggs and M. P. Seah (John Wiley & Sons, Chichester, 1996), p. 595.
- [94] *Handbook of X-ray Photoelectron Spectroscopy, A Reference Book of Standard Data for Use in X-ray Photoelectron Spectroscopy*, edited by C. D. Wagner, W. M. Riggs, L. E. Davis, J. F. Moulder, G. E. Muilenberg (Perkin-Elmer Corporation, Eden Prairie, Minnesota, 1979).
- [95] *Handbook of X-ray Photoelectron Spectroscopy, A Reference Book of Standard Spectra for Identification and Interpretation of XPS Data*, edited by J. F. Moulder, W. F. Stickle, P. E. Sobol, K. D. Bomben, J. Chastain (Perkin-Elmer Corporation, Eden Prairie, Minnesota, 1992).
- [96] S. M. Sze, *Physics of Semiconductor Devices*, 2nd ed. (John Wiley & Sons Inc., New York, 1981).
- [97] U. Rau, H. W. Schock, *Appl. Phys. A* **69**, 131 (1999).
- [98] U. Rau, A. Jasenek, H. W. Schock, F. Engelhardt, Th. Mayer, *Thin Solid Films* **361-362**, 298 (2000).
- [99] N. R. Pavaskar, C. A. Menezes, and A. P. B. Sinha, *J. Electrochem. Soc.* **124**, 743 (1977).
- [100] I. Kaur, D. K. Pandya, and K. L. Chopra, *J. Electrochem. Soc.* **127**, 943 (1980).
- [101] N. T. S. Nair, P. K. Nair, and J. Campos, *Thin Solid Films* **161**, 21 (1988).
- [102] J. M. Dona, and J. Herrero, *J. Electrochem. Soc.* **139**, 2810 (1992).

- [103] D.Lincot, R. Ortega-Borges and M. Froment, *Appl. Phys. Lett.* **64**, 569 (1994).
- [104] M. Froment, M. C. Bernard, R. Cortes, B. okili, D. Lincot, *J. Electrochem. Soc.* **42**, 2642 (1995).
- [105] R. Cortes, M. Froment, B. Mokili, D. Lincot, *Phil. Mag. Lett.* **73**, 209 (1996).
- [106] G. A. Kitaev, A. A. Uritskaya, and S. G. Moksushin, *Russ. J. Phys. Chem.* **39**, 1101 (1965).
- [107] I. Kaur, D. K. Pandya, and K. L. Chopra, *J. Elechtrochem. Soc.* **127**, 943 (1980).
- [108] M. Froment and D. Lincot, *Electrochim. Acta* **40**, 1293 (1995).
- [109] G. D. Parfitt, *Pure Appl. Chem.* **48**, 415 (1976).
- [110] A. Kylner and E. Niemi, in *Proceeding of the 14th E.C. Photovoltaic Solar Energy Conference and Exhibition, Barcelona, Spain, (H.S Stephens & Associates, Bedford, 1997)*, p. 1326.
- [111] F. Engelhardt, L. Bornemann , M. Köntges, T. Mayer, J. Parisi, E. Pschorr-Schoberer, B. Hahn, W. Gebhardt, W. Riedl, and U. Rau, *Prog. Photovolt. Res. Appl.* **7**, 423 (1999).
- [112] K. Orgassa, U. Rau, Q. Nguyen, H. W. Schock, and J. H. Werner, *Prog. Photovolt. Res. Appl.* **10**, 457 (2002).
- [113] D. Hariskos, *Dissertation, University of Stuttgart, 1998.*
- [114] J. Sterner, C. Platzer-Björkman, and L. Stolt, in *Proceeding of 17th European PV Solar Energy Conference, Munich, 2001*, p. 1118.
- [115] D. Lincot, R. Ortega-Borges, J. Vedel, M. Ruckh, J. Kessler, K. O. Velthaus, D. Hariskos, and H. W. Schock, in *Proceedings of the 11th E. C. Photovoltaic Solar Energy Conference, Harwood Academic Publishers, Montreux, Switzeland (1992)*, p. 870.
- [116] J. Kessler, K. O. Velthaus, M. Ruckh, R. Laichinger, H. W. Schock, D. Lincot, R. Ortega, and J. Vedel, in *Proceedings of the 6th International Photovoltaic Science and Engineering Conference, New Delhi, India (1992)*, p. 1005.
- [117] A. Kylner, *J. Electrochem. Soc.* **146**, 1816 (1999).

- [118] T. M. Friedlmeier, D. Braunger, D. Hariskos, M. Kaiser, H. N. Wanka, and H. W. Schock, in Proceedings of the 25th IEEE Photovoltaic Specialists Conference, Washington DC, 1996, p. 845.
- [119] K. Ramanathan, R. N. Bhattacharya, J. Granata, J. Webb, D. Nieves, M. A. Contreas, H. Wiesner, F. S. Hasoon, and R. Noufi, Proceeding of the 26th IEEE Photovoltaic Specialists Conference, Anaheim, CA (IEEE, New York, 1997), p. 319.
- [120] K. Ramanathan, H. Wiesner, S. Asher, D. Nieves, R. N. Bhattacharya, J. Keane, M. A. Contreas, and R. Noufi, Second WCPEC, Viena, Austria, 1998, p. 477.
- [121] T. Wada, S. Hayashi, Y. Hashimoto, S. Nishiwaki, T. Sato, T. Negami and M. Nishitani, in Proc. of the 2nd World Conference and Exhibition on Photovol. Solar Energy Conversion, Vienna, Austria, 1998, p. 403.
- [122] T. Nakada and A. Kuiuoka, Appl. Phys. Lett. **74**, 2444 (1999).
- [123] Dongxiang Liao and Angus Rockett, J. Appl. Phys. **93**, 9380 (2003).
- [124] A. Ringbom, in: Les Complexes en Chimie Analytique, Dunod Ed., Paris (1967).
- [125] D. Braunger, PhD. Thesis, Stuttgart University, 1999, pp 83-86.
- [126] E. H. Swift and E. A. Butler, Analytical Chemistry **28**, 146 (1956).
- [127] C. F. Baes and R. E. Mesmer, The hydrolysis of cations, Wiley-Interscience (1976).
- [128] R. Ortega-Borges and D. Lincot, J. Electrochem. Soc. **140**, 3464 (1993).
- [129] A. Kylner, J. Lindgren, and L. Stolt, J. Electrochem. Soc. **143**, 2662 (1996).
- [130] C. H. Huang, S. S. Li, W. N. Shafarman, C.-H. Chang, E. S. Lambers, L. Rieth, J. W. Johnson, S. Kim, B. J. Stanbery, T. J. Anderson, and P.H. Holloway, Solar Energy Materials & Solar Cells **69**, 131 (2001).
- [131] R. Nomura, K. Konishi, H. Matsuda, Thin Solid Films **198**, 339 (1991).
- [132] Q. Nguyen, K. Orgassa, I. Koetschau, U. Rau, and H. W. Schock, Thin Solid Films **431-432**, 330 (2003).
- [133] U. Rau and M. Schmidt, Thin Solid Films **387**, 141 (2001).

- [134] M. W. Hillen and J. F. Verwey, in *Instabilities in Silicon Devices*, G. Barbottin and A. Vapaille, Editors, Vol. 1, Amsterdam, The Netherlands, 1986, p. 403.
- [135] P. Zabierowski, U. Rau, and M. Igalson, *Thin Solid Films* **387**, 147 (2001).
- [136] R. Herberholz, M. Igalson, H. W. Schock, *J. Appl. Phys.* **83**, 318 (1998).
- [137] M. Igalson and P. Zabierowski, *Thin Solid Films* **361-362**, 371 (2000).
- [138] M. Igalson, A. Kubiazcyk, and P. Zabierowski, *Mat. Res. Soc. Symp. Proc.* **668**, H9.2.1 (2001).
- [139] M. Igalson, M. Bodegard, and L. Stolt, *Solar Energy Materials & Solar Cells* **80**, 195 (2003).
- [140] U. Rau, D. Braunger, R. Herberholz, H. W. Schock, J.-F. Guillemoles, L. Kronik, and D. Cahen, *J. Appl. Phys.* **86**, 497 (1999).
- [141] A. Niemegeers and M. Burgelman, in *Proceedings of the 25th IEEE Photovoltaic Specialists Conference*, IEEE, New York, 1996, p. 901
- [142] D. Cahen and R. Noufi, *Appl. Phys. Lett.* **54**, 558 (1989); *Solar Cells* **30**, 53 (1991).
- [143] D. Cahen and L. Chernyak, *Adv. Mater.* **9**, 861 (1997).

Acknowledgement

I would like to sincerely thank Prof. Emil Roduner for accepting and supporting me as a PhD student and for contributing to the successful completion of this PhD thesis.

I am very grateful to Prof. Jürgen H. Werner for giving me the opportunity to do this work at the Institute of Physical Electronics and for helpful suggestions.

I want to express my sincere gratitude to Prof. Le Thi Trong Tuyen for guiding me into the basic knowledges of surface and interface science.

I am greatly thankful to Dr. Hans-Werner Schock for valuable suggestions and evaluating this work.

Special thanks are given to Dr. habil. Uwe Rau for interesting discussions in the field of physical and chemical defects in semiconductor devices.

In connection with the XPS and SIMS measurements I would like to thank Dr. Gerhard Bilger for the patience to professionally introduce me to surface analysis. I extend my appreciations to my co-workers in the chemical lab at the institute Dr. H. Kerber, Dr. V. Laptev and T. Adler for showing me techniques and giving me helpful advices from their own experiences. For the supply of Cu(In,Ga)Se₂ substrates I am greatly thankful to my colleagues Dr. Immo Kötschau, Holm Wiesner and Dennis Kühnle. Leo Bauer, Martin Wagner, Dr. Kristin Weinert are greatly acknowledged for their technical supports. Many thanks are given to Dr. George Hanna, Dr. Kay Orgassa and Dr. Mircea Turcu for collaborations and interesting discussions in the field of CIGS solar cells.

I would also like to thank all other of my former and present colleagues at the Institute of Physical Electronics for a nice working atmosphere and the supporting co-operation.

The Foundation of German Academy of Exchange Service (DAAD) is greatly acknowledged for the financial support of this work.

Especially, I would like to thank my wife who did support me and take care of me with all her love.

Curriculum Vitae

Nguyen Hong Quang

Born on 17th May, 1970 in Hanoi Vietnam

1976-1980	Primary school in Hanoi
1980-1986	Secondary school in Hanoi
1986-1987	Learned Russian language in Hanoi
1987-1995	University Minsk, Belorussia Studied chemistry Received Master degree in Chemistry
1995-1997	Firma „Dai Viet“, Vietnam Technical assistant
1997-1999	Center for Natural Science and Technology, Hanoi, Vietnam Institute of Material Science Researcher
4/1999-10/1999	Göthe Institut, Bremen DAAD scholarship holder Learned German language
1/2000	University Stuttgart DAAD scholarship holder PhD thesis under supervisions of Prof. Dr. E. Roduner at the Institute of Physical Chemistry and Prof. J. H. Werner at the Institute of Physical Electronics